Development of X-ray Phase Contrast and Microtomography Methods for the 3D Study of Fatigue Cracks

A Thesis
Presented to
The Academic Faculty

by

Konstantin I. Ignatiev

In Partial Fulfillment
of the Requirements for the Degree
Doctor of Philosophy

School of Materials Science and Engineering
Georgia Institute of Technology
July 2004

Development of X-ray Phase Contrast and Microtomography Methods for the 3D Study of Fatigue Cracks

Approved by:

Professor Stuart R. Stock, Committee Chair

Professor W. Steven Johnson

Professor Thomas H. Sanders

Professor Angus P. Wilkinson

Professor Robert L. Snyder

Date Approved: August, 19, 2004

ACKNOWLEDGEMENTS

First of all, the author would like to thank his advisor, Dr. Stuart R. Stock, for his invaluable guidance, time and patience. He would also like to thank his committee members from the Georgia Institute of Technology: Dr. Thomas H. Sanders, Dr. Robert L. Snyder, Dr. W. Steven Johnson and Dr. Angus P. Wilkinson.

The author would like to thank Wah-Keat Lee and Kamel Fezza from Argonne National Laboratory for their help with the experimental setup and data collection and for valuable discussion on the X-ray phase contrast imaging and for providing the aluminum phantom samples. The author would also like to acknowledge Robert Morano for the microtomography data on sample CT-41M, Jon Almer (APS) for making loading stage available for in-situ measurements at the APS beamline 1-ID and Francesco De Carlo for helping with the synchrotron microtomography measurements and data reconstruction at the APS beamline 2-BM. Most of the laboratory microtomography data used in this work was collected by Prof. J.C. Elliott and Dr. G.R. Davis from Queen Mary, University of London. The author would also like to acknowledge Dr. Eugene P. Lautenschlager of Northwestern University for helping fracture sample CT-33M.

The author wishes to especially thank his wife, Ms. Olga Tsareva, for her extraordinary patience and encouragement, which helped author a lot during the times when it was hard to see a light at the end of the tunnel.

The Office of Naval Research funded the initial portion of the research through grants N00014-89-J-1708 and N00014-94-1-0306. The synchrotron measurements were conducted at Advanced Photon Source which is supported by the US Department of Energy, Office of Basic Energy Sciences, under contract No. W-31-109-Eng-38.

TABLE OF CONTENTS

LIST OF TABLES

LIST OF FIGURES

LIST OF SYMBOLS AND ABBREVIATIONS

0D	zero-dimensional.
1D	one-dimensional.
2D	Two-dimensional.
3D	Three-dimensional.
a	crack length.
ANL	Argonne National Laboratory.
APS	Advanced Photon Source.
ASTM	american standards for testing materials.
B	sample thickness.
β	imaginary part of the index of refraction.
CCD	charge coupled device.
CT	computed tomography.
da/dN	crack growth rate.
δ	deviation of index of refraction from unity.
ΔK	Stress intensity factor range.
ΔK_{eff}	Stress intensity factor range.
η	index of refraction.
I	X-ray intensity.
I_0	incoming X-ray intensity.
K	Stress intensity factor.
K_{max}	maximum stress intensity factor.
λ	X-ray wavelength.
μ	linear atenuation coefficient.
μ_{air}	linear attenuation coefficient of air.
μ_{mean}	mean linear attenuation coefficient.

p	propagation function.
P	Fourier transform of propagation function.
ψ	wavefunction.
Ψ	Fourier transform of wavefunction.
q	Transmission function.
Q	Fourier transform of transmission function.
R	distance from axis of rotation to feature of interest.
SEM	Scanning electron microscopy.
σ_y	yield stress.
t	thickness of the sample.
θ	sample rotation angle.
ε	dielectrical constant.
φ	wave phase.
voxel	volume element.

SUMMARY

In this work, two innovations were demonstrated for in-situ 3D study of fatigue cracks and their closure as a function of applied load. The first related to improvements in how absorption microtomography is used to study fatigue cracks. The second is a new approach to 3D crack mapping relying on X-ray phase imaging and stereometric approaches.

Absorption microtomography was used to determine crack surface positions. A special algorithm was used to detect crack positions that increased accuracy of the crack detection process over methods used previously. Crack opening was measured from absorption microtomography data both before and after crack extension and patterns of opening at several loads were analyzed for both cases.

X-ray phase contrast imaging, an alternative approach to absorption microtomography, whose sensitivity to cracks is not strongly affected by the shape of the specimen, was also investigated. Phase imaging provides much greater contrast (than absorption-based imaging) at interfaces where refraction index changes. Increased sensitivity of phase imaging to cracks, compared to that of the absorption X-ray methods, allowed detecting crack positions up to the crack tip with no load applied to the sample. As demonstrated here, phase contrast imaging approaches optical microscopy in terms of the minimum resolution achievable. Stereometry reconstruction based on the phase microradiographs was carried out, and the results were compared with those of absorption microtomography on the same specimen. This study demonstrated that it is possible to reconstruct accurate 3D positions of features inside optically opaque sample by recording several X-ray phase microradiographs.

Computer simulation of the X-ray interaction with a cracked aluminum sample

was carried out, based on the physical processes behind phase contrast formation and taking into account experimental parameters such as the sample's geometry (including that of the crack), the X-ray wavelength, the material's index of refraction and sample - detector distance. The simulation provided good qualitative agreement with experimental phase images.

CHAPTER I

INTRODUCTION

There is currently great interest in application of lightweight aluminum alloys to various structures due to their high specific strength. Aluminum-lithium alloys are a prime example of such materials, since lithium is the only alloying element that increases strength and elastic modulus while decreasing the density of the alloy. Since many potential applications for lightweight alloys involve variable loading conditions, fatigue crack propagation rate is of concern. Aluminum-lithium AA 2090 stands out as an alloy that has an abnormally low fatigue crack propagation rate in certain orientations [2]. Previous investigations showed that the reason behind the decreased crack growth rates is what is termed roughness induced crack closure [3–5] — a process that occurs during unloading portion of fatigue cycle when the faces of the crack contact each other before the minimum load is reached and during loading portion of the cycle when faces remain in contact until some effective load, which is higher than minimum load, is reached. This in turn reduces effective value of the crack tip driving "force" and results in lower than usual fatigue crack propagation rate.

Optical and SEM studies revealed that the highly non-planar jagged crack is responsible for the crack path closure in L-T oriented compact tension samples of AA 2090 [2]. Previous microdiffraction investigations [6] showed that this is due to a specific mesostructure: regions of AA 2090 alloy consist of near single crystal material containing 5 to 10 pancake-shaped grains with each grain dimensions of approximately 2.5 mm in the plate rolling direction, 500 μm in the transverse direction and 50 μm in the short transverse direction. Passage of the crack through these volumes forms the

large asperities in AA 2090. Other Al-Li alloys, which have more planar crack paths and which exhibit normal fatigue crack growth rates than AA 2090, do not have this type of mesostructure [7].

X-ray methods are the only good choice for studying the phenomenon of crack closure. Serial sectioning is time consuming and destroys the specimen. There are always questions about artifacts introduced by the sectioning or about changes in crack face contact due to changes in physical constraint (from removing material). Optical and electron microscopy can only provide information about the surface and near-surface processes. However, by its nature, the crack propagation and accompanying crack opening and closing are 3D processes and need to be studied with methods that can give information about what is going on inside optically opaque specimen. X-ray absorption microtomography was used to study crack closure in AA 2090 alloy [8–12]. Advantages of this method are that it is non-destructive, that it can give 3D information about the crack location and its opening, and it allows in-situ measurements, that is measurements of the sample corresponding to different applied loads, simulating different portions of a fatigue cycle.

The earlier studies [8–16] with absorption microtomography employed notched tensile as well as compact tension samples (see Background for details). The focus of these studies was on determining pattern of contact of the opposite crack faces as a function of applied load. One question remaining was how does pattern of opening change after crack extends. Unfortunately, the shape of the specimen that is customarily used for fatigue testing and for which a large database already exists, namely the compact tension specimen, is ill-suited for studies by X-ray absorption microtomography due to a number of reasons given in the following section. A novel X-ray method, imaging with X-ray phase contrast, or in-line holography, developed over the last decade, is one method of overcoming the limitations of X-ray absorption microtomography.

Phase contrast is a well-known effect in the visible wave range; however it only recently became available for radiation with wavelengths in the X-ray range, due to advent of third generation synchrotron sources such as Advanced Photon Source (APS) at Argonne National Laboratory. The resulting highly collimated, high energy X-ray beam increases sensitivity in X-ray phase imaging up to 100 times compared with X-ray absorption imaging for light elements [17]. X-ray phase contrast imaging has recently been used to study biological and medical samples and to distinguish between tissues with similar X-ray attenuation coefficients [18–20]. In the area of materials science, it was used to study damage inside a sample of an aluminum alloy reinforced with SiC particles [21].

The overarching aim of the research described below was to demonstrate new approaches to the 3D study of fatigue cracks in compact tension geometry samples. First, samples had never been examined previously with absorption microtomography before and after crack extension: data on changing patterns of crack closure appear below. Second, an alternative approach (phase contrast stereometry) to absorption microtomography is investigated for 3D quantification of crack position and opening. Specifically, this portion of the research explores application of X-ray phase contrast imaging to the study of crack closure in compact tension specimens, to develop a new approach to tomography optimized for plate-like samples containing a sharply defined object or series of objects, and to compare results obtained with the phase contrast method to those obtained with absorption microtomography.

CHAPTER II

BACKGROUND

While the focus of this thesis is the development of new approaches to study fatigue cracks in 3D, in particular techniques improving crack sensitivity, it is first necessary to examine why such techniques are needed. This is done by providing background on crack closure and the material system under study. Next background on micro-tomography is provided. Then section 2.3 details prior work with microtomography on crack closure and its limitations requiring development of new approach. X-ray phase imaging background is provided in the final section.

2.1 Crack closure

The aluminum alloy used to investigate new approaches to 3D study of fatigue cracks in compact tension geometry samples was AA2090 T8E41. Fatigue crack growth rates in AA 2090 are, along certain plate orientations, unusually low compared to other aluminum alloys [2, 22–26]. The low crack growth rates in the L-T plate orientation (crack growth along the plate's T direction and loading along the L direction) was attributed to the very rough surface geometry of the cracks [4, 27], and planar slip behaviour controlled by coherent and shearable ordered $\delta'(Al_3Li)$ precipitates [28, 29] and the near-single crystal volumes formed by the peculiar mesotexture [6] were responsible for development of large asperities.

Each weight % of lithium added to aluminum lowers the density of the alloy 3% and improves elastic modulus 6% for additions of Li up to 4% [2]. Interest in aluminum-lithium alloys was primarily caused by the fact that they were cheaper than composites, compatible manufacturing technology could be used, and it offered

considerably higher ductility and fracture toughness than composites. Strengthening in Al-Li alloys comes mostly from hardening by the nucleation and growth of one or more second phase particle distributions, precipitated from a supersaturated solid solution [2].

Binary Al-Li alloys have low ductility and low toughness due to inhomogenous slip and strain localization [28], which in turn is caused by coherent $\delta'(Al_3Li)$ particle hardening in the matrix, nucleation and growth of grain boundary AlLi δ precipitates and the formation of δ' - precipitate free zones (PFZ). To improve its properties, additional alloying elements were introduced and modifying thermomechanical treatments were developed. In particular, to reduce the inhomogenous mode of deformation, ternary elements (such as Cu and Mg) and dispersoid forming elements (Zr, Mn), that form a fine dispersion of intermetallic phases to reduce the tendency for localized deformation, were introduced (Zr is preferred because its addition results in fine structure and better corrosion properties). AA 2090 T8E41 has 1.9-2.6 weight % of Li, 2.4-3.0% of Cu, 0.08-0.15% of Zr, 0.12% of Fe, 0.10% of Si, 0.25% of Mg, 0.05% of Mn and 0.15% of Ti. The T8E41 heat treatment (solution treatment at 549° with successive water quench, 6% stretch and aging at 163° for 24 hours) produces pancake-shaped anisotropic grains with the dimensions of 2.5 mm in the rolling direction of the plate, 500 μm in the transverse direction and 50 μm in the short transverse direction.

As a result, advanced commercial Al-Li alloys, such as AA 2090, exhibit strength-toughness combinations that are comparable or superior to traditional Al alloys. Specific Al-Li alloys can be 30% higher in strength with similar elongation and toughness properties compared with traditional aluminum alloys (in longitudinal orientation).

The fatigue behavior of AA 2090 benefits from more pronounced crack tip shielding from crack deflection, crack path tortuosity (which is caused by shearable nature of coherent δ' precipitates, crystallographic texture, and anisotropic grain structure) and consequent, roughness induced crack closure mechanisms, which can significantly

decrease fatigue crack growth rates [2].

The phenomenon when opposite crack faces prematurely contact each other during the fatigue unloading cycle is termed crack closure. This behavior reduces crack tip driving "force" and, as a result, decreases crack propagation rates. A variety of crack closure mechanisms exist, including oxide-induced crack closure [30], plasticity-induced closure [3, 31] and roughness-induced crack closure [32]. Crack face roughness dominates in samples of AA 2090 [33]. There are several techniques used for crack closure and crack opening determination, but apart from the microtomography technique described in more detail in Section 2.3 these techniques are either macroscopic in nature, i.e. they measure macroscopic response of the sample such as strain through the sample's experimental compliance curve [3], changes in electric current through the sample, or they are 2D, i.e. they are based on the observation of the sample surface behavior, such as optical and scanning electron microscopy, optical and laser interferometry. Models of crack closure/opening include the one proposed by Elber [3] which assumes that the crack tip is fully shielded from any load below the opening load, and the incremental crack closure model, which assumes that the closure/opening processes and shielding effects are incremental in nature.

2.2 Microtomography

Computed tomography is a technique that allows the 3D distribution of some parameters of the object to be obtained from its angular projections [34, 35]. In the case X-ray absorption is utilized, reconstructed volumes will contain linear attenuation coefficients of the sample. There are different ways to realize computed tomography in practice, including different configurations of X-ray beams and detector elements [11]. Computed tomography has been used widely in medicine since the 1970's, when first commercial medical systems appeared. It is also used as a non-destructive evaluation technique in industrial applications [36].

Absorption CT is based on the mathematics of the Radon transform [37]; this transform reconstructs the spatial distribution of linear attenuation coefficients in the sample from the line integrals recorded for a number of sample (or combined X-ray source - detector) rotations. In one reconstruction method, Fourier transforms of a set of line integrals recorded with a detector for a series of projections over 180° of view (although this number may vary for different data collection schemes such as cone or fan beam configuration), are combined in frequency space and backprojected into direct space, to yield a map of linear attenuation coefficients μ within the sample's cross-section.

X-ray microtomography is an evolving form of computed tomography that gives quantitative information on linear attenuation coefficients at a scale of 0.3 to 100 μm [38], and commercial microtomography instruments using X-ray tubes have been available for several years. Depending on the size of a sample, the commercial systems can provide spatial resolution down to $\approx 10\mu$m [39, 40]. The disadvantage of such instruments is that the intensity of the X-rays generated from an X-ray tube source does not allow X-ray energy filtering to be performed, which in turn introduces artifacts in the reconstructed data.

Higher resolution, higher contrast reconstructions continue to be performed using synchrotron X-radiation. The advantage of the synchrotron radiation is that it provides a monochromatic X-ray beam, which has much higher intensity than the microfocus tubes. Third generation synchrotron sources also provide the additional advantage of very low angular divergence X-rays. One problem of the third generation synchrotron sources is that small defects in the optics can introduce non-uniform beam artifacts. Rapid temporal changes in the distribution of X-ray intensity within the beam sometimes results and these are difficult to correct.

Another important factor in the development of the CT systems is the detector. Initially detectors were 0D (standard scintillation or proportional detectors) and 1D

(linear pin diode arrays, etc.). At the present time, however, most of the microtomography setups use 2D CCD detectors, which allow much faster data collection for volumes of material. With the earlier detectors, microtomography data were collected slice by slice and analysis focused on what was seen in each slice. Now most studies are volumetric and employ 3D analysis techniques.

Microtomography was successfully used for studies of fatigue crack closure in 2090 notched tension and compact tension specimens [8–16]. These studies revealed where (in 3D) and at what loads roughness-induced crack closure occurs and are summarized in Section 2.3.

Microtomography has a number of limitations when studying compact tension specimens. The greatest challenge comes from the shape of the specimen. The shape – aspect ratio of the compact tension specimen is very unfavorable for computed tomography and limits the crack opening sensitivity that can be obtained with microtomography. The reason behind this is that when the sample is oriented in such a way that its longest dimension is parallel or nearly parallel to the direction of X-ray beam, the transmitted X-ray intensity is greatly attenuated and, as a result, contrast may be insufficient to detect the crack. The minimum detectable change in intensity ΔI for transmitted X-ray intensity I defines the sensitivity level $\Delta I/I$ which is directly related to the quotient of the minimum detectable change in thickness Δt and the sample thickness t. For a given $\Delta I/I$ defined by the CCD detector well depth and the image acquisition time (itself limited by the need to avoid saturating the detector in positions where no part of the sample intersects the beam), increased sample thickness means that Δt is increased and the minimum detectable crack opening increases as well. This effect is most severe where the crack is closest to being closed, i.e., precisely those sections of the crack that are of greatest interest in fatigue crack closure studies.

This phenomenon is demonstrated in Figure 1. The compact tension sample is

represented as a rectangle with constant density and linear attenuation coefficient, and the crack is represented as a small circle in the middle of the rectangle. The crack is assumed to have zero X-ray attenuation and projection radiographs of this model are taken in an ideal monochromatic tomography apparatus for an angular range of 180 degrees. Assuming the smallest contrast that detector can detect is 1%, the crack will only be seen when the ratio of the circle diameter to the path traversed by the beam is more than 0.01 according to Beer's equation ($I = I_0 \exp(-\mu t)$, where I_0 is the intensity of the incident radiation, μ is the linear attenuation coefficient of the sample, and t is the sample thickness). This condition is satisfied for only some of the projections, and the result is that errors will be introduced in the reconstructed image.

Another CT limitation is that the sample must remain in the field of view of the detector for all angular orientations; otherwise, significant and sometimes difficult to predict artifacts are introduced. This dictates that the voxel (volume element) size is the sample diameter divided by the number of detector elements spanning the object in the plane of reconstruction. In other words, a detector with 1K elements in the plane of reconstruction can reconstruct a 3 mm diameter object with 3 μm voxels. Thus, this limitation negatively affects resolution for relatively large aspect ratio specimens, such as the compact tension specimen, and further decreases sensitivity to the cracks. Alternative approaches such as that of Davis and Elliott [41] can ameliorate this limitation but complexities of the hardware or of image processing appear to have limited widespread adaptation of these approaches.

The limitation in sensitivity and spatial resolution of absorption microtomography prevents detection of details connected with parts of the crack with small openings. This is especially true for regions of the crack close to the crack tip, since the crack openings for a specific load are the smallest there, and for small loads when the crack is mostly closed. Obtaining more detailed data for these cases will provide more

insight into the crack behavior at initial stages of crack opening and where closure phenomena are expected to have the greatest effect on crack extension "driving force", i.e. the stress intensity range ΔK.

2.3 Prior absorption microtomography studies of crack closure

Breunig *et al.* [13] reported the first in situ absorption CT imaging of samples under load and showed that changes in crack images could be observed with absorption microtomography as a function of applied load and of position within the sample. Samples were machined from the center of a 12.5-mm-thick plate of 2090 T8E41 and loaded in the L (rolling) direction. A notched tensile sample geometry (2.1 mm diameter at the base of the notch) was used because it provided optimum sensitivity and spatial resolution for absorption microtomography and provided a well-defined volume in which to find the crack: the authors of this study were well aware that this geometry was problematic in terms of simple yet precise calculation of quantities such as ΔK and ΔK_{eff}. The load-deflection curve of the fatigue-cracked sample was bilinear, indicating the presence of crack closure with closure load $\sigma_{\text{cl}} \approx 0.47\,\sigma_{\max}$, where $\sigma_{\max}$ was the maximum applied stress during the last increment of crack propagation. In a custom-designed load frame described elsewhere [42], the crack was imaged under load with 6x6x6 μm voxels and was highly visible at the highest loads. The crack was very non-planar, as expected, and as the load decreased, more and more sections of the crack became invisible, indicating that physical closure of the crack was occurring at loads above the macroscopically determined closure load.

After this initial report on the feasibility of absorption microtomography detection of crack changes in crack opening, Guvenilir *et al.* [9] quantified the amount of crack opening as a function of applied load and 3D position. The position of the crack in the interior of a notched tensile sample (the same sample as in Breunig *et al.* [13])

was mapped in 3D and represented as a 3D mesh for several loads simulating different stages of a fatigue cycle. Crack face separations as a function of position were quantified by summing, along the direction of the load axis, the fractions of adjacent voxels partially occupied by the crack. Substantial contact on asperity faces was shown to exist even at the maximum load of the fatigue cycle, and crack face contact appeared to occur on both mixed mode I–III and I–II surfaces. Physical closure at portions of the crack tip preceded (during unloading) the bend in the sample's load-displacement curve and that the mixed mode I–III surfaces began to carry significant load in the region near the bend of the load-displacement curve.

Guvenilir *et al.* [12] studied a second notched tensile sample, this time using synchrotron radiation instead of X-rays from a tube. In this sample, the fatigue crack surfaces were relatively planar and deviated little from the plane containing the tip of the notch. This geometry was quite different from that in the notched tensile sample described above whose surface was dominated by steep asperities, and the difference was attributed to the normal variability seen in crack face morphology for AA 2090 samples from plate centers.

Guvenilir *et al.* [14] studied a compact tension sample with absorption microtomography, also using a microfocus X-ray source; and the 2.1 mm thick, 20.3 mm wide (notch-tip to back-face) sample was reconstructed at several loads with 20 μm isotropic voxels. Considerable crack branching was detected in the compact tension sample, and, where the crack propagation direction changed, various patterns of contact (discussed below) were observed.

The results for the three samples described above showed two principle types of behavior: regions where the crack has mostly mode I character and regions where crack surface has mixed character with crack path close to parallel to the load axis [10]. The dimensions of these regions determined from the absorption microtomography data was of the order of 1 mm. During the unloading portion of a fatigue cycle,

crack morphology governs whether the crack faces contact at irregular locations as the load decreases (in asperity-dominated regions of the crack) or whether the crack closes relatively uniformly from its tip as the load decreases (in planar sections of the crack).

Morano *et al.* [15, 16] used absorption microtomography and in-situ loading of compact tension samples to compare fatigue crack closure for a crack grown at a low load ratio and one grown at high load ratio. Those investigators concluded that the complexity of the closure processes is consistent with the strong macrotexture present. As cited above, the macrotexture in the center of plates of 2090 T8E41 and the planar slip character of deformation in this alloy can explain the angle of the faces of asperities. As described below, mesotexture within the samples (i.e., a spatial scale of texture between orientations of individual grains and sample average texture) appears to drive the formation of features such as asperities; features which dominate the fracture surface and which are tied to increased crack closure.

Haase *et al.* [6] used synchrotron microbeam X-ray diffraction mapping to investigate the origin of the large asperities required to produce significant fatigue crack closure effects in AA 2090 T8E41 samples. Haase *et al.* [43] focused on the role of individual grain orientations (microtexture) and of average orientation within small groups of adjacent grains on the crack's path through a sample. They found asperities in the center of plates of AA 2090 did not form at random within the volume of material through which the crack grew. Instead, mesotexture within this volume dictated where large and small asperities developed. The characteristic mesotexture (leading to formation of asperities) consisted of stacks of 5 to 20 adjacent, pancake-shaped grains that were so highly aligned that they could be regarded as near-single-crystal volumes. Approximately 45% of the volume in the center of AA 2090 plates consisted of such volumes, this result was consistent with macrotexture represented by pole figures and the large asperities on the crack surface consisted of grains of only one

orientation type.

Ignatiev *et al.* [7] investigated whether the AA 2090 mesotexture - closure correlation was nothing more than a coincidence, that is, whether this mesotexture is seen in other alloys which do not show pronounced crack closure. The first material that was investigated in this study, AA 8090 (which is also an aluminum-lithium alloy as AA 2090), has similar microstructure and macrotexture as AA 2090, however the amount of crack deflection and asperity size are lower for AA 8090 [2]. Grains in AA 8090 have similar shape as in AA 2090, however their size was smaller. Grain dimensions for AA 8090 were 1 mm in the plate L direction, 165 μm in the plate T direction and 20 μm in the S direction. Macrotexture in AA 7055 (which emerged as a result of modifications to alloy AA 7050) is similar to that in AA 2090, but fatigue crack growth rates, fatigue crack path and grain morphologies differ considerably for AA 7055 and AA 2090 [44] with AA 7055 having more equiaxed grains.

X-ray microbeam diffraction mapping of samples of AA 8090 (macrotexture and grain morphology similar to that of AA 2090 but much smaller crack deflections and asperity size) and of AA 7055 (macrotexture also similar to that in AA 2090, but fatigue crack growth rate, the fatigue crack path and grain morphologies different from those in AA 2090) showed that AA 8090 had considerably less near single-crystal volume ($\sim$ 10 vol. % vs. 45 vol. % in AA 2090). Data from AA 7055 material showed that the near single-crystal mesotexture was not an artifact of the method: no near-single crystal mesotexture was found, which is not surprising given the difference between AA 7055 and the aluminum lithium alloys. The differences in fatigue crack propagation between AA 2090 and 8090 appeared to be due to the different levels of near single-crystal mesotexture.

Since earlier, preliminary reports were prepared of the data presented below [45], Toda *et al.* [46] reported absorption microtomography studies of a fatigue crack in aluminum and took the approach of cutting a small section from the sample and

examining this small parallelepiped (containing the crack tip) at very high spatial resolution (0.7 μm voxels). It remains an open question as to whether the crack observations are valid: has the removal of the constraint from surrounding material changed the near-crack volume or has the cutting process changed the material around the crack? Avoiding these worrisome considerations was the reason that the present stereometry approach was developed.

Another example of microtomography applied to fatigue crack characterization, the interaction of a short fatigue crack with grain boundaries in a cast aluminum alloy was carried out using synchrotron X-ray microtomography [47]. The aluminum grain boundaries were decorated by liquid Ga which served as a contrast agent for X-rays. As a result of the study, 3D shape of the fatigue crack were correlated to the grain structure of the material.

2.4 Phase contrast imaging

There has been an upsurge of interest in X-ray phase contrast imaging lately due to availability of third generation synchrotron sources. The high degree of collimation, low X-ray beam angular divergence and small source size of these synchrotrons allow phase information to be extracted from the beam that has passed through the object of interest. Since the phase shift φ of the beam is affected by the electron density, important information about the object can be obtained.

Like electromagnetic waves in the visible light range, X-rays refract. The complex index of refraction can be written as $n = 1 - \delta - i\beta$. Changes in the real part δ of the deviation of the index of refraction from unity are what produce phase contrast in X-ray imaging. The imaginary part of the index of refraction β is proportional to the linear attenuation coefficient μ, and changes in μ are what is measured in absorption microtomography. In many applications, phase contrast reveals more subtle changes in the sample than absorption contrast; this results from the fact that δ is several

orders of magnitude larger than μ for light elements. For aluminum and 30 keV X-rays, the ratio of δ to β equals 7.9×10^2. Therefore, phase contrast techniques allow one to detect very small changes in material density or composition, changes that absorption based methods would not reveal.

With respect to studying compact tension specimens of Al-Li, it allows detection of cracks that are not visible with conventional absorption radiography. Another advantage of using phase contrast in conjunction with stereometric reconstruction is that sharp discontinuities that introduce artifacts and decrease image quality of the reconstructed slices in absorption tomography do not appear in the phase methods.

There are three distinct experimental methods used for X-ray phase contrast imaging. In order of increasing experimental complexity, X-ray phase imaging can be performed with the propagation, diffraction-enhanced (also termed analyzer crystal), or interferometer methods which directly measure $\bigtriangledown^2\varphi$, $\bigtriangledown\varphi$ and φ, respectively [48].

2.4.1 Physical Principles of the Phase Contrast Formation

In this sub-section, physical principles of the x-ray phase contrast image formation will be discussed.

X-rays are electromagnetic waves in the range of wavelengths from 0.1 to 10 Angström. Its behavior and propagation in space can be described by a wave function $\psi(r)$, which is generally a complex function of spatial coordinates. X-ray detectors can only measure the intensity of the wave function, i.e. $|\psi(r)|^2$, so the phase information which is contained in the imaginary part of the wave function is lost. However, it can be recovered by utilizing a number of diffraction effects, one of which, so called Fresnel diffraction or free space propagation, is described here.

Electromagnetic wave behavior is governed by the wave equation. For an electric field vector $\vec{E}$, it can be written as

$$\frac{\partial^2\vec{E}}{\partial x^2} + \frac{\partial^2\vec{E}}{\partial y^2} + \frac{\partial^2\vec{E}}{\partial z^2} = \varepsilon\mu\,\frac{\partial^2\vec{E}}{\partial t^2} \tag{1}$$

where ε is the permittivity (or dielectric constant) and μ is the magnetic permeability of the medium through which the wave is propagating.

Vector properties of the electric field can be neglected, assuming unpolarized radiation. Then for wave function, the following can be written:

$$\nabla^2\psi(r) = \frac{\partial^2\psi(r)}{\partial t^2} \tag{2}$$

The Kirchhoff formulation is based on the Huygens' principle of wave propagation, i.e. each point of the wave front serves as a scattering point for the original wave and creates secondary waves, which in sum give the new wave front. It is derived from an integral form of the wave equation.

Assuming that the radiation wavelength is much smaller than the dimensions of the scattering object, the Kirchhoff formula for the wave function at the coordinate (x, y) can be written as follows [49]:

$$\psi(x,y) = \frac{i}{2\lambda}\iint q(X,Y)\,\frac{\exp(-2\pi ikr_q)}{r_q}\,\frac{\exp(-2\pi ikr)}{r}\times$$

$$\times\left\{\cos(\widehat{\vec{Z},\vec{r}}) + \cos(\widehat{\vec{Z},\vec{r}_q})\right\}\,dXdY, \tag{3}$$

where the scattering object is assumed to be a 2D and planar body, lying in the (X–Y) plane, which has a complex transmission function $q(X, Y)$, which relates amplitude and phase of the wave function of the scattered wave just after the object to the amplitude and phase of the incident wave. Here $\vec{r}$ is the vector from the point on the object to the radiation point source, and $\vec{r}_q$ is the vector from the object to the observation point. This is illustrated in the Figure 3.

The transmission function $q(X, Y)$ in Equation (3) can be written as [50]

$$q(X,Y) = A(X,Y)\,\exp\left[i\varphi(X,Y)\right] \tag{4}$$

with amplitude $A(X,Y)$ and phase modulation $\varphi(X,Y)$ given by

$$A(X,Y) = \exp\left[-\frac{1}{2}\int \mu(X,Y,Z)\,dZ\right] \tag{5}$$

and

$$\varphi(X,Y) = -\frac{2\pi}{\lambda}\int \delta(X,Y,Z)\,dZ, \tag{6}$$

where μ is the linear absorption coefficient, λ is the radiation wavelength and δ is the real part of the deviation of the index of refraction from unity in following formula for the index of refraction: $n = 1 - \delta + i\beta$, where n is the index of refraction of the object and its imaginary part β is related to the absorption coefficient as follows: $\beta = \frac{\mu\lambda}{4\pi}$ [50]. From the definition of the transmission function, the wave leaving the sample $\psi_o(\vec{r})$ can be related to the incident wave $\psi_i(\vec{r})$ as

$$\psi_o(\vec{r}) = q(\vec{r})\;\psi_i(\vec{r}). \tag{7}$$

In the case of the wavelength much smaller than the object dimensions, small angle scattering from the object can be assumed. Then, in the case of a plane incident wave, $\cos(\widehat{\vec{Z},\vec{r}}) \approx 1$ and $\cos(\widehat{\vec{Z},\vec{r_q}}) \approx 1$.

The distance between the scattering point and detector can be written as

$$r = \left(R^2 + (x-X)^2 + (y-Y)^2\right)^{1/2}, \tag{8}$$

where x and y are coordinates of the point on the observation plane and R is the distance between the object and the observation plane. Again, for small angle scattering, assuming x-rays approximately parallel to the $\vec{Z}$ direction, R can be substituted for r in denominator of (3), and in the exponent, using Taylor series expansion, it can be rewritten as

$$r \approx R + \frac{[(x-X)^2 + (y-Y)^2]^{1/2}}{2R}, \tag{9}$$

so the equation for the wave function of the scattered wave will be

$$\psi(x,y) = \frac{i \exp(-2\pi i k R)}{R\lambda} \times$$

$$\times \iint q(X,Y) \, \exp\left\{\frac{-2\pi i \left[(x-X)^2 + (y-Y)^2\right]}{R\lambda}\right\} dX dY \tag{10}$$

It can be seen from equation (10), that the wave function and, correspondingly, the intensity of the scattered beam depends on the distance from the sample to the detector plane. Strictly speaking, this equation is valid only for a limited range of sample – detector distances. Starting from a certain sample – detector distance, Fraunhofer diffraction dominates and equation (10) is no longer valid.

The beam intensity distribution at the detector plane can be directly calculated from the equation (10), if the sample transmission function $q(X,Y)$, sample – detector distance and radiation wavelength are known. However it is a computationally inefficient way of calculating the intensity distribution, since for each (x,y) coordinate on the detector plane, the double integral over all positions of the sample in (X,Y) plane has to be calculated. A quicker and more efficient way of doing this, is to use calculations in frequency domain with the help of Fourier transformations, for which there exists a number of popular computational algorithms, such as the Fast Fourier Transforms (FFT), which are very fast, efficient and are easily realized on different computer platforms.

Calculation of the beam intensity distribution via FFT can be carried out as follows. Equation (10) can be represented by a convolution of functions $f(X,Y)$ and $g(x,y)$ in the 2D domain:

$$f(x,y) * g(x,y) = \iint f(X,Y)\, g(x-X, y-Y)\, dXdY, \tag{11}$$

where symbol $*$ denotes convolution operator.

Comparing equations (10) and (11), the following equation can be written

$$\psi(x,y) = q(x,y) * \left[\frac{i \exp(-2\pi ikR)}{R\lambda} \exp\left\{ \frac{-2\pi ik(x^2+y^2)}{2R} \right\} \right] \tag{12}$$

The function in square brackets in last equation can be termed the propagation function and will hereafter be written as $p(x,y)$. In the context of Fresnel diffraction, it can be thought of as a wave function of a scattered radiation from a point source.

According to one of the properties of Fourier transform, convolution in direct space is equivalent to multiplication in reciprocal, or frequency space; i.e. if $Q(X,Y)$ is the Fourier transform of $q(x,y)$, and $P(X,Y)$ is the Fourier transform of $p(x,y)$, then

$$\Psi = Q\, P, \tag{13}$$

where Ψ is the Fourier transform of ψ.

Thus the calculation of wave function is reduced to obtaining the Fourier transforms of the transmission and propagation functions, multiplying them and taking the inverse Fourier transform.

$$Q = FT(q) \qquad P = FT(p) \tag{14a}$$

$$\Psi = Q\, P \qquad \psi = IFT(\Psi), \tag{14b}$$

where FT stands for the Fourier transform and IFT — the inverse Fourier transform.

The resulting intensity can be obtained as the square of the modulus of wave function.

$$I = |\psi(r)|^2 \tag{15}$$

These calculations can be modified for the use with experimental phase contrast methods other than propagation. In this case, instead of using propagation function described above, the corresponding function that describes wave behavior after exiting the sample should be convolved with the sample transmission function.

2.4.2 Interferometer method

This method uses three aligned parallel perfect crystals as an interferometer system [17, 18, 20, 51–55]. In the Bose–Hart interferometer, the first crystal element (sometimes a pair of crystals) serves as a beam splitter, the second one as a mirror and the third as an analyzer (see Figure 4a). The first crystal splits the monochromated beam into two separate beams, and the object of interest is placed into one of the beam paths, introducing phase shift between two beams and distorting wave front. The altered and unaltered beams are brought back together by the mirror, and an interference picture is formed by an analyzer crystal which is recorded by the detector.

A limitation of this method is that it requires perfect alignment and stability on the order of 10^{-2} nm. Shifts of temperature on the order of 0.1°C are sufficient to destroy the interferometer's stability. Fabrication of this kind of interferometer is complicated.

2.4.3 Diffraction-enhanced imaging

This method of phase-contrast imaging uses a perfect crystal as an analyzer for X-ray beam that passed through the sample [48, 56–58]. X-rays can originate from either a synchrotron source or microfocus tube. In the case of synchrotron radiation, the beam is monochromated with a monochromator tuned to the energy of interest, depending on the type of the sample and features of interest. The sample is placed between

the monochromator and analyzer crystal (see Figure 4b). Due to variations in the index of refraction, there will be a slighty diverging array of X-ray beams exiting from the sample. The analyser crystal is aligned in such a way that it would satisfy Bragg condition for a reflection that produces sharp rocking curve. To increase the contrast of the resulting image, the analyzer is rotated so that its orientation would correspond to the middle of the flanks of this sharp reflection. This produces sharp contrast between X-ray beams that propagate in different directions. There are two major sources of contrast in the resulting image — one is due to the differences in coefficient of absorption, and another arises from the variation of index of refraction. It is possible to separate two effects by taking measurements on the low angle and high angle flanks of the analyzer rocking curve and carrying out simple image transformations. These two types of images complement each other. The advantage of this method is that inelastically scattered x-radiation from the sample does not affect the results, since its angular divergence from the initial beam direction is much higher than the angular width of the analyzer rocking curve and thus it is not diffracted by the analyzer crystal.

2.4.4 Propagation method

The propagation method of X-ray phase contrast image formation is based on what is called the in-line holography effect: object situated in the highly coherent X-ray beam introduces a phase shift, which can be detected at some distance behind the sample due to Fresnel diffraction [19, 50, 59–66]. The main advantage of this method compared to the other phase contrast techniques is its experimental simplicity. No additional X-ray optical elements, such as mirrors or analyzer crystals, are needed (see Figure 4c), and, experimental system setup and alignment are correspondingly simple. Despite its simplicity, the propagation method has sufficient sensitivity to detect abrupt changes in index of refraction. It is also possible to record phase

contrast images using microfocus X-ray tube [67] or SEM source [68]. The theoretical basis behind the phase contrast imaging in Fresnel regime with respect to imaging planar 2D objects was described above in Section 2.4.1.

2.4.5 Phase contrast imaging applications

Most applications of X-ray interferometry have been with biological soft tissues. This technique was especially advantageous in cancer studies and mammography [19, 20, 69]. Current X-ray absorption radiography techniques often fail to distinguish between tissues with slightly different absorption coefficients. Measurement of phase contrast, however, allows detection of small changes in X-ray beam phase. By rotating the specimen and recording interference pattern for each rotation angle, it is possible to reconstruct 3D distribution of phase changes inside the sample, which greatly enhances visibility of edges between different regions.

Diffraction-enhanced phase contrast imaging was used on various biological samples, that included breast tissues with tumors and breast tissue phantoms [57]. Conventional radiographs, apparent absorption radiographs and refraction radiographs were taken. The apparent absorption radiograph showed more contrast for the tumor than the conventional radiograph. The refraction radiographs of the same specimen provided even more information, since it showed small fibrils which were not observable in the conventional radiograph. Presence of small fibrils is a possible indication of a small, otherwise undetectable tumor. Mechanisms of insect respiration were studied in real time using radiographs recorded with the phase propagation technique [70].

Phase-contrast X-ray microtomography was used to study a cancerous rabbit liver using a synchrotron X-radiation [18]. The cancer lesion was easily distinguished from the normal liver tissue. Comparison between a phase-contrast X-ray microtomography image and an optical image of a human breast tumor was reported in [20]. It was shown that various structures of breast lesions were described almost as clearly

as with an optical micrographs.

In the area of materials science, characterization of the internal damage in a metal matrix composite sample (Al 6061 alloy reinforced by SiC particles) was conducted using phase contrast microtomography [21]. Particles could be visually separated from the matrix and internal damage from the loading could be seen. Cloetens *et al.* [71] used phase contrast for imaging cracked silicon single crystal. The surface morphology, individual grains and cracks in polycrystalline diamond samples have been imaged by a series of X-ray phase-contrast techniques [72].

2.5 Stereometry

The problem of inferring information about the 3D properties of an object from a number of 2D projections is well known. Human vision is one example: the brain processes 2D images of a scene from each eye to extract 3D geometry and location of each object in a scene. This principle is used in different fields of science where exact information about object location in space is needed. The same effect can be achieved by utilizing only one detector and recording several images of the object from different angles or positions, or by recording projection or reflection images of an object while rotating it (tilt-only). The former is used in air- and space-based surveys of the Earth surface and the latter in microscopy (e.g. [73]). The tilt-only approach is used in this study.

For the tilt-only approach, if the position of the rotation axis is not known, three images of the object made at different tilting angles are needed. The position of the object's rotation axis is determined from measurement of the position of a well-defined feature in three images made at different tilting angles. This knowledge is used to determine positions of any other feature of interest of the object using any two projections. The equations governing the position determination are covered in Section 3.6.

The number of views given above are minimums. More accurate position determination should result from use of more views than this minimum (provided, of course, that the random error does not dominate).

CHAPTER III

MATERIALS AND METHODS

The overall aim of this study was to demonstrate and apply new approaches to the 3D study of crack geometry and opening as a function of applied load in a common fatigue crack growth specimen, the compact tension sample. The first absorption microtomography measurements before and after crack extension are reported for compact tension sample CT-32M. Comparison of the spatial distribution of crack openings before and after extension was used to estimate microtomographic sensitivity to crack opening and determination of how the pattern of crack openings changes with crack growth and how it relates to crack path and geometry.

Second, this study focused on extracting 3D crack positions from synchrotron X-ray phase contrast microradiographs using stereometry methods mentioned in Section 2.5. The possibility of measuring crack opening using phase contrast imaging was also investigated. Absorption microtomography of the same sample under load was used to check the stereometry results (3D crack face positions) and the crack openings.

3.1 Samples

Small versions of the compact tension samples were used in this study. They were cut from the center of 12.7 mm thick plate of AA 2090 T8E41 alloy such that the load axis coincided with the rolling direction of the plate (L) and the plane of the specimen would be perpendicular to the short transverse direction (S) of the plate. According to this geometry, the crack propagates in the transverse direction (T). Samples were scaled and machined according to ASTM Standard E399-83 with thickness of 2.7 mm,

length of 31.8 mm and width of 30.5 mm (Figure 2).

The samples were precracked, and the fatigue crack was grown at 20 Hz, with a load ratio $R = 0.1$ (sample CT-32M) and $R = 0.75$ (CT-41M). Here "M" denotes a sample taken from the middle of the plate. Crack lengths for different samples vary from several millimeters to up to 6 mm. After fatigue crack was grown, 5 mm length was cut off from the backface of the sample CT-41M to reduce X-ray paths through the sample.

For one specimen (CT-32M), additional fatigue crack growth was carried out after the first set of absorption microtomography data was collected. A second set of absorption microtomography data was then collected on CT-32M. Data on a second specimen, CT-41M was used for comparison with the phase contrast method (absorption microtomography and measurement of opening as a function of applied load was already performed by Morano *et al.* [15, 16].

Table 1 contains the list of the samples available for use along with the experiment information. Table 2 lists the phase contrast measurements performed on these samples. Only data from the samples described above were analyzed.

3.2 Absorption microtomography measurements

The experimental part of this thesis that involves absorption computed tomography measurements, was carried out using a time-delay integration microtomography apparatus with a cone X-ray beam at the Queen Mary, University of London, England. The size of resulting voxels (volume elements) varied for the different samples. For sample CT-41M voxel size was 58 μm and for sample CT-32M voxel size was 29.10 μm before crack extension, and 23.23 μm after crack extension. In order to be able to compare these two data sets, data resampling was carried for the data set before crack extension to 23.23 μm voxel size using cubic interpolation. Details on this

Table 1: List of samples that are used in the measurements and loading for each sample.

Sample ID	Sample loads, kgf			Additional experiment information
	absorption micro-CT		phase contrast	
	before the crack extension	after the crack extension		
CT-32M	0.0		-	-
	8.5	8.0	-	-
	22.6	22.7	-	-
	37.2	37.5	-	-
	51.8	52.6	-	-
	60.6	66.3	-	-
		84.1	-	-
CT-41T	0.0	-	-	-
	8.1	-	-	-
	23.0	-	-	-
	37.2	-	-	-
	51.8	-	-	-
	61.3	-	-	-
CT-41M	0*	-	0.0	rotation
	6*	-	6.0	around y-axis
	10*	-	10.3	for each load
	15*	-	15.1	
	20*	-	20.0	
	25*	-	24.9	
	30*	-	30.0	
	35*	-	35.0	
	40*	-	40.0	
CT-37	-	-	0.0	rotation
	-	-	2.0	around y-axis
	-	-	10.0	for each load
	-	-	20.0	
	-	-	30.0	
	-	-	40.6	

* these measurements were made in previous investigation [16]

Table 1: (cont.) List of samples that are used in the measurements and loading for each sample.

Sample ID	Sample loads, kgf			Additional experiment information
	absorption micro-CT		phase contrast	
	before the crack extension	after the crack extension		
CT-39	-	-	2.1	rotation
	-	-	9.9	around y-axis
	-	-	19.9	for each load
	-	-	29.8	
	-	-	40.4	
	-	-	50.1	
	-	-	60.1	
	-	-	72.1	
	-	-	81.7	
	-	-	90.7	
	-	-	101.5	
CT-33	-	-	2.2	
	-	-	10.0	
	-	-	20.5	
	-	-	30.7	
	-	-	40.4	
CT-2	-	-	2.2	
	-	-	10.3	
	-	-	20.2	
	-	-	30.1	
	-	-	40.5	
CT-44M	-	-	2.1	
	-	-	10.0	
	-	-	20.0	
	-	-	30.0	
	-	-	40.0	
	-	-	50.0	
	-	-	60.0	
	-	-	70.5	
	-	-	80.9	
	-	-	89.6	
	-	-	101.5	

Table 2: List of phase contrast measurements.

Sample	Crack length, mm	Measurements without load	Measurements with load[a]
CT-2			-Map of the crack -Rotation about y-axis from $-20°$ to $20°$ with $5°$ step (all positions)[b]
CT-33		-Map of the crack -Rotation about x-axis from $0°$ to $45°$ with $1°$ step (one position) -Rotation about y-axis from $-45°$ to $45°$ with $1°$ step (one position)	-Map of the crack -Rotation about y-axis from $-20°$ to $20°$ with $2.5°$ step (one position)
CT-37			-Map of the crack -Rotation about y-axis from $-20°$ to $20°$ with $5°$ step (all positions)
CT-39		-Map of the crack -Rotation about x-axis from $-45°$ to $45°$ with $1°$ step (all positions)	-Map of the crack -Rotation about y-axis from $-30°$ to $30°$ with $1°$ step (one position)
CT-41M		-Map of the crack -Rotation about x-axis from $-45°$ to $45°$ with $1°$ step (all positions)	-Map of the crack -Rotation about y-axis from $-15°$ to $45°$ with $1°$ step (one position)
CT-44M		-Map of the crack -Rotation about x-axis from $-45°$ to $45°$ with $1°$ step (one position)	-Map of the crack -Rotation about y-axis from $-15°$ to $45°$ with $1°$ step (one position)

[a]Measurements in this column were made for each load listed in Table 1

[b]These measurements were made only for two loads — 20.2 kgf and 40.5 kgf

apparatus are reported elsewhere [41]. To study the crack opening pattern, a loading stage was used [15], and the tomography measurements were conducted in-situ, that is, the sample was held under the constant load during a round of tomography measurements. Measurements were repeated for a number of different loads that correspond to different portions of the fatigue cycle. In total, each sample was measured under six different loads, up to 185 lbs, and Table 1 lists the samples and loads at which data were collected. The resulting projections were reconstructed using filtered backprojection algorithm [35] into a 3D matrix of linear attenuation coefficients.

3.3 Phase contrast microradiographs

The phase contrast part of the proposed experiments consisted of aluminum compact tension samples imaged both with and without load, simulating conditions during the fatigue cycle. Preliminary studies showed that the cracks in aluminum specimens of 3 mm thickness are clearly visible in propagation phase contrast imaging mode and that the resulting contrast reflects changes in crack opening depending on the amount of load that is applied to the samples. Phase contrast measurements were conducted at the beamline 1 ID-C and 2-BM-B of the APS (Advanced Photon Source) at the Argonne National Laboratory. A schematic of the experimental layout is shown in Figure 5. The distance from the source to the sample was about 60 meters and the imaging system was mounted on an optical rail parallel to the axis of the X-ray beam so that the detector - sample separation could be varied for optimum phase contrast.

The detector system consisted of a CCD camera coupled with a Ce-doped YAG crystal that is used as a scintillator. The scintillator crystal converted X-ray radiation into a visible light, and an optical microscope objective magnified the image that is detected by the CCD camera. The CCD camera had 1024x1024 pixels, had a dynamic range of 16 bits and was cooled by liquid nitrogen to reduce the thermal noise in the camera's electronic components. The field of view and image resolution

were controlled by the magnifying objective.

Station 1 ID-C receives monochromatic radiation, whose energy is tunable in the range from 10 to 80 keV. For the experiments with aluminum compact tension specimens, 30 keV photons were used, since this energy satisfies the condition of $\mu t < 2$ (μ is the aluminum linear absorption coefficient and t is the length of the X-ray path through the sample) [74] to produce the best contrast for this type of material and specimen geometry.

Samples can be mounted on a translation stage with three degrees of freedom equipped with computer-controlled stepping motors. For measurements under load, a load frame was used, which was specially designed for use in synchrotron radiation experiments. It had a standard clevis and pin assembly for mounting the sample. After changing the load on the sample, the sample was allowed to stabilize. All hardware devices, including monochromator and beam shutters, were controlled by the software.

A number of measurements were conducted in the phase contrast regime. To determine the spatial orientation of the crack surface, images for a number of sample orientations were taken. There are three rotational degrees of freedom associated with the sample, however only two of them can be used to obtain 3D information about the crack. They correspond to rotation about **x** and **y** axis as shown in Figure 6. These axes of rotation also satisfy the condition that they should be parallel to the plane of the detector. Both of these rotations were used for experiments that do not involve specimen loading. Use of the loading cell limited the choice of possible rotation axes to **y** axis.

The 3D sample physical characteristics are projected onto the 2D detector by the X-ray beam. In the phase contrast regime it is the information about discontinuities in the index of refraction that is projected, and, correspondingly, information about

sharp changes of orientation in the crack surface. The coordinates on the 2D projection (detector) of the crack features were measured in the individual radiographs.

Determination of the point coordinates for crack features in individual images is subject to random errors which directly affect precision of the resulting crack position. To decrease the influence of random errors, regression analysis on the input data was conducted: coordinates of each visible crack point of interest on the radiograph were measured at several sample orientations at which this point was clearly visible (at some sample orientations it may be obscured by other crack features), and the regression analysis was used to determine the mean value of the point coordinates for each angle of rotation, spanning 180 degrees, and the standard data deviation.

Since the CCD camera had a fixed number of detector elements, spatial resolution and the size of the field of view were inversely proportional. Features that lay away from the rotation axis moved out of the field of view of the detector when the sample rotated beyond a given angle, thus limiting angular range over which coordinates of the feature's projection could be measured. The technique of image "stitching", when images of several neighboring fields of view of the sample are joined together, was used in order to obtain the images of the whole crack, whose length exceeded detector field of view.

3.4 Phase contrast image processing

The main factor that degraded quality of radiographs was non-uniformity of the incident X-ray beam. While the synchrotron X-ray distribution is more or less uniform at the X-ray source, imperfections of optical elements along the beam line, such as thickness variations of beryllium windows, contamination on the mirrors and monochromators, variation in reflectivity of mirrors and monochromators etc. introduce small deviations in the spatial distribution of X-ray intensity. After the distance of several tens of meters when the beam reaches the sample, these deviations propagate

to horizontal streaks. This is another manifestation of phase contrast; this time it is destructive for the sample imaging.

Some images were normalized to reduce effects of the beam and detector imperfections. Along with the image of the sample, a "white" field (image of the beam without a sample) and a "dark" field (no beam) image were recorded, and the normalized image was calculated by using the following equation for each pixel in the image:

$$\text{Normalized} = -\log \frac{\text{image} - \text{dark}}{\text{white} - \text{dark}} \tag{16}$$

Examples of normalized images can be seen on Figures 32 – 34. Use of Equation (16) did not work well for many images due to the motion of the streaks over time and the effectiveness of the technique depended in part on the detector field of view (it worked better for small fields of view where the streak size was comparable to that of the field of view).

High-pass image filtering using a 40^{th} order Butterworth filter was done to improve contrast for most of the images. Since beam streaks have primarily low spatial frequency and crack contrast lines have high spatial frequency, then by using high-pass filter it is possible to significantly reduce appearance of artifacts caused by the beam non-uniformity. The quality of the images can be increased even more by using directional-sensitive filter, that is, taking into account the fact that beam streaks are stretched in one direction. By stretching the filtering function in Fourier space in accordance with the streak orientation is is possible to selectively reduce the appearance of the streaks. Figure 7 shows the original and filtered images of the phantom sample containing the simulated crack. It must be noted that it was not always possible to completely eliminate beam streaks without sacrificing useful data.

3.5 Crack position and opening analysis for absorption microtomography

Data from the absorption microtomography experiments is in the form of a regular, 3D grid representing positions in space, with its elements equal to the values of attenuation coefficients of the sample at these positions. Since the attenuation coefficients of the crack equals that of air, and the attenuation coefficient of the rest of the sample equals that of aluminum, theoretically it should be possible to precisely detect positions and borders of the crack in space, given a sufficient number of measurements. In reality, however, there are limitations on the accuracy of the data imposed by various factors. First, the maximum spatial resolution achievable is limited by the number and size of detector elements. Also, a non-linear response of the individual detector elements may introduce reconstruction artifacts in the resulting image, such as ring artifacts; they are largely absent when the time-delay integration apparatus is used [41]. The continuous energy spectrum of the X-rays in this experiment can also potentially degrade the quality of the image because of the beam-hardening effect [35]. Use of the monochromatic synchrotron X-radiation can eliminate this effect.

The first step in analyzing the absorption microtomography data was the determination of the 3D crack positions. The crack was located using the difference between the linear attenuation coefficients of the crack itself, which was assumed to be that of the air, and those of the aluminum matrix. Due to the noise present in the reconstructed data, simple selection of the crack position as the voxel with lowest attenuation coefficient each in column (along L) of the cut did not work well (this observation is similar to that made by Guvenilir [75]). Instead, a crack detection algorithm was applied.

The algorithm for crack detection relied on the distinctive properties of the cracks; namely their continuity and 1D character (in individual numerical cuts through the 3D reconstructed data) that distinguished it from random noise within the reconstructed

volume, which was of "salt and pepper" (or 0D) type. The crack positions were measured for the loaded sample: this was where crack was most visible. This geometry did not change (at least on the scale of the voxels in the reconstruction) at the different loads. A linear probe with 6 voxel length served as an idealized crack segment. The probe was applied virtually, using computer software, to each reconstructed cut. The cut was oriented perpendicular to the crack growth direction. The probe automatically adjusted itself so that it occupied a set of contiguous voxels with the smallest possible values of linear attenuation coefficient, that is, voxels corresponding to the crack. By moving the probe voxel by voxel along the line of the crack, until the other side of the sample was reached (each cut ran from sample face to sample face), the crack positions for each cut were determined. The procedure was repeated for each cut in which the crack was visible.

Once the crack positions were determined, the opening at each point of the surface was measured. A large percentage of the crack voxels were partial voxels, that is, the voxels contained some aluminum in addition to empty space (or air). This dictated the strategy used to measure crack opening at each position, namely the partial volumes for each crack position along the load axis direction were added to give the total opening at that position. The average value of voxels outside of the volume occupied by the sample was taken as μ of the air. The distribution of μ was measured in part of the sample that did not contain the crack, and μ_{mean} was calculated. Because of the non-monochromatic beam and the resulting beam hardening effect, position-dependent basis in values of the mean linear attenuation coefficient μ_{mean} exist in the reconstruction. Therefore, μ_{mean} is position dependent, which can introduce errors into the determination of crack opening. Instead of using one value for μ_{mean}, individual $\mu_{\text{mean,z}}$ were calculated for each z, i.e. for each column (along L) in each Y-Z cut (note the different font used for the sample coordinate system, which refers to the coordinate system native to the microtomography reconstructed

data; this distinguishes it from the sample coordinate systems used in the rest of the thesis). The opening at each crack position was calculated using $\mu_{\mathrm{mean,z}}$ for that z.

The values of μ around the crack's center were interrogated (along the loading direction) until a value $\mu > \mu_{\mathrm{mean}}$ was found on either side of the crack. The voxels between these two points were converted to partial volumes of crack, f, via

$$f = \frac{\mu_{\mathrm{mean}} - \mu_{\mathrm{i}}}{\mu_{\mathrm{mean}} - \mu_{\mathrm{air}}} \tag{17}$$

and the partial volumes were added to give the total opening at the position in question. Additional details on the method can be found elsewhere [9, 16, 75].

3.6 Stereometry

As described in the Background, analytical geometry equations can be used for reconstructing 3D information about the object for which projection images have been recorded. In this section, computational basis behind stereometry in relation to X-ray phase contrast radiography of fatigue crack sample will be discussed.

While positions of a feature on two projections is the minimum information required for 3D determination of the feature's position (if the rotation axis is known), a more robust determination results if more projections are used in the analysis. Therefore, the projected coordinates of each specific feature were measured for up to 10 sample orientations with the specific number depending on the visibility of the feature. This had the double effect of reducing random error in the measurement of projected coordinates and decreasing the chance that an incorrect feature would be selected in one of the projections.

Figure 8 schematically indicates how projected coordinates of the feature change with sample rotation. The detector and sample coordinate systems are given by $X'Y'$ and XYZ, respectively. Note that axis X is perpendicular to the plane of the drawing, and, for C (rotation axis) perpendicular to the plane of the drawing, the X coordinate x of A (and, therefore, the X' coordinate x' on the detector) does not

change. The position of each feature A that produces phase contrast is defined by vector R (from the rotation axis C to A) and by the angle θ_0 that R makes with the detector plane. After rotation from θ_0 to $\theta_0 + \theta_n$, the coordinates of the image of A on the detector change from x', y'_0 to x', y'_n. For each sample rotation,

$$R = \frac{[C'A'_n]}{\cos(\theta_0 + \theta_n)} \tag{18}$$

where $[C'A'_n]$ is the measured length of the projection of R, and θ_0, the initial angle of R relative to the detector plane, is unknown. Each projection n will produce a different measured $[C'A'_n]$, and the problem is determining the best value of θ_0, and hence z_0, for feature A. Here, the best value of θ_0 is taken to be that which produces the smallest σ_R, the standard deviation of R, for the measured projections. This is done iteratively by substituting a given value of θ_0 and determining R_n for the set of experimental projections, until σ_R is minimized for feature A. This value of θ_0 gives, in turn, coordinate z_0 for feature A.

CHAPTER IV

RESULTS AND DISCUSSION

4.1 Absorption Microtomography

4.1.1 CT-32M data collection

The fatigue crack in sample CT-32M was grown with $R = 0.1$ using an MTS servo-hydraulic fatigue testing machine in the MPRL, and the final crack length was 6.17 mm after 584K cycles. Two sets of microtomography data were taken for sample CT-32M. After the first set of data was taken, 155K additional cycles were applied to the sample, extending the crack an additional 0.4 mm (crack growth was monitored using an optical microscope). During each round of tomography measurements the sample was held under the constant load (in a small purpose-built load frame), as was noted previously [15, 16], and the tomographic data collection was repeated for a number of different loads that corresponded to different portions of the fatigue cycle. Details of the apparatus were described above. In all, 6 measurements were taken for each data set, and data were collected with an X-ray tube voltage of 120 kV. The loads and corresponding stress intensities can be found in Table 3. The stress intensities given in the table were calculated from ASTM 647-93 for the compact tension geometry using:

$$K = \frac{P\,(2+\alpha)\,(0.886 + 4.64\alpha - 13.32\alpha^2 + 14.72\alpha^3 - 5.6\alpha^4)}{B\,W^{.5}\,(1-\alpha)^{1.5}} \tag{19}$$

where K is the stress intensity, P is the applied load, B is the sample thickness, W is the specimen width from the load line to the back face, and a is the crack length a divided by W. Use of this equation is an approximation because sample dimensions varied from the ASTM standard, but accuracy should be adequate because of the small crack extension (relative to the total crack length), and the equation is used for

Table 3: List of the applied loads P and corresponding stress intensities K used during microtomography measurements of sample CT-32M. Crack length is in mm and is measured from the load line

		Crack	Measurement number						
		length	0	1	2	3	4	5	6
Initial	P (kgf)	11.1	0.0	8.4	22.6	37.1	51.7	60.5	-
	K (MPa$\sqrt{\text{m}}$)		0.0	1.7	4.5	7.4	10.3	12.1	-
Final	P (kgf)	11.5	-	8.0	22.6	37.4	52.5	66.2	83.9
	K (MPa$\sqrt{\text{m}}$)		-	1.7	4.7	7.8	10.9	13.7	17.4

the same sample.

To characterize sample macroscopic response, sample load - deflection curves (Figure 9) were recorded for the sample CT-32M early during cycling and after 584K cycles (i.e. with the crack length used for the first set of microtomography measurements). The initial load–deflection curve was linear, and, as it is similar to what was shown in earlier work [75], it is not reproduced here. After 584K cycles, the curve is bilinear. The slopes for the two linear portions of the curve are separated by a bend which demonstrates "macroscopic" crack closure. The load interpreted as the crack closure load is given by the intersection of slopes at low and high load. In this case it is found to be equal to 110 lbs. or 50 kgf.

4.1.2 Crack detection algorithm

Figure 10 shows typical cuts through sample CT-32M (in the Y-Z plane) on the left and results of the crack determination algorithm with calculated crack positions marked white on the right. By combining the results of the crack detection algorithm for each cut, the crack surface position was determined in 3D. Since the relative positions of the crack surface did not change with load (at least on the scale of the voxel

size in the reconstruction), the crack surface at the highest load was determined and was used for 3D representations of distribution of openings at other loads. Determining crack position at the highest load provided the most accurate data, because the crack contrast was most definitive when the crack was open.

Not surprisingly, the sample position in space changed slightly with applied load, and the sample probe starting positions used for a given cut at a given load could not be transferred directly from a previous measurement: corrections for this change in position had to be applied. A 3D correlation translational matrix with a spacing of one voxel was calculated for a number of cuts, and the position of the matrix minimum identified the shift in absolute position of the sample from measurement to measurement. In general it was found that the largest sample shift was in the loading (Y) direction due to the fact that one half of the sample was fixed to the apparatus while the other half moved with the moving loading pin. Sample rotation could not be detected in the cuts. After making geometrical corrections, the crack surface at highest load was used with measurements at other loads.

4.1.3 Crack opening

Figures 11 – 14 show 3D renderings of crack opening superimposed on the crack surface. Since it is impossible to show the whole crack surface in 3D in one view due to the presence of asperities, two views from different observer perspectives are shown to give a better representation of the opening for each load. Each page of a figure consists of three images of the crack surface at the same orientation. Figure 11 shows openings for all loads at the first perspective of the initial crack, and Figure 12 shows the second perspective. Similarly one perspective of crack opening maps appears in Figure 13 for the final crack length, and Figure 14 shows all loads at the second perspective. False color is used to show the amount of opening with the color table going from the dark blue (0 μm opening, crack closed) to the red (80 μm or higher,

largest openings). The color table was kept consistent for all figures to make direct comparisons between different data sets possible. It should be noted here that the largest opening value was higher than 80 μm, but the upper value of 80 μm was chosen for better visualization of the data. The notch side on all figures is marked "N", and the arrows show the direction of the crack propagation.

Images of the initial crack surface contain a strip of gold opposite the notch. This area represents the crack surface which was obtained from the later, extended crack surface and for which no opening data existed for the initial crack surface, because either the crack did not exist at these locations yet, or its opening was too small and below the sensitivity limit of absorption microtomography. It is once again important to note that the actual initial crack length determined by the optical microscopy (6.17 mm from the notch at the sample surfaces, see Figure 15) was larger than the one determined with absorption microtomography (4.83 mm at the largest load), because the crack opening at the crack tip was below the absorption microtomography sensitivity limit. Similarly, the final crack length visible with absorption microtomography was 6.32 mm, and this means that about 10% of the gold-colored surface area closest to the crack tip had not yet formed at the time when the first set of data was taken, but the rest of the gold area (90%) had already been formed but could not be detected with microtomography. About 80% of the crack length could be reliably detected with microtomography for the first data set. For the extended crack, surface position measurements showed the crack grew about 0.4 mm from its initial length (to a total length of $\sim$6.6 mm from the notch). After crack extension, about 95% of the crack can be detected with absorption microtomography, and the reason for this much greater increase in fracture visible is discussed before individual features on the sample are analyzed.

During the 155K cycles of crack extension after the first microtomography measurements, the crack branched (at one face of the sample, Figure 16). The crack grew

first along the first branch and stopped. When the first branch stopped, the second branch started to grow. The overall rate of crack extension slowed considerably from what was expected. One interpretation is that all of the available energy for each extension was being channeled into forming the different branches and perhaps into deforming the volume of material around the two or more active crack tips. Such deformation concentrated over many cycles at a crack tip (constrained from moving by some barrier) might lead to large displacement across the crack surface near the tip, i.e. very large amount of opening in the immediate vicinity of the crack local tip as in blunting-resharpening propagation mechanism [76]. This increase in opening would also appear over the remainder of the crack surface.

4.1.4 Crack surface geometry

The crack surface geometry is similar to that observed previously in other Al-Li 2090 fatigue samples [6, 8–10, 12–16, 42, 43]. There are a number of sharp asperities present, which extend in the crack propagation direction (sample T direction) and have pronounced mixed mode I-III faces (such as "A" and "D" shown on Figure 13). The approximate length of these asperities along the crack propagation direction approaches 1 mm, and the asperities are all parallel. The average asperity height is about 400 μm, so their surface area can be estimated to be on the order of 0.8 mm^2. There are also several rather flat areas free of asperities, such as "B", but their number and area is limited. Finally, some mixed mode I-II surfaces could be spotted on the crack surface, such as "C" shown on Figure 14f.

Figure 15 shows the crack path on the two faces of sample CT-32M, with the crack tip position labeled in K cycles and the local crack growth rate indicated schematically with color fill for each portion of the crack. Local crack growth rates (at least at the surfaces) are somewhat irregular. Figure 17a shows crack length as a function of number of cycles, and Figure 17b shows crack growth rate as a function of stress

intensity factor range.

Figure 11 shows a dip in the crack surface R-R' some distance from the crack tip. This dip is visible in surface micrographs and was formed between 120K and 280K cycles. Figure 13c shows there is somewhat higher opening on the trailing edge; this difference in opening disappears at higher loads. The difference in opening on the two sides of the dip is only appreciable at the highest load (Figure 11f) for the initial crack length.

There is a particularly abrupt change of crack plane on the back, trailing edge of the dip (as shown in Figure 11 and 13). At this point crack remains closed up to the highest loads both before and after crack extension.

Figure 13a-c and e shows a pocket P of opening near the dip R-R' (marked in Figure 13f). This pocket is less visible in Figure 13d, evidently an artifact of the color table chosen, and in Figure 13f the pocket merged with a nearby large open area. The pocket P does not appear in Figure 13, that is, at the initial crack length.

The dip R–R' (see Figure 11c and Figure 15) is about 1 mm wide along the direction of crack propagation (T). It began to form after about 250K cycles, and the far side of the dip was reached after about 100K cycles later. The rates of crack propagation did not deviate significantly from the average over this portion of the crack, and $10.7 < \Delta K < 11.7$ Mpa$\sqrt{\text{m}}$. If the plastic zone size was about the same size as the characteristic microstructural length, then unusual changes in crack path might result. For this sample along the T–direction, the grain dimension is $\sim 500\mu$m. Plastic zone size in case of plane stress can be calculated from [77]:

$$r_p = \frac{1}{\pi}\left(\frac{K_{max}}{\sigma_y}\right)^2, \tag{20}$$

where K_{max} is the maximum stress intensity factor applied and σ_y is the yield stress. For the start of the dip, the crack length was $\sim$ 3.1 mm and $K_{max} =$ 10.7 MPa$\sqrt{\text{m}}$. The yield stress is about 550 MPa [2], and $r_p \sim 0.2$ mm (and the

size of a cyclic plastic zone is smaller than that). It is unlikely, therefore, that plastic zone effects produced the dip. Instead, as is discussed in Section 4.3.1 below, the dip likely is produced by mesotexture variation in the sample.

The images in Figure 18, 19 show the opening projected on the nominal crack plane (i.e., the plane perpendicular to the loading direction). Visible anisotropy of crack opening is present across the thickness of the sample (i.e. along the sample S direction). Many patches of open crack elongated along the direction of the crack propagation (T) are prominent and coincide with the location of sides of the asperities on the crack surfaces, e.g. "A", "D" and "E" in Figure 13) . Another feature that can be seen in all data sets is that one side of the sample is more open than the other. Non-uniform loading probably caused the asymmetry in crack opening. The fact that such non-uniformity can be seen at all loads supports this interpretation.

Measurements number 4 on sample CT-32M were carried out under similar loads for initial and final crack lengths (51.7 and 52.5 kgf, respectively), but the stress intensities differed slightly (10.3 vs. 10.9 MPa$\sqrt{\text{m}}$, respectively) and Figure 20a and b compares maps of projected opening for these two measurements side by side. The color table range is different from the previous figures with maximum opening (red) equal to 50 μm. The amount of opening is different for these two cases, although the general pattern is similar. The top image (initial crack length) has much more pronounced opening at asperity positions. Strongly elongated stretches of open crack were present in the projection for the final crack length image while the projection for the initial crack length appeared more smoothly ranging.

The difference between the two data sets (with the initial and final crack) is shown in Figure 20c. Colors represent the difference in the crack opening at each position on the crack surface with blue representing no difference between the data sets and red the maximum difference (30 μm or more). As it was discussed above, the biggest differences between two data sets can be seen in the areas of asperities (e.g.

"A") where the difference in openings can reach 30 μm and more, and it is mainly concentrated in the central part of the sample. In other parts of the crack surface the difference is much smaller and for the most part does not exceed 10 μm. The main source of the difference in patterns of opening shown in Figure 20c probably is not the slight difference in stress intensities at which the data were collected: 10.3 MPa$\sqrt{\text{m}}$ (initial) and 10.9 MPa$\sqrt{\text{m}}$ (final). From looking at the final crack opening in measurements 3 and 4 (7.4 and 10.3 MPa$\sqrt{\text{m}}$, respectively) in Figure 14 and Figure 12 it can be seen that the general pattern of crack opening remains the same, although the absolute values of opening are different. Since the opening pattern remains similar for relatively large changes in the value of K (for example between Figure 13d and 13e), it can be said that the small difference in K for measurement 4 of the crack before and after extension does not invalidate the comparison.

4.1.5 Asperity on the crack surface

Since asperities play an important role in the process of roughness-induced fatigue crack closure, it is interesting to take a closer look at the opening at asperity faces. Figure 21 shows one of the major asperities on the crack surface (marked "A" in Figure 14f) that is located about 2 mm from the notch and about 0.9 mm in from the face of the sample. In order to view both faces of the same asperity, two perspectives are shown (the asperity in the left column is rotated 90° about the vertical axis L from that in the right column) for the highest three loads (with the highest load at the top of the figure). The cut-off edge of the asperity in the left column is much higher than that on the right because of the adjacent asperity (marked "H" in Figure 14f) that runs parallel to the asperity "A"; the valley between asperities "A" and "H" is considerably higher than the one on the other side of "A".

There is a marked difference in the opening for both sides of the asperity. The letters "I", "J" and "M" mark positions on one face of asperity A; and "I′", "J′"

and "M′" identify the corresponding positions on the other face of this asperity (i.e., the coordinates of "I" and "I′" differ only in their value along the S axis). For all of these positions, local crack opening is much higher on the "right" side of the asperity (smaller S coordinate) than the one on the "left" side (larger S coordinate), and there is a clear "watershed" running along the crest of the asperity (marked by "W"), which separates both faces.

There are two possible causes for this effect (the difference in opening on either side of the asperity). One possibility is that the crack faces rotate relative to each other with applied load, but the specific pattern of opening (opening at the top and bottom of the asperity is approximately equal) does not support this. Most likely, asperity sliding is occuring - crack faces shift relative to each other with lower face going in the S direction, so there is much more contact on the "left" side of the asperity. This is similar to observations of Guvenilir et al. [9] in a notched tensile sample of AA 2090. Figure 22 is similar to Figure 21 but it shows the asperity "A" for the sample with crack before extension. Note that the color table scale is different in this figure with the maximum opening of only 20 μm versus 50 μm in Figure 21. In this case the opening is more or less even for both asperity faces with no noticeable difference in opening at the marked positions.

4.1.6 Crack opening histograms

Figure 23 shows the histogram of crack opening (after crack extension) for the different applied loads. The horizontal axis represents voxel values (in μm) and the vertical axes shows the number of the surface positions (with each position surface area equal to the voxel dimensions) that have the corresponding opening. Different colors are used for histograms at different loads, and the numbers in the plot legend box correspond to the measurement numbers in Table 3. The general shape of the

histograms is similar for all loads. The main peak is located at zero opening (its maximum for every histogram is off scale), which corresponds to the crack whose opening is below the sensitivity limit. The secondary peak on the right side is bell-shaped, usually with a well-defined maximum. As the load is increased, this peak's shape becomes less and less symmetric: its right shoulder extends to higher openings but the position of its maximum does not change appreciably.

Crack opening histograms for the sample before the crack was extended are shown on Figure 24. The general shape of the histograms is similar to those for the sample after the crack was extended. The main difference from the previous figure is the smaller number of pixels with large openings. Also, the maximum of the secondary peak can not be separated from the main peak (zero opening) for loads smaller than 37 kgf.

Figure 25 compares histograms for the same load (about 52 kgf, measurements number 4) of the two data sets (before and after crack extension). The shape of the histograms is similar, but for every opening greater than zero, the number of voxels open is higher for the sample with extended crack than the initial crack. The data for the initial crack length show more voxels corresponding to closed crack (near zero opening). In Figure 25 the difference in the number of voxels for each opening is more or less constant. One might restate this as: for each opening at 52 kgf, extension of the crack adds a fixed amount of additional opening, and the overall pattern of opening does not change. This view is consistent with plastic blunting and crack stalling described above.

At lower loads, opening behavior for the sample before and after crack extension changes. Figure 26 compares opening histograms for 37 kgf load before and after crack extension. In this case, the shape of the histograms is different: the number of crack voxels that have local openings below 5 μm actually decreases for the sample when the crack was extended. Apparently, parts of the crack that are closed remain

closed after the crack is extended, so they do not contribute to the opening at higher opening loads.

Figure 27 shows the histogram of the difference in openings for the sample with extended crack vs. the sample with the initial crack length under the 52 kgf load. The major peak of the histogram is located at zero opening, because the histogram maximum for both before and after crack extension are also located at zero. There is a small range of negative values for positions where initial crack openings are higher than final ones, however the number of such positions is insignificant and probably was caused by noise in the data. Otherwise the histogram closely resembles histograms for positions before and after the crack extension for the same load, with position of its maximum close to the position of the maximums of the other two histograms.

One way to quantitatively describe the process of opening is to measure the total opening, i.e. the total volume of the open space between the crack faces and how it depends on the applied load. Figure 28 shows two plots of total open volume of the crack (in 23.23 μm voxels) vs. load for initial (top) and extended (bottom) cracks. The amount of total crack opening should reflect what is measured by an extensometer, with different slopes for low and high loads in the load - displacement curve. For both the initial and final cracks, the intersection of the two linear segments of the curve in Figure 28 (lines through the bottom three points at low, and the top three points at high loads) is about 40 kgf. In general, the plots exhibit an exponential dependence; clearly seen in semi-log plots (Figure 29). The integrated opening (i.e. the volume of open portion of crack) then can be written as a function of load Vol. $= A\exp(B \times \text{load})$. Curiously, parameters B in the exponent for initial and extended crack are close to each other and are equal to 0.03 kgf^{-1} for the initial and 0.02 kgf^{-1} for the extended crack.

Figure 30 shows opening data for a specific position on the crack surface, located about 2.1 mm from the notch on the side of a big asperity and which is marked "A"

in the Figure 13f. Triangles mark opening for the initial crack length, and circles mark opening for the extended crack. Except at K equal to 4.5 MPa$\sqrt{\text{m}}$ where there is little difference, the final crack opening is larger than the initial crack opening as one would expect. The initial crack opening for point A is zero until 7 MPa$\sqrt{\text{m}}$, after which there is a linear increase in opening, but at a slower rate than that that for the final crack.

Feature marked "B" is located on the substantially flatter part of the surface away from the asperities, i.e., a very different type of location than that of "A", and B's position is marked in the Figure 13f. The opening for position B before and after crack extension is shown in Figure 31 with triangles used for the initial crack data set and circles for the final. At this crack surface point no opening could be detected for the sample before crack extension: the crack remained shut at all loads. The load at which the opening would become noticeable was never reached. After extension, crack opening changed with load, and it showed approximately the same behavior as in Figure 30 but with a smaller slope. The maximum opening at this point was just 12 μm which is about one-half of the voxel size, so it is impossible to determine the exact opening behavior due to the opening sensitivity limits. After crack extension, the opening at B at maximum load was about one-fourth that at A (47 μm) for the same load (84 kgf).

4.2 Phase contrast stereometry

The experimental determination of the optimum sample-detector separation is covered first. A phenomenological explanation of crack contrast in the AA2090 samples follows in the second subsection. The third subsection covers the determinations of crack positions.

4.2.1 Experimental determination of optimum sample-detector separation

In order to determine optimum sample-detector separation distance, several micrographs of compact tension sample CT-43 containing fatigue crack were recorded at different sample–detector distances (see Figure 51). The plane of the specimen was perpendicular to the X-ray beam direction. The notch can be seen at the bottom of the radiographs and the crack growth direction is in the vertical direction.

The first image was taken at 10 mm sample-detector distance which corresponds to the absorption dominated regime. It can be seen from the figure that crack is not visible at all. As the sample–detector distance is increased, contrast from the crack features begins to appear with more contribution from phase propagating through space. As the sample-detector distance is increased, the resulting contrast changes from Fresnel diffraction (or edge-enhanced regime) to the Fraunhofer diffraction in which edges inside the sample become blurred. Although this regime is useful for sample phase determination, in this case it is detrimental to the quality of recorded radiographs. For beamline 1-ID, the optimum sample-detector separation distance was determined to be in the range of 30-50 cm, though this value might differ for other beamlines, since it depends on the beam properties.

4.2.2 Crack contrast in the compact tension samples

As is demonstrated below, changes in the crack surface orientation (asperities) that the X-ray beam encounters on its way through the sample, produce contrast on the detector that is placed at certain distances behind the sample. Thus, the contrast that can be seen on the detector, provided all the necessary conditions (beam spatial correlation, sample-detector distance) for its formation are met, is a projection of all the ridges of the crack surface along the beam direction. Another way to explain it is that phase contrast is a projection of all the "folds" on the crack surface.

Figure 32a shows a phase contrast image of the compact tension sample CT-41M.

The dark area on the left side of the radiograph is the notch from which the crack initiated and propagated to the right. The beam direction was perpendicular to the plane of the sample. The crack growth direction is to the right, and the field of view is about 1.7 mm in horizontal direction.

Figure 32b is a schematic of the cracked sample with the left and right sides of the image being the front and back surfaces of the sample and with the crack propagation direction perpendicular to the plane of the section. The position of the crack is highlighted in black line. Folds on the crack surface traversed by the beam form high contrast lines in the phase microradiograph (see below) and the circles show positions where crack orientation changes sharply relative to the direction of the incident beam. X-ray photons traveling along path 3 of Figure 32b do not encounter changes in μ or δ and this contrast is characteristic of the uncracked sample. Along path 1, the total change in μ or δ is different from that along path 3 (this path crosses the crack), but the paths on either side of 1 have the same change in μ or δ as path 1. The contrast produced at 1 is the same as that of its surroundings and the crack will not be visible. The paths to either side of 2 have accumulated different μ and δ in traveling through the sample, and the position on the microradiograph corresponding to path 2 will show high contrast. The origin of this contrast is akin to refraction at sharp edges in geometrical optics of visible light. The microradiograph in Figure 32a is a superposition of the projections of those parts of the crack surface that are oriented favorably for phase contrast formation, such as those marked by circles in Figure 32b.

The fact that the features are linear, or 1D, in the phase microradiographs, tells that the contrast forming positions in the sample are elongated along the crack propagation direction, i.e. the contrast comes from the tips of the asperities on the crack surface, which in Al-Li 2090 are elongated in the crack propagation direction. In order to confirm this, the following experiment was conducted: Phase contrast radiographs

of the compact tension sample CT-33M containing fatigue crack were recorded at the APS while the sample was still intact. After that, the sample was broken in two parts, the volume of material containing several mm of the crack surface near the notch was cut out and microtomography measurement of this volume was carried out using a Scanco MicroCT-40 laboratory microtomography apparatus at the highest possible resolution. This was done for convenience, and the same map could have been produced in a SEM. The resulting 3D reconstruction of this sample had nominal voxel size of 6 μm. The data set was segmented to separate aluminum in the material from the air and the resulting binary volume was rendered using corresponding software.

Figure 35 shows the crack surface of sample CT-33M on the left and the phase contrast microradiograph of the same position and orientation of the sample on the right. The viewing angle was identical for both. Note that the phase microradiograph was recorded while the sample was still intact, and absorption microtomography was done on the broken sample. There is a very good correlation between the phase contrast features and microtomography crack surface rendering, and letters mark some of the features that can be seen on both images. This clearly shows that the contrast that can be seen in phase radiographs comes from the positions where crack sharply change its orientation, such as at asperities on the crack surface.

4.2.3 Determination of 3D crack positions

In order to record phase radiographs of the whole crack (the total crack length exceeded the 1.7 mm field of view of the detector), the sample was translated in the direction perpendicular to the beam and parallel to the crack growth direction. Figure 33 shows the first half of the crack starting from the notch, and Figure 34 shows the second half of the crack. It took six fields of view at different sample T positions, including some overlap between the fields of view, to record the whole crack. The crack images shown in Figure 33 and Figure 34 were stitched together from these six

fields of view. Vertical streaks that can be seen on these figures are beam artifacts and their waviness at certain locations is an artifact of image stitching. Each feature on the radiograph represents position where the crack sharply changes its orientation. The tip of the crack can be seen in Figure 34 and optical microscopy observations of the surface of the crack confirm that; this will be discussed in Section 4.3 below.

In order to reconstruct the 3D positions of crack features, coordinates of several projections recorded at different sample orientations are required as discussed in Section 3.6. Figure 36 shows three phase microradiographs of the same area of the sample (near the notch) with 10° rotation between each image. In Figure 36, the crack growth direction is vertical as is the rotation axis. The horizontal white dashed line identifies positions at constant T (i.e., at constant distance from the notch tip), and the numbers identify three crack features, whose relative positions in the projection change with sample rotation. As the sample is rotated about its T axis (as in Figure 36), the angle between the incoming X-ray beam and the local crack surface geometry changes, altering the contrast; and features often superimpose as rotation changes or go out of the field of view of the detector.

An array of parallel lines which would include a line such as that shown in Figure 36 (perpendicular to the crack growth direction for all rotation angles and at identical separations from the notch tip) was superimposed on each of the phase radiographs. Each clear intersection of the crack image with a reference line was selected and traced through the different projections; its position was recorded where it was not obscured by other features. The process was aided by a software program which clearly marked each processed point on the radiographs so it would not be confused with other, still unprocessed points. First, a coarse array with a line separation of 220 μm was applied, and crack feature positions were measured as a function of angle. After this initial feasibility study, a fine array with line separation of 44 μm was used. The entire crack surface visible in phase microradiographs was covered by an array

of 112 lines and 2269 points. Rows of points equidistant from the edge of the notch resulted (as viewed from above the nominal crack plane), and the points on each line were not evenly spaced. In other words, the process necessarily does not produce an evenly spaced mesh covering the fatigue crack surface, but the density of measured fatigue crack positions was never too low to prevent accurate reconstruction of the 3D surface.

While positions of a feature on two projections is the minimum information required for 3D determination of the feature's position (if the rotation axis is known), a more robust determination results if more projections are used in the analysis. Therefore, the projected coordinates of each specific feature were measured for up to 10 sample orientations with the specific number depending on the visibility of the feature. This had the double effect of reducing random error in the measurement of projected coordinates and decreasing the chance that an incorrect feature would be selected in one of the projections.

Figure 37 shows the variation of σ_R as a function of θ_0 for a typical point on the crack face within the sample. Positions from ten different projections were used (angles between $-8°$ and $-28°$), and the minimum value of σ_R (0.7 pixels) was at $\theta_0 = 6.3°$. For reference, $R = 288$ pixels for this point, and the sample face was perpendicular to the X-ray beam at $0°$. Assuming the σ_R represents the sphere of uncertainty about the point within the sample, the uncertainty in z_0 would equal σ_R, that is, 0.7 voxels or 1.9 μm for 2.7 μm pixels. Suppose one erroneously selected θ_0 for $\sigma_{Rmin} + 5\mu$m; from Figure 37, this corresponds to $\theta_0^L = 5.2°$ or $\theta_0^H = 7.3°$. Via Equation (18), the values of θ_0 correspond to $R^L = 790$ μm and $R^H = 767$ μm and to heights 505 μm and 489 μm, respectively, instead of the height of 497 μm which was actually determined. The actual uncertainty from this source, however, is much less than these calculated values.

4.3 Phase contrast stereometry compared to absorption microtomography

4.3.1 Crack face-maps

For lines T=0.27 mm, T=1.35 mm and T=1.89 mm (T=0 is the notch tip), Figure 38 compares crack surface positions obtained with phase stereometry reconstruction (asterisks) with those obtained with absorption microtomography (solid line, reported previously by Morano *et al.* [15]). In general the agreement between the two methods can be considered to be quite good, and discussion of the differences is postponed until the following section. At all three T positions, the crack face is quite jagged although the nature of the roughness changes. At T=0.27 mm, there is one large mixed mode crack surface (500mm $< Z <$ 1000 mm), i.e., a crack surface deviating from perpendicular to the load axis, but the balance of the section consists of smaller scale peaks and valleys. At the other two positions, the crack surface is dominated by the mixed mode surface extending 500mm $< Z <$ 1500 mm. In addition, at T=0.27 mm the maximum departure of the crack from its mean "height" is ΔL = 300 mm while at T=1.35mm and T=1.89 mm ΔL = 450 mm. A number of phase contrast data points lie outside of the thickness range covered by microtomography data. This is due to the fact that reliable crack positions at the edge of the sample can not be obtained with microtomography because of the partial volume effect.

The difference in crack face positions for two methods (solid line for microtomography and discrete markers for phase contrast) in Figure 38 could result from several factors. The very pessimistic calculation of uncertainty in crack height (in the preceding paragraph) would not be visible in Figure 38: the size of the asterisks is larger than the uncertainty. In absorption microtomography the resulting 3D data is regularly spaced with a fixed voxel size, while in the stereometric approach the 3D data is scattered in space and density of points depends on the density of features (cracks) which can be followed in microradiographs. Sharp crack branches running

along the loading direction (from the main crack) are a common feature of fatigued samples from the center of the same plate as this sample (Haase *et al.* [6, 43]). The presence of such cracks would lead to differences like those that are seen in Figure 38: absorption microtomography of the compact tension samples would not detect such narrow crack branches while the stereometric phase method would be extremely sensitive to some orientations of minor crack branches. In addition, small differences between the datasets can be explained by the averaging effect of large voxels in the absorption microtomography data, that is, positions near sharp asperity ridges may be smoothed out. The data for the two modalities were as closely aligned as possible for the comparison: data from phase contrast stereometry was translated in three dimensions relative to the absorption microtomography data to minimize the difference between them. Differences in Figure 38 could be accentuated by slight angular misregistrations.

Figure 39 compares crack height (L) as a function of position T and S for absorption microtomography and for phase stereometry. The colors represent the different heights (yellow highest, blue lowest) along the L direction, and the notch is to the left of each image and the crack grew to the right. Figure 39a shows the absorption microtomography data, Figure 39b the phase stereometry data. Note that Figure 39a does not show crack positions over the entire thickness of the sample (along S); this is because partial volume effects near the specimen's faces caused difficulties with the software used to extract crack position from the absorption microtomography slices. The lower crack opening sensitivity of absorption microtomography allowed crack positions to be determined to a distance approximately 1 mm from the notch. Phase contrast imaging is much more sensitive to cracks which are nearly closed, and the surface is reconstructed to the crack tip (Figure 39b). It should be noted here that absorption microtomography surface map was reconstructed from data recorded

with a 40 kg load applied to the sample, whereas phase contrast maps were reconstructed with no load applied to the sample. With no load applied during absorption microtomography imaging, even less of the crack can be detected [15].

There are several regions with different character on the crack surface. The bottom part of the crack (as aligned in Figure 39a) is dominated by a rather symmetric large asperity with A marking the highest point on the crack surface. The rest of the surface is rather uniform with the exception of several deep hollows at the left upper part of the surface, separated by ridges such as C or DD'. E marks a position near the crack face where there is a sharp change in the crack surface: the crack rises from E to a large asperity. There is a good agreement in the crack surface positions obtained with the two different methods. The phase contrast map (Figure 39b) provides more detail at the positions where sharp changes in surface height occur, such as the edges of the asperity near B and E. The rest of the crack surface is much flatter with relatively small changes in the surface height. In this region of the crack, several ridges extend from left to right (parallel to the sample faces, i.e. to the sample T direction, the crack propagation direction). These ridges or asperities are relatively sharp and are similar to those described by Haase *et al.* [6] in fractured AA 2090 samples from the same lot of material. Near both faces of the sample, the crack is much flatter.

Contrast at positions where the crack meets the sample face is much lower than at positions within the interior of the sample, and this intersection often could not be observed. The effect was exacerbated toward the tip of the crack, as one would expect from the steadily decreasing crack openings. The unusual shape of the crack surface map (i.e. the trapezoidal boundary) obtained from phase stereometry (Figure 39b) is the product of this surface effect and the decreasing opening as the crack tip is approached: near the notch, nearly the entire thickness of the crack (along S, vertical in the figure) can be measured while the fraction that can be mapped decreases as the crack tip is approached. Physical measurement shows the actual sample thickness

is constant within 10–20 μm from notch tip to backface.

Asperity A shown in Figure 39a is 2.5 mm long in the sample T direction. In this alloy typical grain size is about 2.5 mm in the L direction, 500 μm in the T direction and 50 μm in the S direction. This means that asperity A is approximately five grains long. The top of the asperity at A is relatively flat, as is the area around C. Along T, the flat portion at the top of the asperity A is slightly less than 1 mm long. The flat areas at A and C could mean the absence of near-single crystal volumes. Between E and A and A and D' there is a sharp change in crack height. Along the S direction the change in crack height between A and D' takes place over 0.5 – 1.0 mm. For an average grain dimension of 50 μm along S, the crack height change would occur across 10–20 grains; and this is consistent with the size of near-single crystal volumes mapped previously [6, 43, 78]. Along the crack propagation direction, the rise from E to the plateau at A is more abrupt than the transition in height from A toward the crack tip. The crack rises from E to the plateau at A over a distance along T of about 1 mm, and this is about twice the average grain dimension. In the L direction, the typical change in crack height (that is between A and D') differ by about 2 mm which is close to the typical grain size in L direction. Taken together, these observations suggest that the crack propagates through a near single crystal volume between E and A. The asperity face between D and A would be the result of the crack propagating through a second area of near single crystal material.

The changes in crack path are unlikely to be influenced by the plastic zone size. The monotonic plastic zone size at the crack tip r_p changes in this sample from 110 μm in the area near the notch to about 270 μm at the final crack length. It is smaller than the typical grain dimension in the direction of crack propagation (500 μm).

Figure 40 compares the crack path on two sample faces (front and back): the crack visible in optical micrographs is compared with results of phase contrast stereometry. Because the intersection of the crack with the sample surface does not always provide

high visibility features for stereometric analysis, the stereometry-derived crack positions closest to the surface were used in Figure 40. The semi-circular-appearing notch tip is on the left and crack grew to the right. The length of the crack for both surfaces determined by two methods (optical microscopy and phase stereometry) is identical (6.0 mm for both front and back faces). A very good match exists between the crack's surface positions determined by the two methods. The maximum difference between the two path determinations ΔL was 250 μm.

A small amount of crack branching can be seen in the crack's surface path obtained from optical microscopy. The procedure described above for phase contrast stereometric reconstruction does not always allow detection of multiple crack branches. Since phase contrast imaging is sensitive to the asperities, it is possible to separate branches if their S-T plane projection coordinates coincide. Usually this is not the case. This effect can introduce artifacts in the reconstructed surface by combining surfaces from several branches. In case of the CT-41M sample, absorption microtomography did not reveal branching in the sample interior, only several branches at the surface (similar to those seen in the optical microradiographs) could be seen. Small branches invisible with absorption microtomography with 60 μm voxels could still be present, that is, two branches in adjacent 60 μm voxels might appear as a single wide-open crack.

4.3.2 Crack openings

For measurements under load, a simple four-post load frame was used. Load under displacement control was applied along the sample L direction, and phase microradiographs were recorded for each load ranging from 2 to 40 kgf. After applying a new load, no images were recorded until stress relaxation ceased (as measured in the frame's load cell). Again, overlapping fields of view were recorded to cover the whole area of the crack. The amount of crack opening at a number of specific positions

was measured for each load. Crack opening was taken as a distance between opposite high contrast regions for each crack feature. The reasoning behind this is that the most prominent change in phase contrast formed by each asperity is where the hill on one crack face is pulled away from the matching valley on the other face. As the load increases, the opposite faces separate, and the contrast in the projected image should reflect this separation, which, in fact, is seen in the images.

Contrast of the crack in phase radiographs changes with applied load, and Figure 41 shows change in contrast for sample CT-41M at four different applied loads from 10 kgf to 40 kgf. The area shown is near the notch, and the load was applied in vertical direction. Widening of the crack lines with load can be clearly seen. Figure 42 shows microradiographs recorded at the same loads, but in the area near the crack tip. In this area widening of the crack lines is much smaller, especially at the crack tip. The magnified area from Figure 41a is shown in Figure 43. Radiographs recorded at loads of 2, 20, and 40 kg (Figure 43a, b, and c, respectively) are shown, and in this figure the load was applied in the vertical direction. Contrast is formed for each crack - matrix interface, so there is a set of two parallel contrast lines for each feature in the radiograph. The separation between the pairs of lines of high contrast increases with applied load, reflecting the actual opening of the crack at the specific position.

Crack openings were measured for nine positions on the crack surface. Figure 44b shows the location of these positions on the map of the crack surface. For the most part, these positions are situated near areas with the steepest inclinations of the crack face relative to the nominal crack plane. For each of these positions, crack openings were measured for a number of applied loads from 2kg to 40kg. Figure 44a shows the amount of opening at the nine positions on the crack surface for 40 kg and 20 kg load. Positions on the plot are arranged by their distance from the notch of the crack (that is, ignoring where in the through thickness direction the points lay), and the

most distant position from the notch is at about the midpoint of the crack. Scatter bars on the plot show the pixel size of phase contrast radiographs that were used in reconstruction. In Figure 44a crack opening generally decreases monotonically as one moves away from the notch. The position about 900 μm from the notch is an exception. This position is associated with a point on the crack surface that lies on the edge of the asperity, that is, where the effects from asperity-induced crack closure would be most notable. In going from 40 kg to 20 kg load, the decrease in opening at this position is much less than that at points somewhat closer to the notch. Figure 45a shows crack opening data determined from phase contrast microradiographs for three points on the crack surface located at different distances from the notch. Opening increases with applied load and decreases with distance from the notch.

Figure 45b compares opening vs. applied load determined from absorption microtomography and from phase stereometry: the data are for the same point, the point farthest from the notch, see Figure 44b, upper right corner. This point is near the limit of what can be measured by absorption microtomography, but is $\approx$ 3 mm behind the crack tip position revealed by phase contrast radiography (which is virtually identical to that observed on the crack face by optical microscopy). The scatter bars show the detection limits (1 pixel or 2.7 μm) in the phase microradiographs and one quarter or 14.5 μm in the absorption microtomography data. The data are in good agreement.

4.4 Contrast formation in phase microradiographs. Phantom samples

To better understand the nature of phase contrast formation in samples containing cracks, two phantom aluminum samples[1] were used in portion of the study. They were machined as 3 mm cubes, which is close to the thickness of compact tension specimens.

[1]Samples were provided by Wah-Keat Lee, APS User Division, Argonne National Laboratory

Several cuts were made with spark machining using a thin wire electrode; these cuts in the samples simulated cracks. The geometry of the cuts is schematically shown in Figure 46. Phantom specimen 1 had a saw-shaped cut, and phantom specimen 2 had a cut shaped as arc.

X-ray phase contrast micrographs were taken, and two are shown in Figure 47. For both of the samples, the crack images can be seen clearly in certain orientations. In other orientations (that is with the plane of the crack perpendicular to the beam), the cracks were invisible, which is what one expects from the physical principles of phase image formation. Increasing the separation between the faces of the cut changes the resulting image. Machining marks on the crack surface can also be seen in the images (slight stippling).

4.5 Simulation of phase contrast microradiographs

Using equations from the Section 2.4.1 and information about physical parameters of the sample, such as its linear attenuation coefficient μ and deviation of index of refraction from unity δ, and beam parameters such as X-ray photon energy E, it is possible to calculate the wave intensity distribution after interaction of the X-rays with the sample. Software was written specifically for the purpose of modeling this interaction in order to determine how geometry of the sample influences the resulting 2D image and what is the contribution from absorption and phase contrast components. The incident X-ray wave front was assumed to be planar, which is a good assumption for third generation synchrotron radiation sources, and scattering from the sample was assumed to be absent. Since the thickness of the sample under consideration was much smaller than the sample - detector distances used for calculations, effects due to finite sample thickness were neglected and samples were represented as a 2D objects with their plane perpendicular to the direction of the beam. For each coordinate of this 2D model, μ and δ were calculated by integrating along the beam

direction through the sample thickness.

For modeling purposes, the cracked aluminum specimen can be represented as a composite structure consisting of air (crack) and aluminum with corresponding parameters β (imaginary part of the index of refraction) and δ. For air these parameters were assumed to be those of vacuum. Figure 48 shows change of β and δ with photon energy for aluminum [1]. For 30 keV X-rays, β and δ were equal to 7.6 x 10-10 and 6.0 x 10-7, respectively. As mentioned above, these parameters differ by nearly three orders of magnitude: $\delta/\beta = 7.89 \times 10^2$.

Figure 49 shows the cross-section of the idealized cracked sample that was used as a model for calculations. The thickness of this model sample is 2.7 mm, and it contains a crack with crack opening that was assumed to be 37 μm. Values μ and δ in the sample volume were those of aluminum, and they were set to zero inside the crack (no absorption and phase change). The direction of the X-ray beam is shown with arrows and detector is located on the opposite side of the sample. Since the sample thickness is negligible in comparison with the sample - detector distance, the particular shape of the crack does not affect outcome of the calculations, only the line integral of sample parameters along the beam direction is important. The virtual detector contained 256×256 elements, its dynamic range was 8 bits and its element size was 20 μm. All resulting images were normalized with respect to incoming X-ray intensity.

Four images calculated for the idealized sample at different sample - detector distances of 1 cm, 10 cm, 20 cm, and 30 cm are shown in Figure 50. At the smallest sample - detector distance, that is, where X-ray absorption in the sample dominates the resulting contrast, no crack features can be seen, the change in X-ray path length for the cracked portion of the sample relative to the uncracked sections is below the detection limit. As the sample - detector distance is increased (corresponding to the detector moving into the Fresnel diffraction regime), two contrast lines start to appear

at the positions corresponding to the crack edges. The upper line corresponds to the upper edge of the crack and lower line to a lower edge of the crack. This clearly demonstrates that the crack can be detected in phase contrast regime even when it is too small to be detected with X-ray absorption.

This effect (absorption dominant at small sample-detector separation, phase contrast dominating at higher separations) was confirmed experimentally (for example, see Figure 51).

It is interesting to compare limits of sensitivity for these two regimes. In order to do that, the crack "thickness" in the direction of beam propagation was varied in the software while the thickness of the sample was kept constant. At highest crack "thicknesses", the crack could be easily seen in both absorption and phase contrast regimes. The calculations were repeated for decreasing crack "thicknesses", and the critical crack thicknesses at which it could be barely seen were recorded for both regimes. The result showed that in fact, at least theoretically, phase contrast sensitivity to crack is about three orders of magnitude higher than that for absorption, which corresponds to the difference in magnitude between β and δ.

Another interesting question is the dependence of the shape of the crack on the phase contrast. Since for thin samples phase contrast depends on the projection of δ in the sample along the beam direction, then it follows that the specific local shape of the crack should not play a large role in contrast formation. Experimental measurements performed on two phantom samples (Figure 46) showed that this is the case: contrast resulted for both semicircular cracks (data not shown) and cracks bending 90° (for the X-ray beam going from left to right in the plane of the figure).

Another question of interest is how the orientation of the crack in space changes the resulting contrast. Figure 52 shows two orientations of the same crack relative to the X-ray beam. In orientation (a) of the incident beam there is phase contrast from the crack as shown on Figure 50d. However there is no contrast in orientation

(b) due to the fact that all X-ray beam photons that traverse the sample contain the same total change in their phase and attenuation after exiting the sample, and, as a result, do not form contrast on the detector. Numerical modeling and experimental measurements on the phantom samples confirm this reasoning.

Figure 53 shows radiographs recorded at several orientations of cracked sample CT-11 at a sample-detector separation of 915 mm. As described previously, the compact tension geometry is far from ideal for absorption microtomography in terms of sensitivity to cracks. In order to get high spatial resolution, high contrast sensitivity data, a small volume near the notch of the crack was cut from compact tension sample CT-11 with its longest dimension oriented in the crack growth direction and cross-section of 2.7×4 mm. The cut-out volume was from a portion of the sample near the notch and consisted of two halves held together with clear office tape (with the matching crack surfaces fitting together). The tape can be clearly seen on the reconstructed slices (Figure 54b) despite its low absorptivity. Horizontal streaks in the radiographs are the result of beam non-uniformity and do not result from the interaction of the beam with the sample. Figure 53a corresponds to the orientation of the nominal crack plane parallel to the plane of the detector. The vertical edges of the sample can be clearly seen, however no contrast from the crack surface can be resolved. Figure 53b corresponds to the angle of 22.5° between the nominal crack plane and the detector, and the contrast from the crack is much more pronounced at this orientation.

This example demonstrates the large change in crack contrast with changing sample orientation. It also demonstrates why algorithms different from absorption microtomography are needed for CT reconstruction based on phase contrast projections. Absorption CT is based on the contrast formed by line integrals of linear attenuation coefficients in the sample at different sample rotations; linear attenuation coefficients

are constant for every elementary volume in the sample and do not change with rotation. However, in the case of phase imaging, contrast from each feature depends on the sample rotation angle, at some rotations it disappears or is greatly diminished, that is, there is no contribution from this feature in the specific projections, as if it did not exist in the sample. Thus, application of absorption CT reconstruction methods to projections containing phase contrast component may lead to significant errors and artifacts. There are a number of reconstruction algorithms being developed for phase contrast tomography, for example [79], however practical implementation of these algorithms is still fraught with difficulties.

Figure 54 is an example of differences in reconstruction of phase and absorption objects. Radiographs of sample CT11 were recorded in the range of $0^\circ - 180^\circ$ sample angular orientations at a number of sample - detector distances at APS and reconstructed using a filtered backprojection algorithm [80]. One reconstructed slice is shown for sample - detector distances of 50 mm (Figure 54a) and 915 mm (Figure 54b). The microradiograph at the larger sample-detector separation exhibits much larger phase contrast contributions than the 50 mm radiograph, which is mostly formed by X-ray absorption. Contrast between the sample and air is much higher in the top image of Figure 54 (dissimilar μ), whereas contrast from the edges of the crack is higher in the bottom image (sharp changes in δ), especially at locations where the crack changes direction (emphasized with arrows in Figure 54b. This confirms that phase contrast in the cracked samples originates mostly from areas in the sample where crack changes direction.

Going back to the discussion of tomography reconstruction for the case of phase contrast, star-like artifacts can be noticed in the bottom slice of Figure 54. These originate from the positions of high phase contrast, and small area of the slice containing them is shown magnified in Figure 55. Similar artifacts are well-known in

absorption tomography and they result in part from the insufficient number of angular radiographs [35], which is equivalent to the statement above that phase contrast can be lost at certain sample orientations.

X-ray photon energy is another parameter that should be carefully considered. Synchrotrons allow easy selection of the required monochromatic energy within a range of several tens of keV by adjusting gaps in the insertion device and tuning additional monochromators further down the beam line. The result is the X-ray beam within a very narrow selective energy range. For absorption radiography, the best contrast is obtained when $\mu t \sim 1 — 2$, where μ is the linear attenuation coefficient of the sample material, which varies with beam energy, and t is the sample thickness.

In the case of phase contrast radiography, there are two contributions to consider. In addition to the dependence of phase contrast itself on X-ray energy, there is an energy range limitation due to X-ray attenuation in the sample. If the energy is too low, then the sample may be too absorbing for X-ray transmission and there would be no useful signal on the detector, even if the energy satisfies requirements for phase contrast.

In addition to detecting crack position in the projections, phase contrast images can also reflect changes in the local crack opening with load, which can be measured. The reasoning behind this statement is that the most prominent change in phase contrast formed by each asperity is where the peak on one crack face is pulled away from the matching valley bottom on the other face. As the load increases, the opposite faces separate, and the contrast in the projected image should reflect this separation, which, in fact, is seen in the images.

An important test of phase contrast modeling is calculation of image contrast based on a physical model of an actual sample and comparison of it with a radiograph of the same sample. The following calculations were performed using data

from the section cut from sample CT-11. In order to get a model for simulation, absorption microtomography was employed. The microtomography measurement was conducted at a sample - detector distance of 50 mm to minimize phase effects. The 3D volume of the sample was reconstructed and segmented with a threshold value in order to separate volume occupied by material from that of air (Figure 57a shows one segmented slice). Values for μ and δ for aluminum were assigned to the volume occupied by each material. The simulation was performed with the same experimental parameters, such as X-ray energy and sample-detector distance, that were employed in data collection.

Figure 56 for 50 mm sample-detector separation compares results of the simulation (Figure 56a) with an experimental microradiograph of the sample (Figure 56b). The sample faces were at 45° to the beam (for reference, a schematic of the sample cross-section and its orientation relative to the beam is shown in the lower right part of the Figure 56b). There is a good match between the two images. The simulated radiograph looks cleaner than the experimental one because the negative effect of beam fluctuations was partially removed during segmentation of the microtomography-derived volume. The vertical edges marked A on the microradiograph (Figure 56) correspond to the two opposite corners of the sample (also marked on the schematic), and the dark area between them is due to constant absorption between the projections of those two corners (in this area the path traversed by X-rays is constant). The two thin white horizontal lines on the simulated radiograph are the result of a glitch during reconstruction - no data existed at these positions.

The simulation worked well at small sample - detector distances (up to 30 cm), however artifacts and noise in the reconstructed model data negatively affected simulation results at higher sample - detector separations. This results from the fact that phase contrast is very sensitive to sharp gradients in data and noise which was not removed during segmentation stage. This noise has very high frequency components

and is accentuated in the calculation.

In order to get simulation results at higher distances, one reconstructed data slice was selected from sample CT-11, segmented, and the noise was manually removed (Figure 57a). Figure 57 compares calculated contrast for a sample - detector distance of 405 mm (Figure 57b) with experimental X-ray intensity profile recorded at the same distance (Figure 57c). Arrows in Figure 57a show the direction of the X-rays used in the calculation and in the experimental microradiograph. Three peaks marked A, B and C and separated by valleys can be seen on Figure 57b and Figure 57c. The general character of these features is reproduced, but some details are not. Low-frequency variations present in the experimental profile are most likely the result of incoming beam intensity distribution variation. Aliasing effects contributed to the high-frequency noise in the calculated profile (since the model's surface was oriented at an angle to the incoming beam, there was a slight jump in the values of μ and δ for adjacent beam paths). For small sample - detector separation distances (absorption contrast regime) noise in the theoretical profile disappears.

CHAPTER V

CONCLUSION AND RECOMMENDATIONS

In this work, two innovations were demonstrated for in-situ 3D study of fatigue cracks and their closure as a function of applied load; these represent the culmination of over ten years' research on fatigue crack closure in aluminum samples. Earlier work had limited sensitivity to small crack openings so learning how to measure openings closer to the crack tip was a major challenge. Taking samples fatigued earlier as part of the larger program, absorption microtomography and phase contrast stereometry reconstruction determined 3D crack positions and openings as a function of applied load. At the time the microtomography data were collected, there was no such instrument at Georgia Tech, and the approach followed by Guvenilir [9, 10, 12] and Morano [15, 16] in earlier thesis work was used: data collection was done in collaboration with others possessing such a system (Prs. Elliott and Davis, Queen Mary, University of London). The phase imaging was done by the author, his advisor and their collaborators at APS. In both cases, the analysis and interpretation of the 3D data was the challenge addressed by the author.

First, crack openings as a function of applied load and 3D position were determined for the first time in a cracked specimen before and after crack extension using X-ray absorption microtomography. Second, a new technique for high spatial resolution, high sensitivity 3D reconstruction of plate-like samples was developed and applied to a cracked compact tension sample. This technique, phase contrast stereometry, avoided the limitations of the computed tomography algorithm for plate-like samples. X-ray phase contrast imaging was demonstrated to be much more sensitive to cracks with small openings and phase microradiographs of the cracked aluminum sample

were recorded at between 5-10 different orientations of the sample with respect to the incident beam. The stereometry approach allowed 3D reconstruction of the crack position, and crack openings were quantified from the phase microradiographs.

In general, there was good agreement between the results of absorption microtomography and of phase stereometry on the same sample. The increased sensitivity of phase imaging to cracks, compared to that of the absorption X-ray methods, allowed detection of the crack up to its tip with no load applied to the sample. The length of the crack determined by phase stereometry matched that determined by optical microscopy in terms of minimum resolution achievable for fatigue cracks. The advantage of the phase method is that it also provides information about interfaces where refraction index changes within opaque materials.

The opposite crack faces were visible at the peak of asperities (and the corresponding valley) in the phase microradiographs. At positions where both absorption microtomography and phase stereometry data were available, the displacement of these images was measured as a function of applied load and was shown to match that measured with absorption microtomography. The data suggest that use of phase contrast images for opening quantification is considerably more sensitive than absorption microtomography. The phase approach, however, suffers from the limitation that it does not allow determination of opening at arbitrary positions on the crack surface.

Computer simulation of the X-ray interaction with a cracked aluminum sample was carried out, based on the physical processes behind phase contrast formation and taking into account experimental parameters such as the X-ray wavelength, the material's index of refraction and sample - detector distance; and its output was compared with experimental results. The simulation confirmed that the linear, high contrast "strands" observed in the phase contrast microradiographs were from the tips of asperities or from other sharp changes in crack path. A small model sample (with a

square cross-section ideal for absorption microtomography and containing a wide open crack) was reconstructed with absorption microtomography (small sample–detector separation). Results of phase imaging of the same sample (larger sample–detector separation) were compared with the simulation based on the absorption-reconstructed cross-section, and the two were found to be in qualitative agreement.

This study demonstrated that it is possible to reconstruct accurate 3D positions of features inside optically opaque sample by recording several X-ray projections; however for larger sample volumes or for higher resolution data sampling, the approach used in this study (manual selection of the features and successive computer processing to yield 3D coordinates) may be impractical. By using cross-correlation between pair of images it might be possible to completely automate the process, without the need for human intervention which would significantly speed up the process of 3D reconstruction.

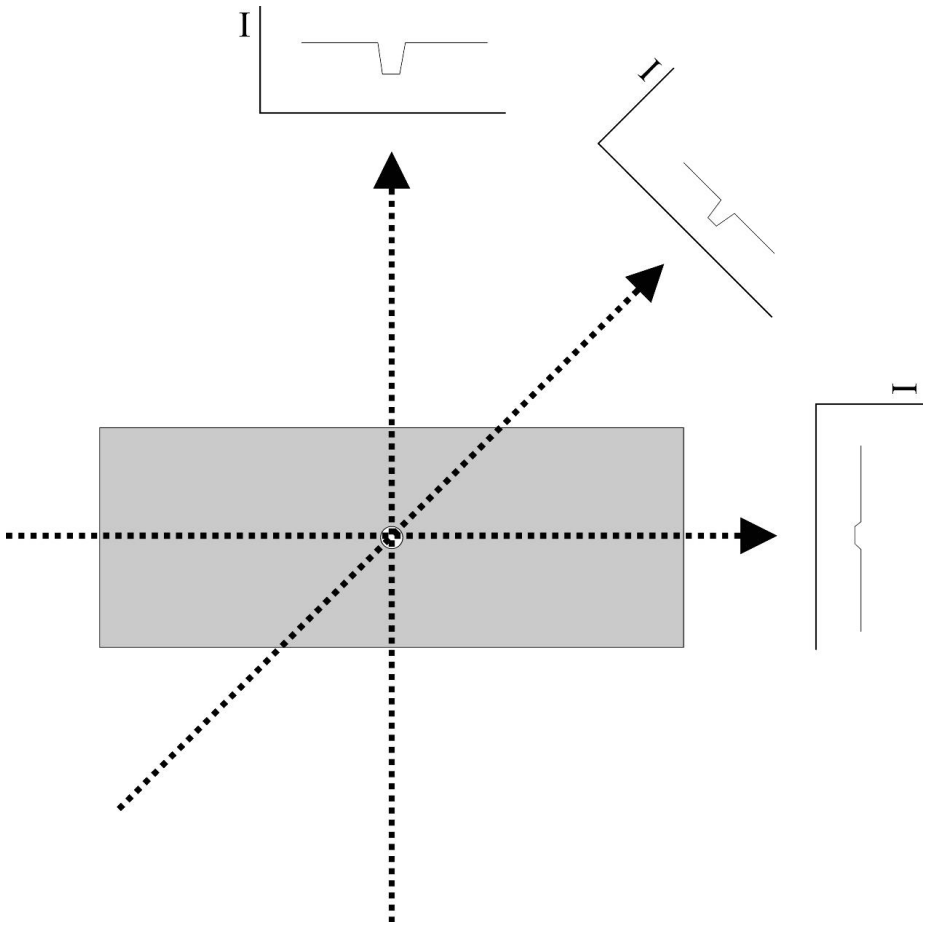

Figure 1: Illustration of the dependence of tomography sensitivity to cracks on specimen geometry. The arrows represent X-ray beam and the plots schematically show intensity of transmitted X-rays.

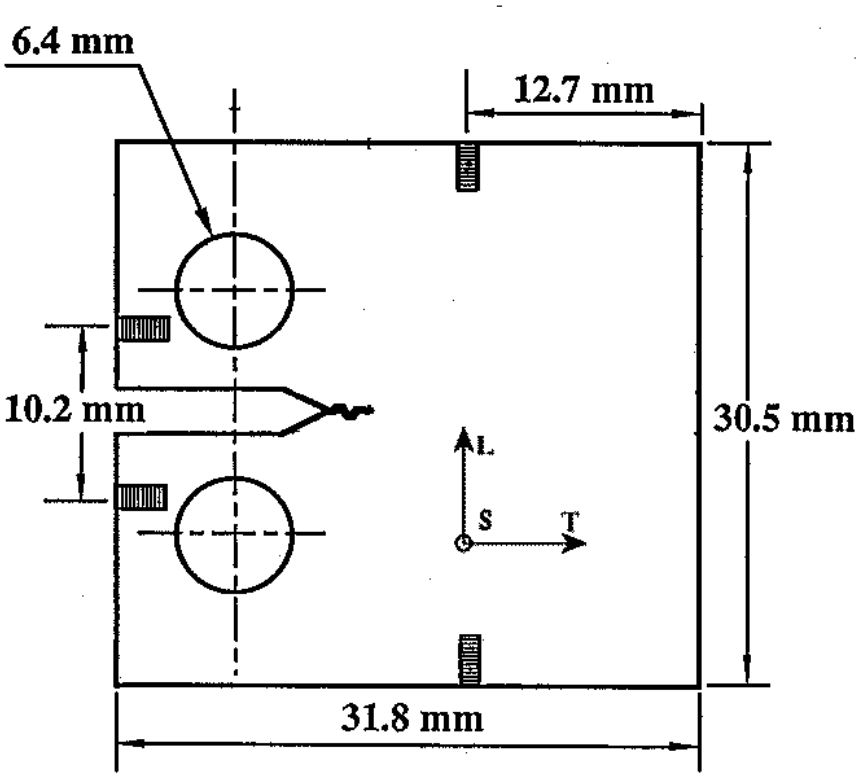

Figure 2: Schematic of the compact tension sample geometry. L corresponds to the plate rolling direction, T – to the plate transverse direction and S – to the plate short transverse direction. Thickness of the sample is 2.7 mm.

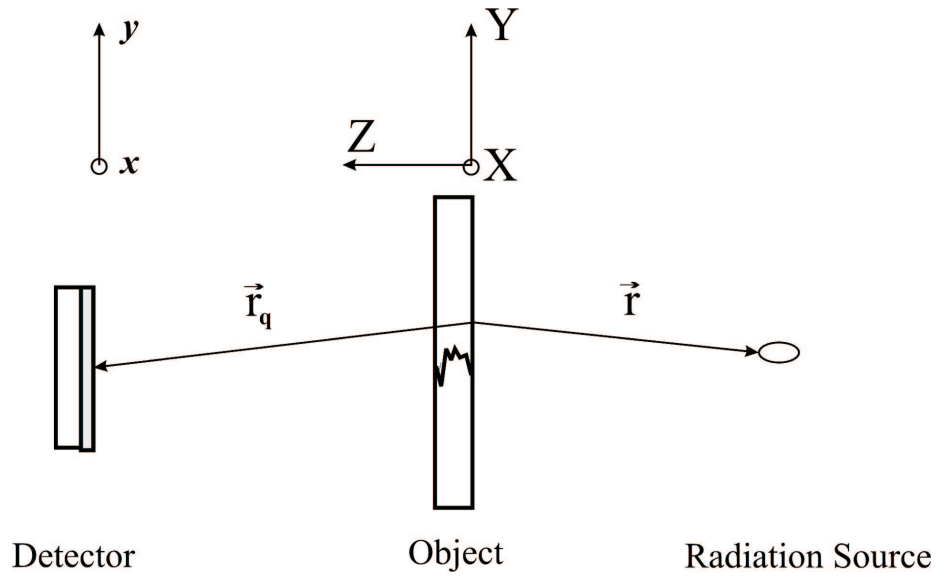

Figure 3: Schematic of the Kirchoff formulation. (XYZ) is the object coordinate system, (xy) is the detector coordinate system.

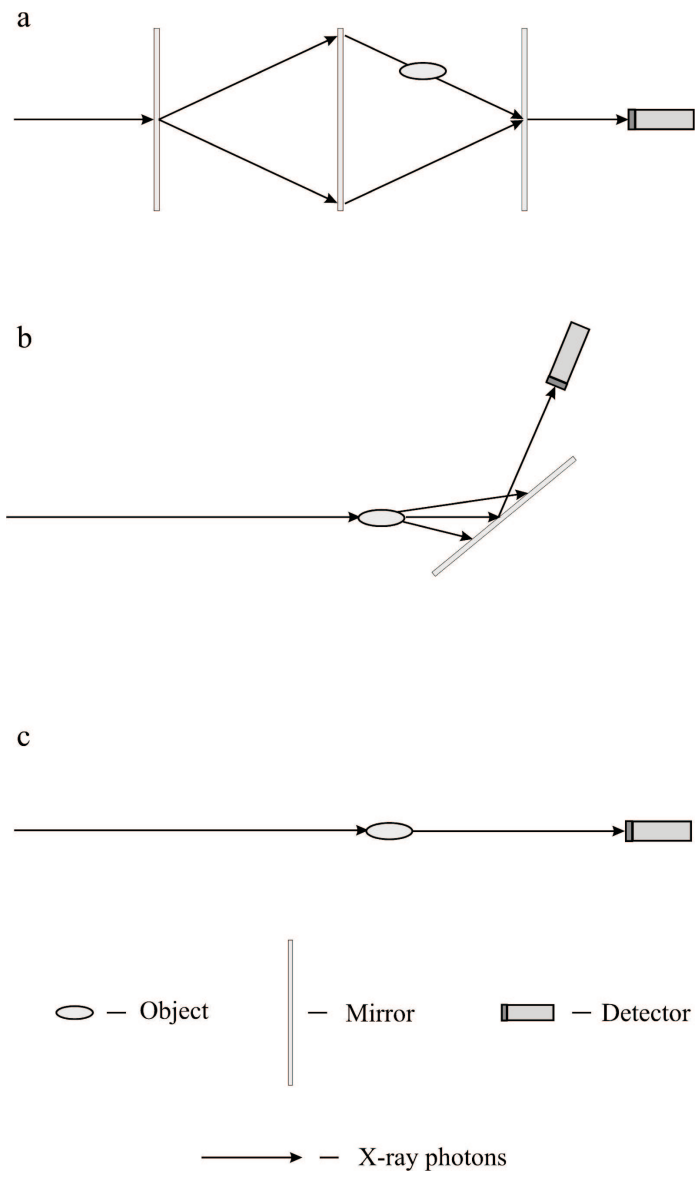

Figure 4: Schematics of several phase-contrast imaging methods: (a) interferometer method; (b) diffraction-enhanced phase contrast method; (c) propagation phase contrast method

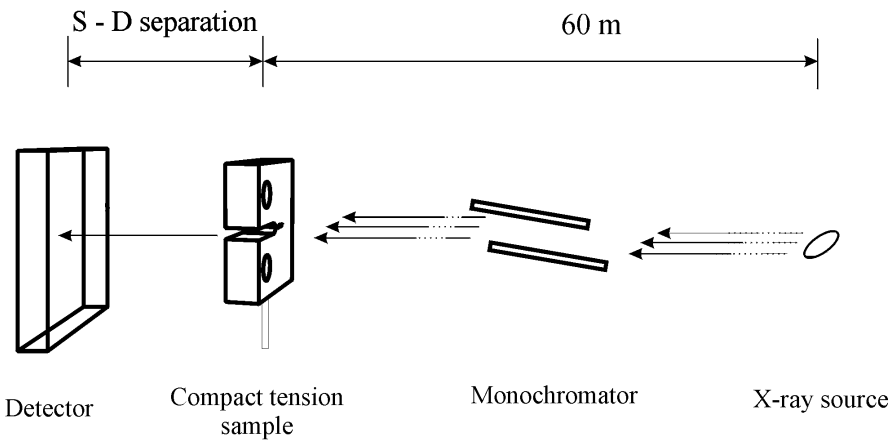

Figure 5: Schematic of the experiment layout at the APS beamline 1-ID. Sample can be rotated about the vertical as well as horizontal (perpendicular to the X-ray beam) axis and sample–detector distance can be varied.

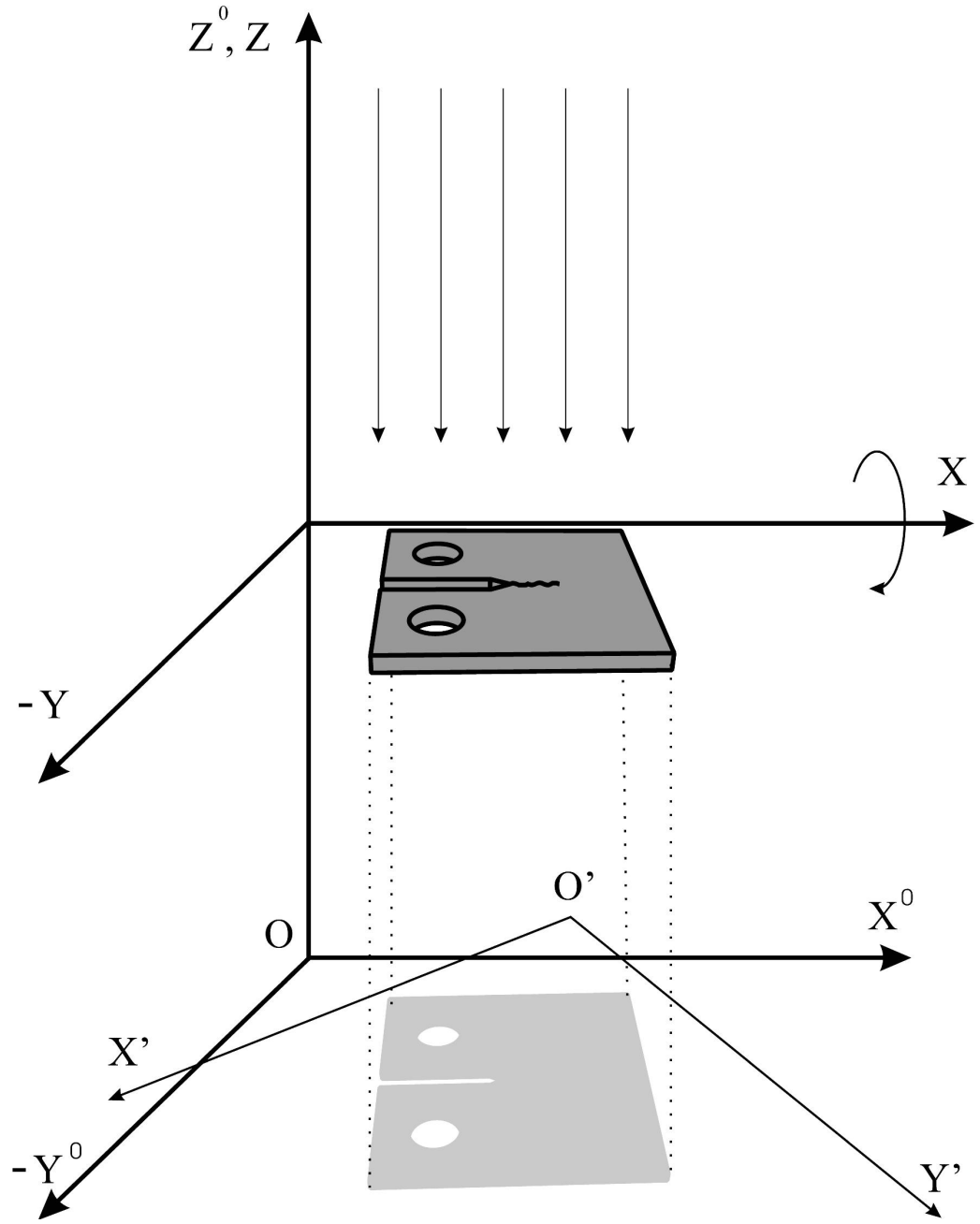

Figure 6: Coordinate systems used for 3D stereo reconstruction. Here (XYZ) is the sample coordinate system, $(X'O'Y')$ is the detector coordinate system and $(X^0Y^0Z^0)$ is the global coordinate system. Arrows represent X-ray beam. Coordinates of the projection are measured in the detector coordinate system $(X'O'Y')$

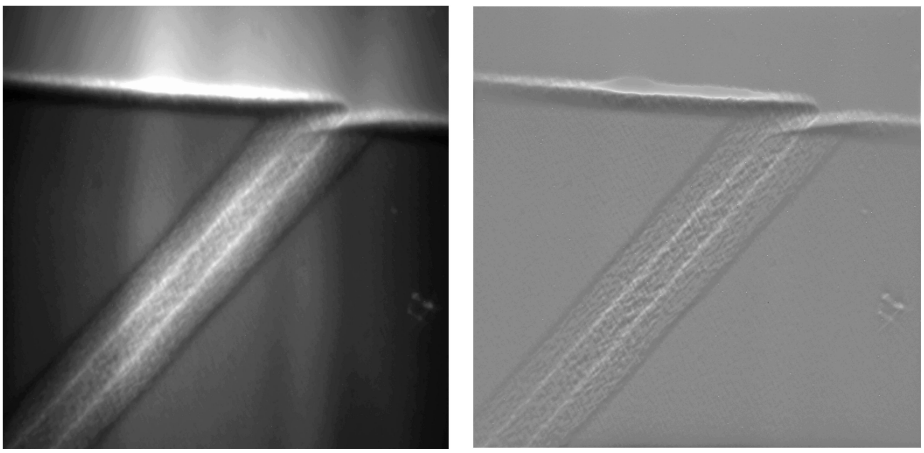

Figure 7: Comparison between unfiltered (left) and filtered (right) images of the cut in aluminum specimen. Filtering was done using 40th order Butterworth high-pass filter with modified kernel to reduce appearance of the vertical streaks that arise from the beam inhomogeneity

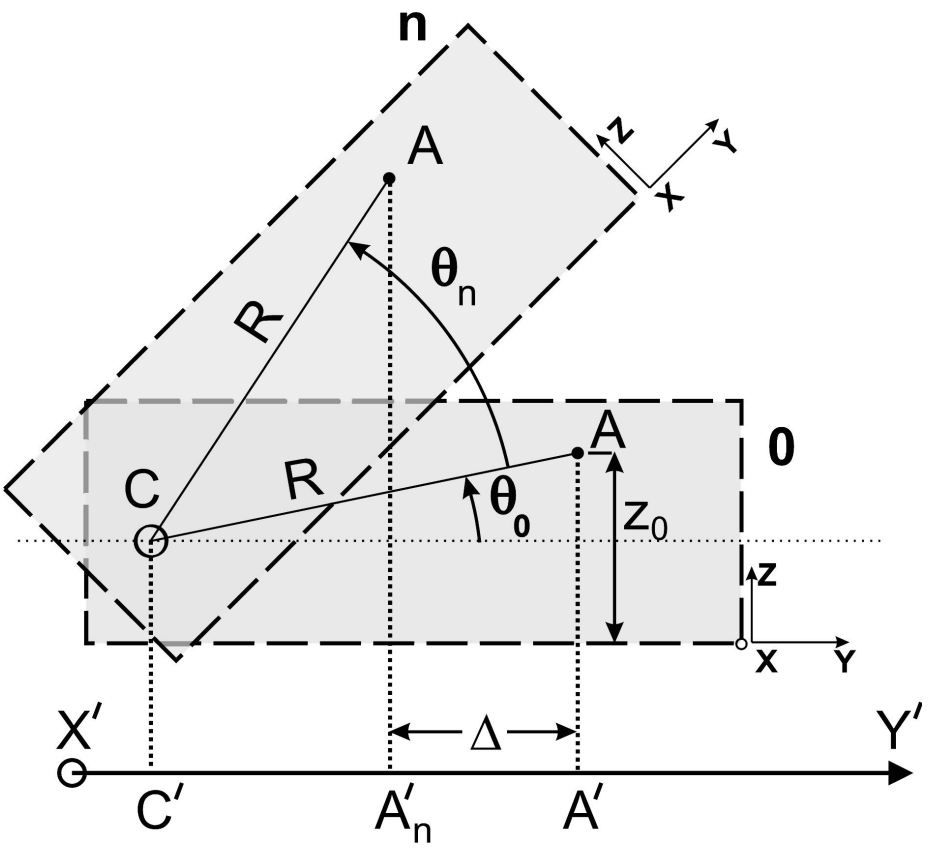

Figure 8: Schematic of a 3D reconstruction process from 2D projections. Two orientations are shown. X'Y' is the detector coordinate system, XYZ is the sample coordinate system and C is the rotation axis. A is the feature of interest in the sample and A' is its projection on the detector plane.

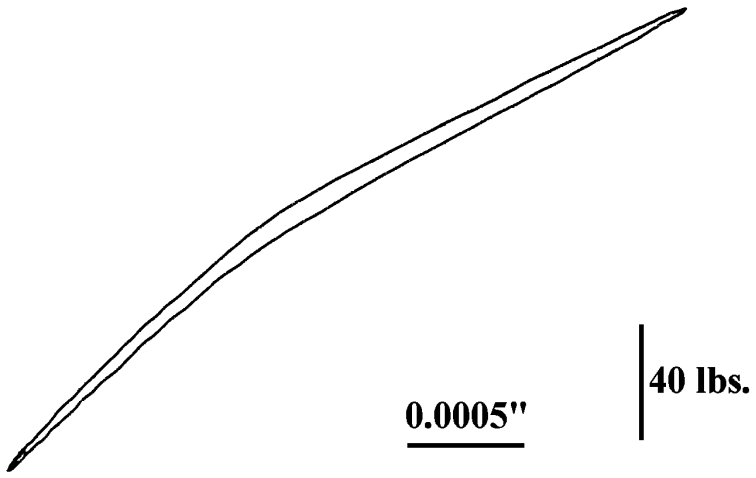

Figure 9: Experimental stress – strain curve recorded for sample CT-32M with crack length used for the first microtomography measurements of this sample. The minimum load is 8.2 kgf and the maximum is 80.7 kgf

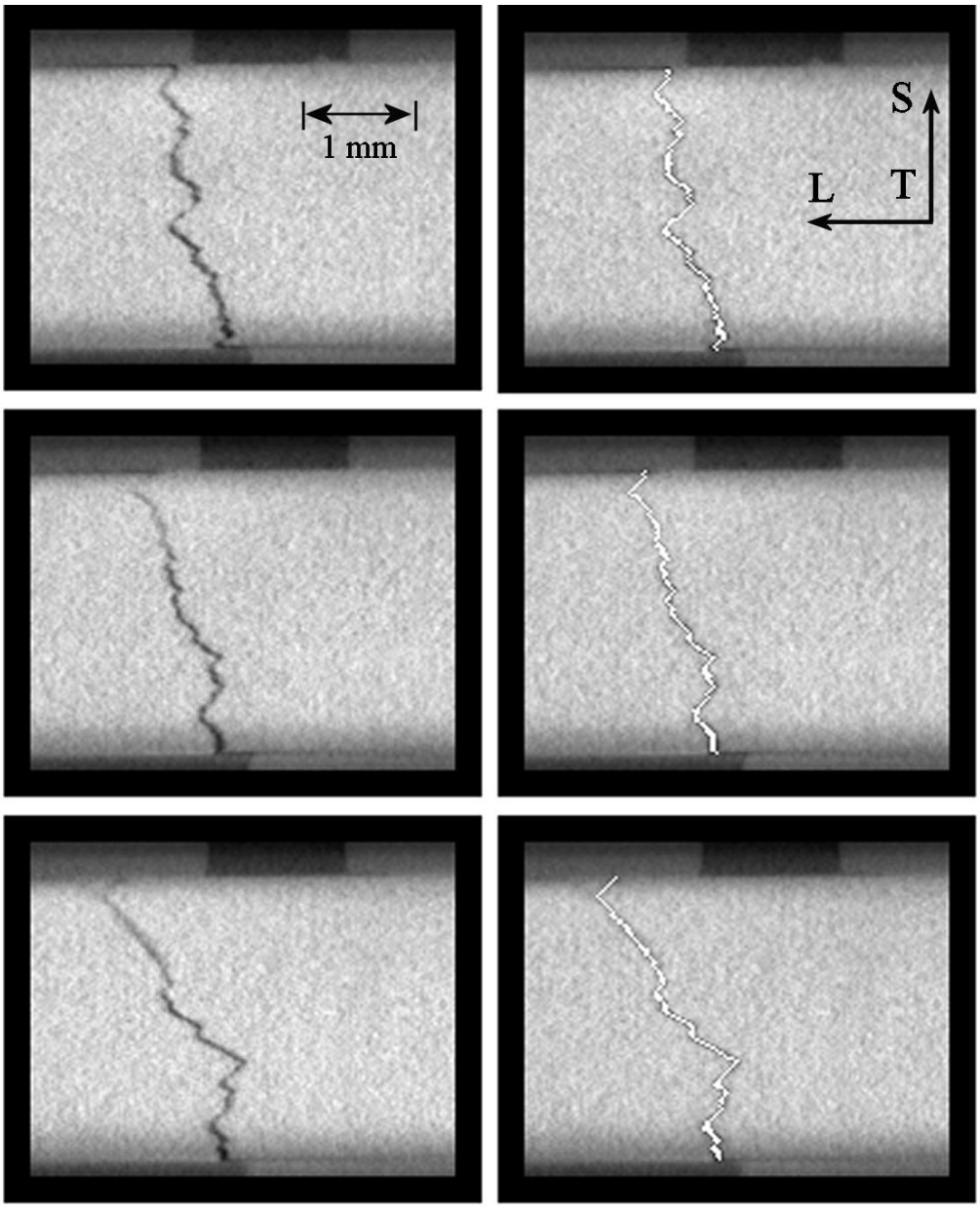

Figure 10: Reconstructed microCT cuts of sample CT-32M. On the right - output of the crack determination algorithm is superimposed on the original cuts (shown in white). Spacing between cuts is 464 μm in T direction.

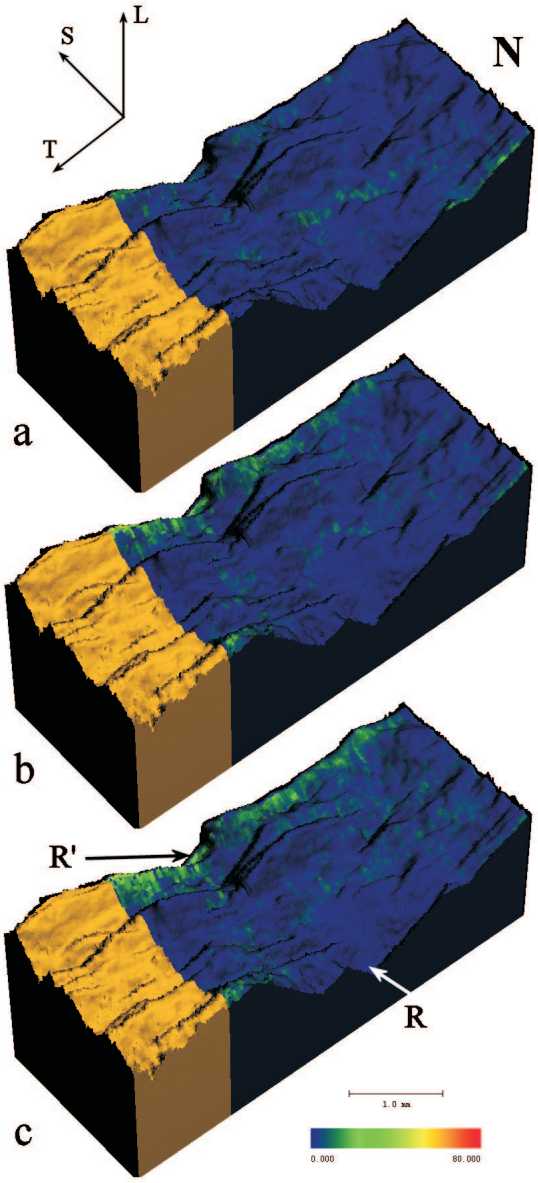

Figure 11: First viewing perspective of sample CT-32M (initial crack length) at loads of 0 (a), 8.4 (b) and 22.6 kgf (c). Crack opening data is superimposed on the 3D crack surface obtained with absorption microCT. Colors represent the amount of opening with red marking the highest opening (80 μm or more) and blue - the smallest opening (0 μm). "N" marks the crack notch and arrows show the sample orientation. The crack propagates in T direction.

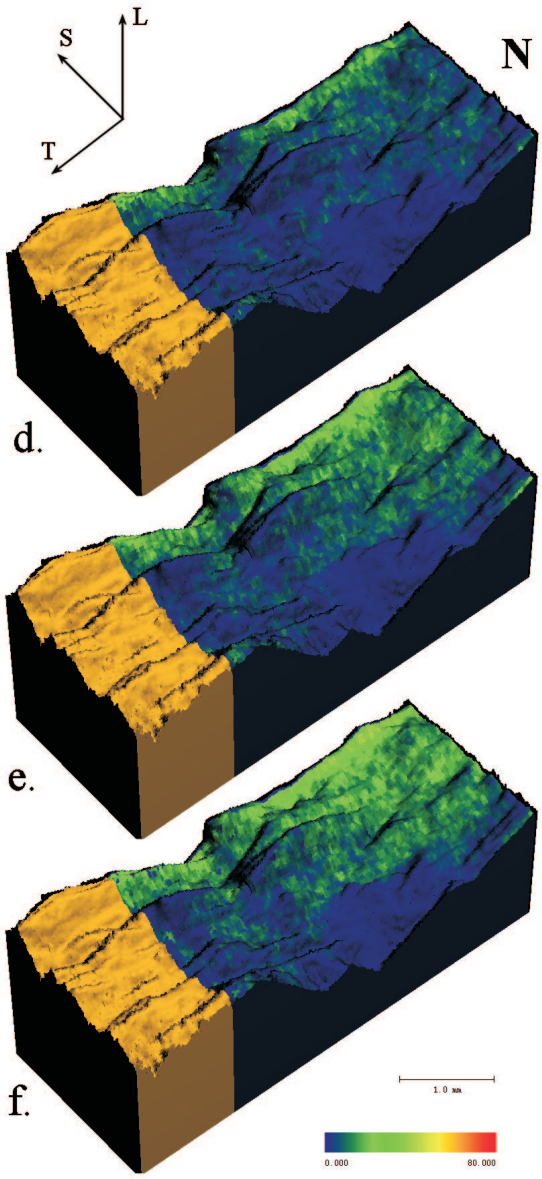

Figure 11: (cont.) First viewing perspective of sample CT-32M (initial crack length) at loads of 37.1 (d), 51.7 (e) and 60.5 kgf (f). Crack opening data is superimposed on the 3D crack surface obtained with absorption microCT. Colors represent the amount of opening with red marking the highest opening (80 μm or more) and blue - the smallest opening (0 μm). "N" marks the crack notch and arrows show the sample orientation. The crack propagates in the T direction.

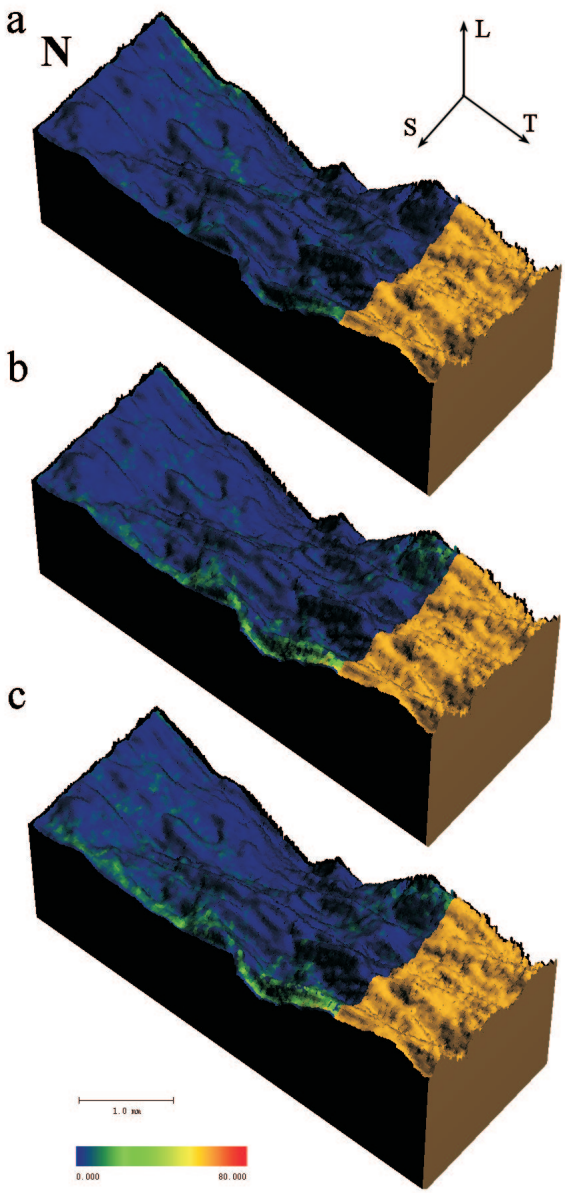

Figure 12: Second viewing perspective of sample CT-32M (initial crack length) at loads of 0 (a), 8.4 (b) and 22.6 kgf (c). Crack opening data is superimposed on the 3D crack surface obtained with absorption microCT. Colors represent the amount of opening with red marking the highest opening (80 μm or more) and blue - the smallest opening (0 μm). "N" marks the crack notch and arrows show the sample orientation. The crack propagates in the T direction.

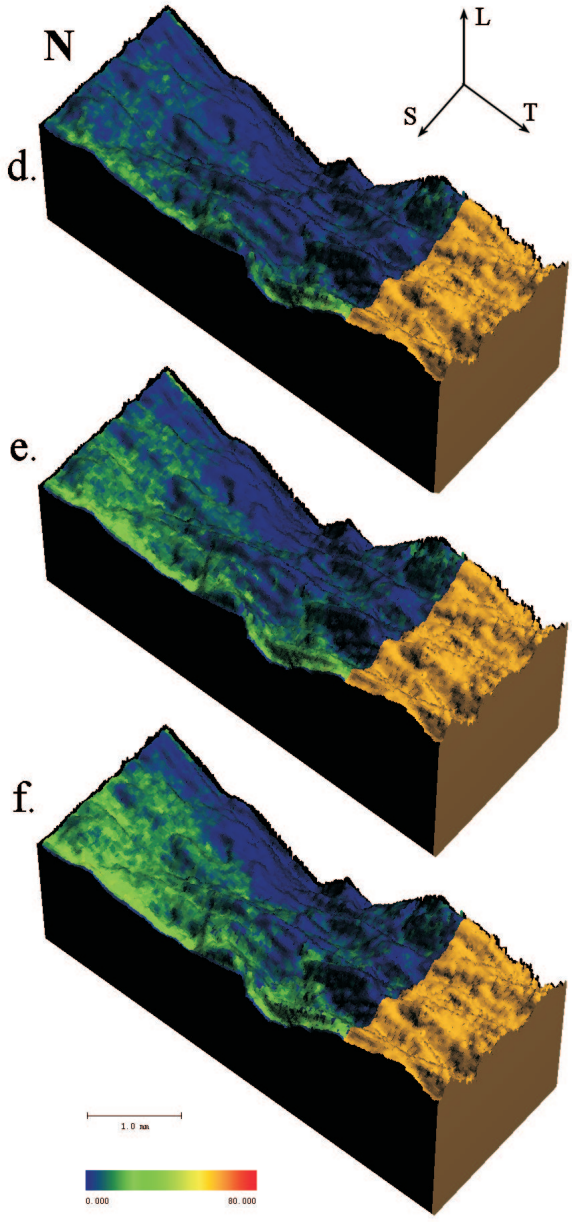

Figure 12: (cont.) Second viewing perspective of sample CT-32M (initial crack length) at loads of 37.1 (d), 51.7 (e) and 60.5 kgf (f). Crack opening data is superimposed on the 3D crack surface obtained with absorption microCT. Colors represent the amount of opening with red marking the highest opening (80 μm or more) and blue - the smallest opening (0 μm). "N" marks the crack notch and arrows show the sample orientation. The crack propagates in the T direction.

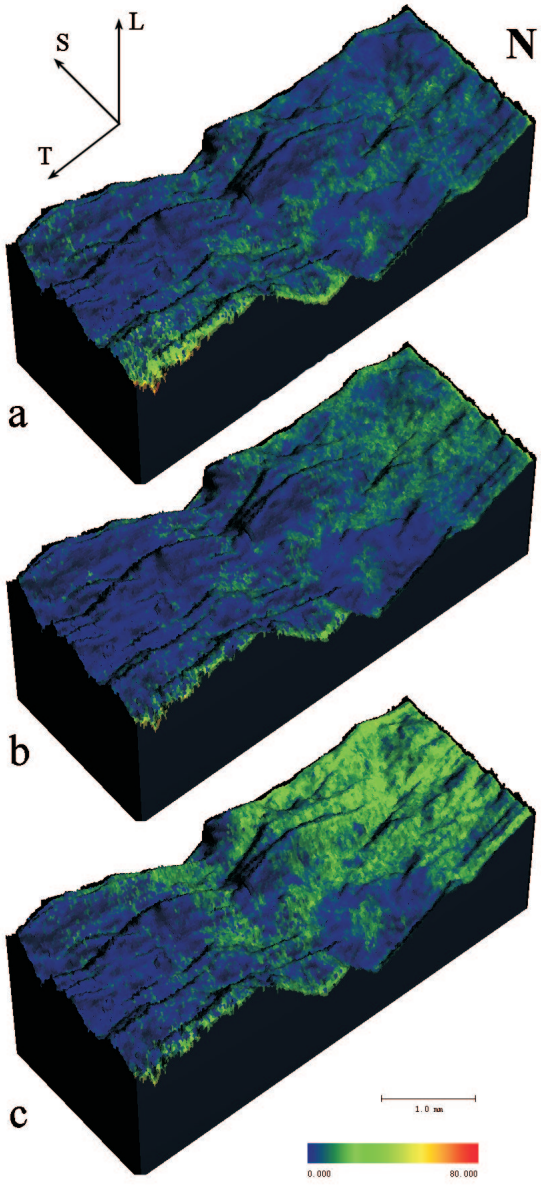

Figure 13: First viewing perspective of sample CT-32M (final crack length) at loads of 8.0 (a), 22.6 (b) and 37.4 kgf (c). Crack opening data is superimposed on the 3D crack surface obtained with absorption microCT. Colors represent the amount of opening with red marking the highest opening (80 μm or more) and blue - the smallest opening (0 μm). "N" marks the crack notch and arrows show the sample orientation. The crack propagates in the T direction.

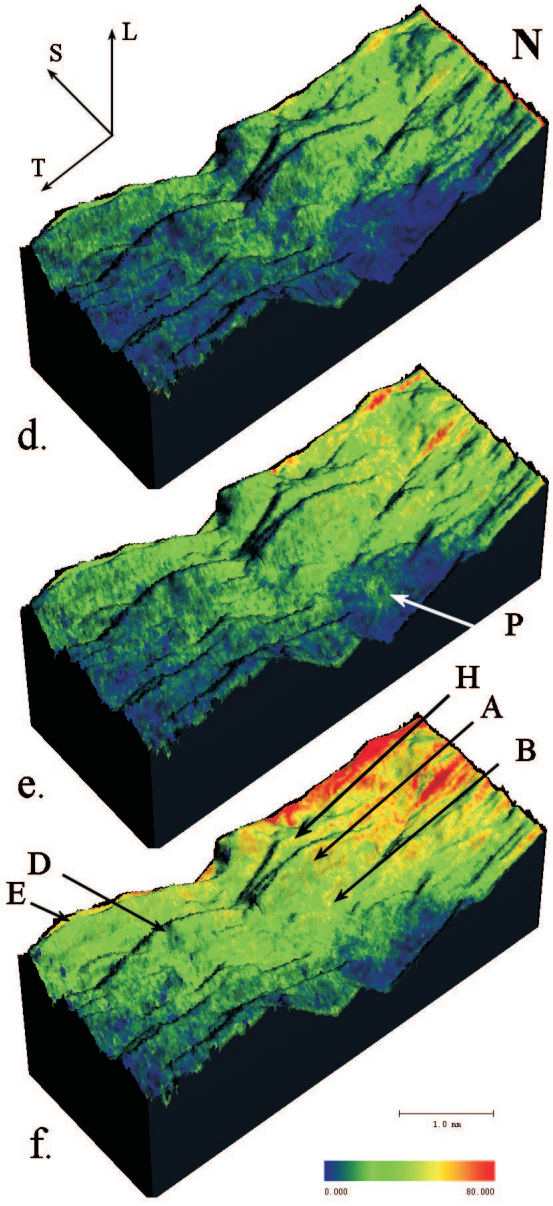

Figure 13: (cont.) First viewing perspective of sample CT-32M (final crack length) at loads of 52.5 (d), 66.2 (e) and 83.9 kgf (f). Crack opening data is superimposed on the 3D crack surface obtained with absorption microCT. Colors represent the amount of opening with red marking the highest opening (80 μm or more) and blue - the smallest opening (0 μm). "N" marks the crack notch and arrows show the sample orientation. The crack propagates in the T direction.

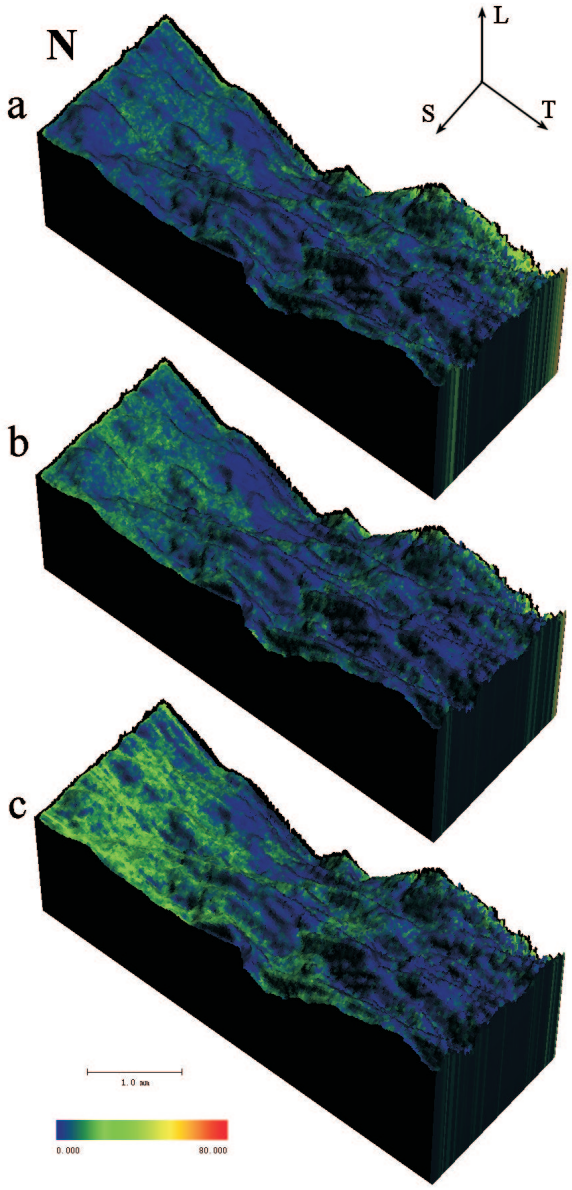

Figure 14: Second viewing perspective of sample CT-32M (final crack length) at loads of 8.0 (a), 22.6 (b) and 37.4 kgf (c). Crack opening data is superimposed on the 3D crack surface obtained with absorption microCT. Colors represent the amount of opening with red marking the highest opening (80 μm or more) and blue - the smallest opening (0 μm). "N" marks the crack notch and arrows show the sample orientation. The crack propagates in the T direction.

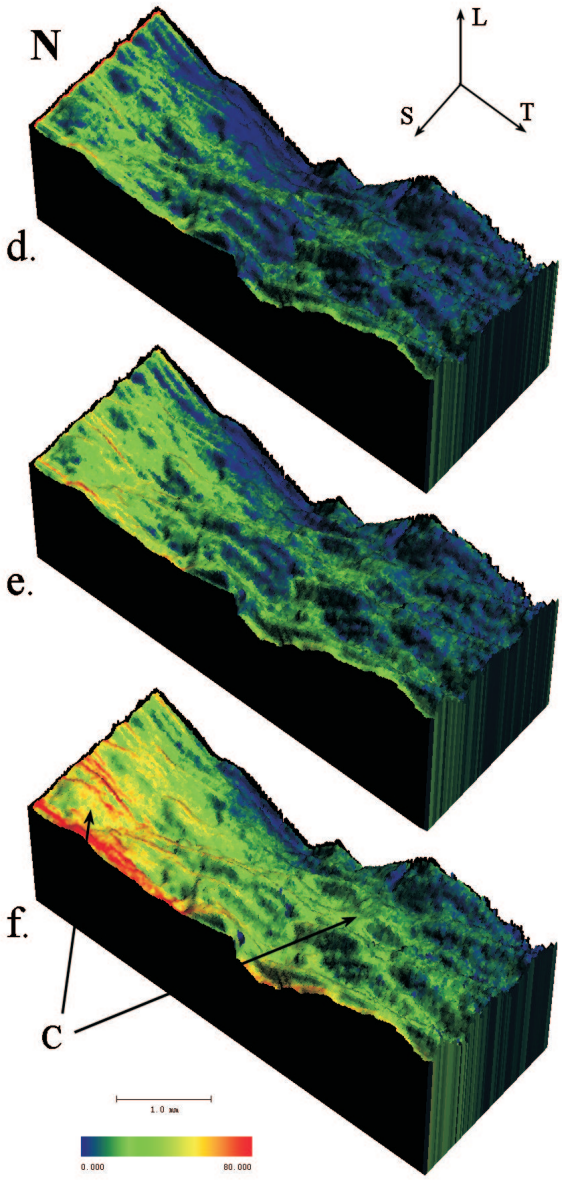

Figure 14: (cont.) Second viewing perspective of sample CT-32M (final crack length) at loads of 52.5 (d), 66.2 (e) and 83.9 kgf (f). Crack opening data is superimposed on the 3D crack surface obtained with absorption microCT. Colors represent the amount of opening with red marking the highest opening (80 μm or more) and blue - the smallest opening (0 μm). "N" marks the crack notch and arrows show the sample orientation. The crack propagates in the T direction.

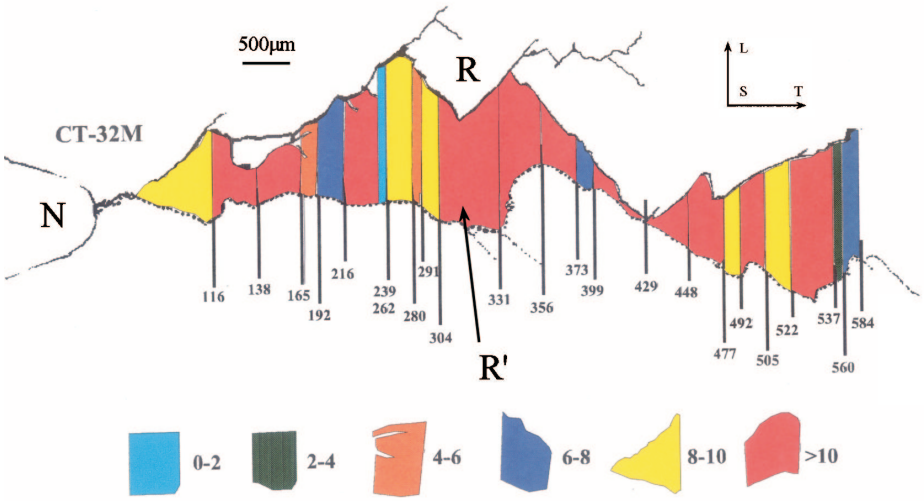

Figure 15: Crack growth rates for sample CT-32M. Crack tip position is labeled in 10^3 cycles and crack profiles for both faces is shown, with color fill between the profiles showing the local crack growth rates. Legend at the bottom of the figure relate color to the crack growth rates in 10^{-9} meters/cycle units. "N" marks the crack notch and arrows show the sample orientation. Figure was created in most part by Robert Morano. "R" and "R' " refer to sample positions shown in Figure 11c.

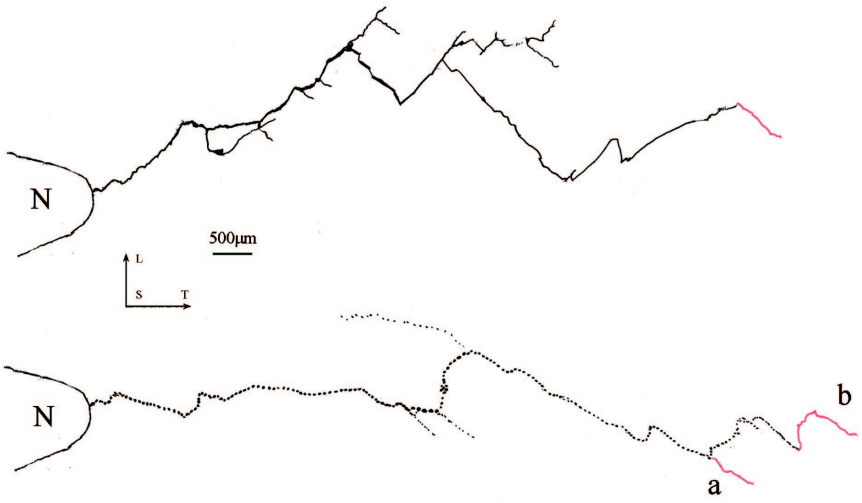

Figure 16: In the 155K cycles added after Figure 15 was recorded, the crack extended along surface paths shown in red. Branch "a" formed first and "b" formed second.

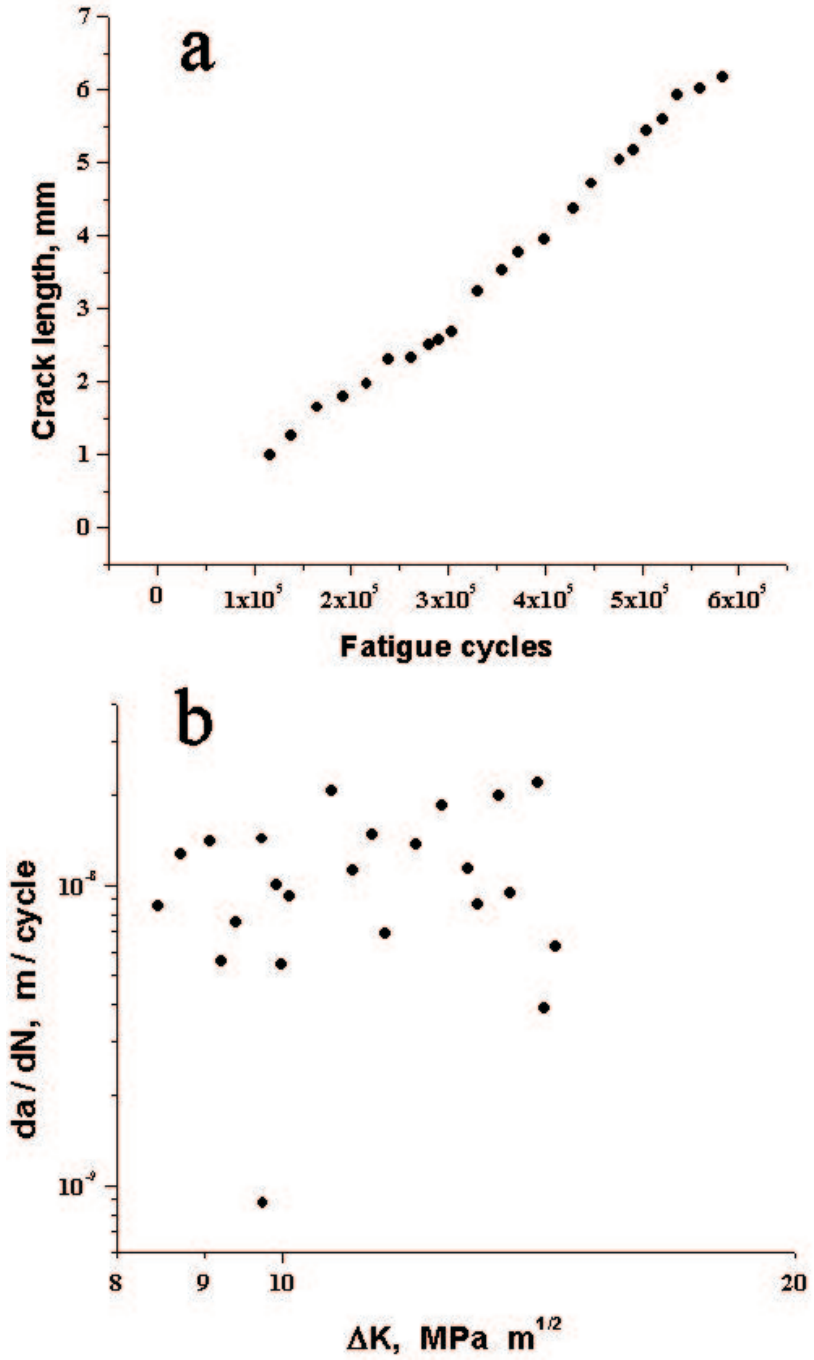

Figure 17: Crack length as a function of the number of fatigue cycles applied (a) and fatigue crack growth rate as a function of stress intensity factor range (b) for sample CT-32M.

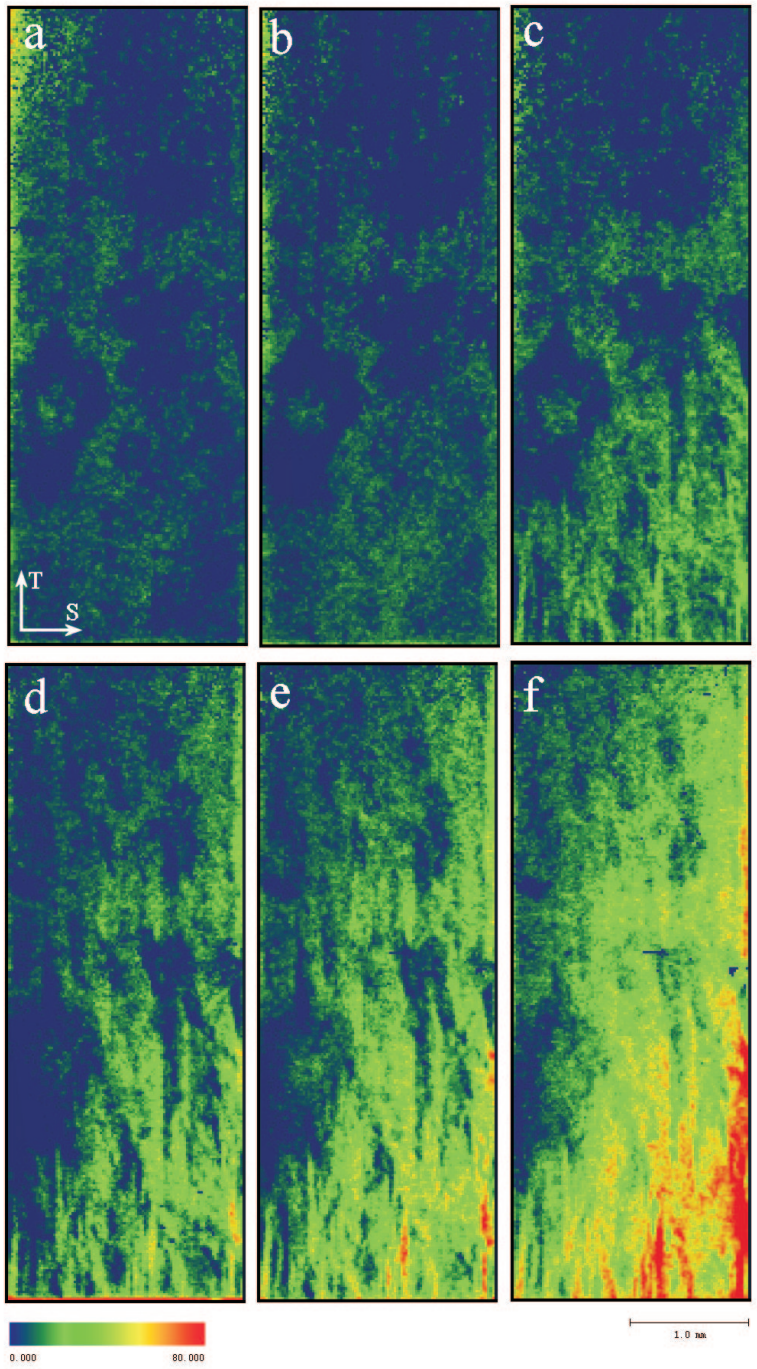

Figure 18: Crack opening in sample CT-32M (final crack length) at loads of 8.0 (a), 22.6 (b), 37.4 (c), 52.5 (d), 66.2 (e) and 83.9 kgf (f). Colors represent the amount of opening with red marking the highest opening (80 μm or more) and blue - the smallest opening (0 μm). The crack propagates in the T direction.

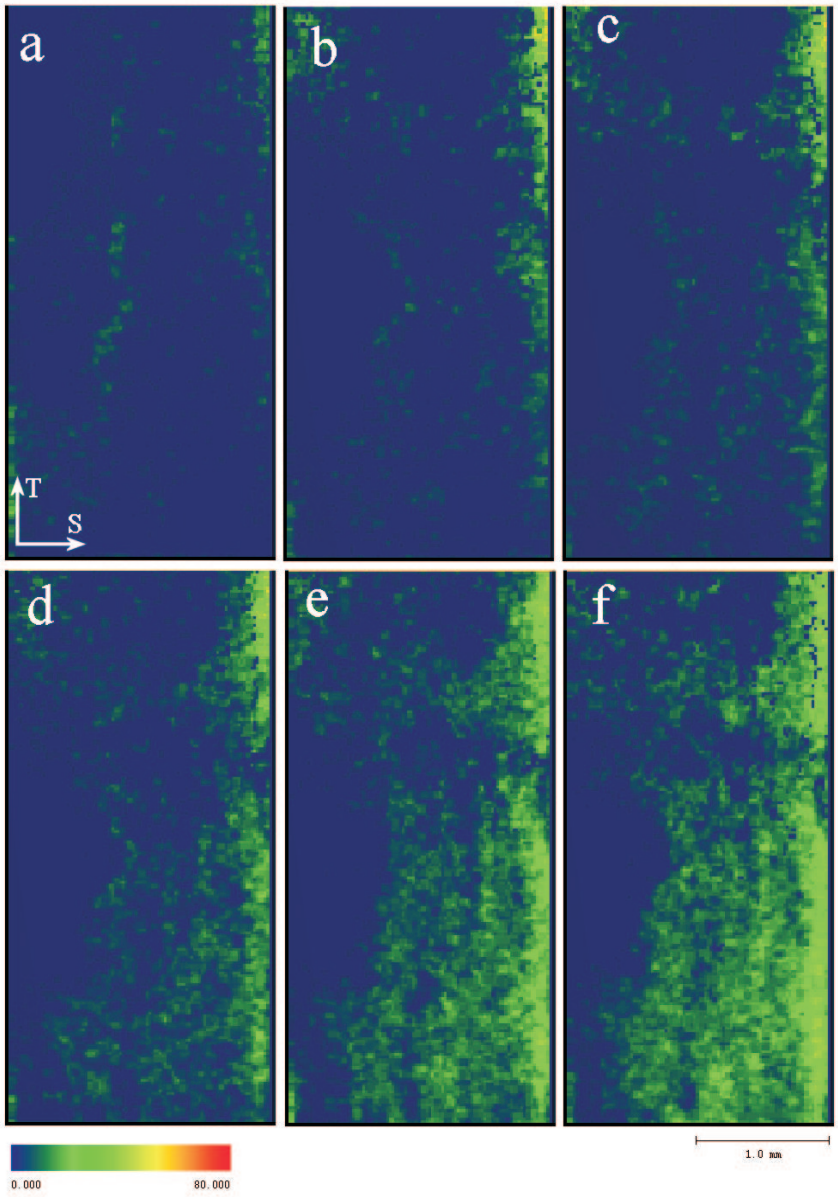

Figure 19: Crack opening in sample CT-32M (initial crack length) at loads of 0 (a), 8.4 (b), 22.6 (c), 37.1 (d), 51.7 (e) and 60.5 kgf (f). Colors represent the amount of opening with red marking the highest opening (80 μm or more) and blue - the smallest opening (0 μm). The crack propagates in the T direction.

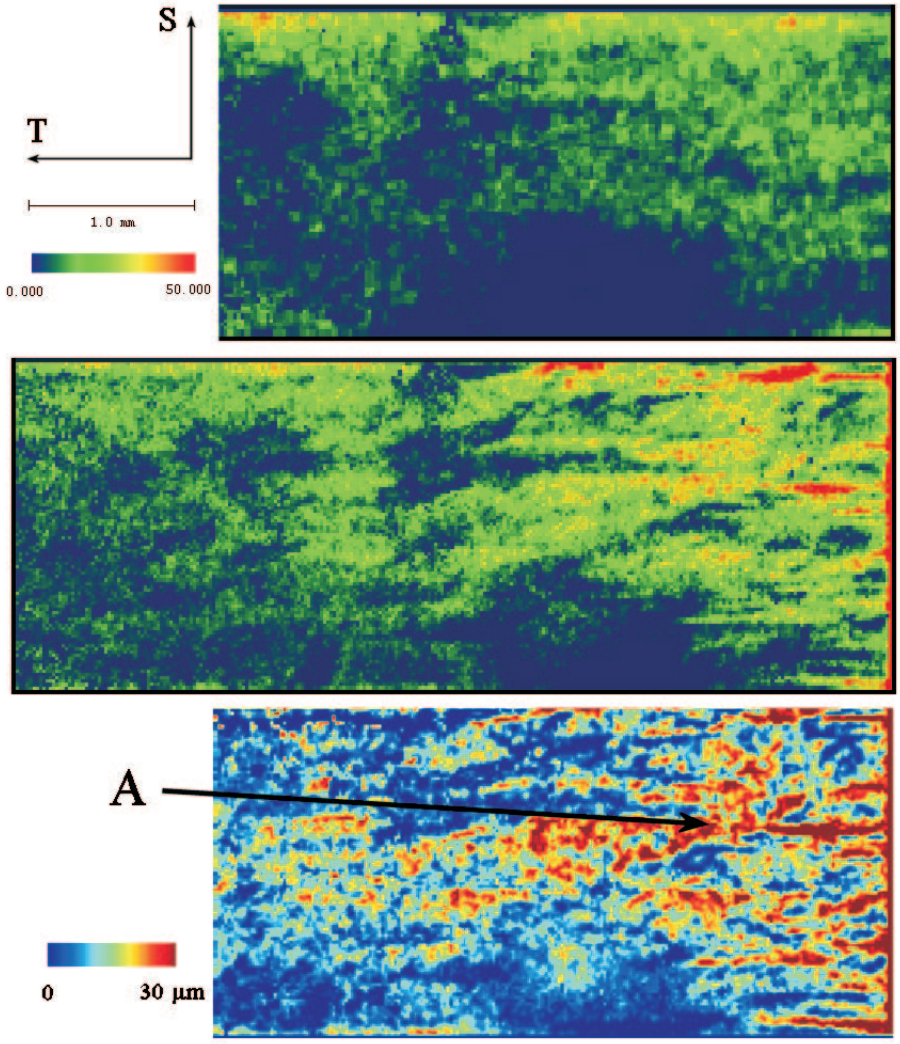

Figure 20: Opening maps for sample CT-32M before (top) and after crack extension (middle). The bottom image shows the difference between the two upper maps.

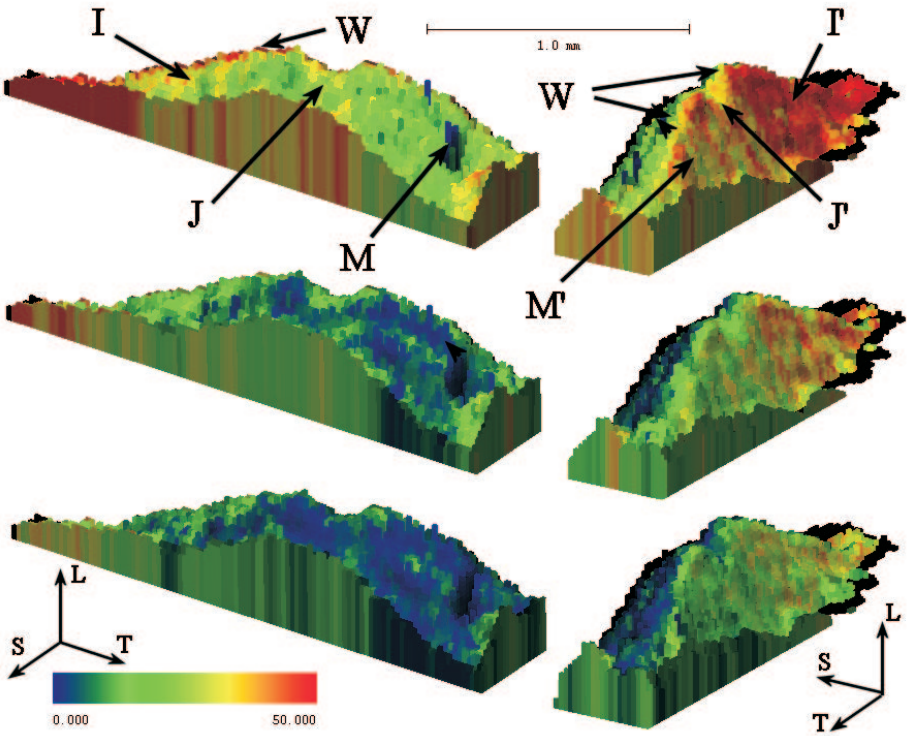

Figure 21: One of the asperities (after crack extension) on the crack surface of sample CT-32M with color representing local crack opening. Two orientations of the same asperity are shown (on the left and on the right) and the load is decreased from the top image (83.9 kgf) to the bottom (52.5 kgf).

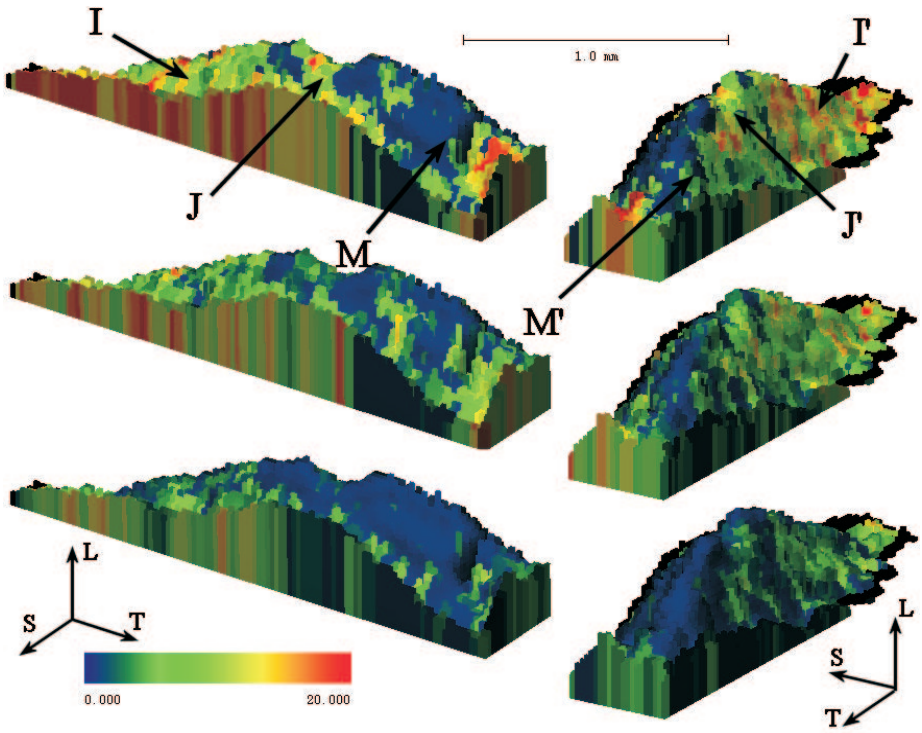

Figure 22: One of the asperities (before crack extension) on the crack surface of sample CT-32M with color representing local crack opening. Two orientations of the same asperity are shown (on the left and on the right) and the load is decreased from the top image (60.5 kgf) to the bottom (37.1 kgf).

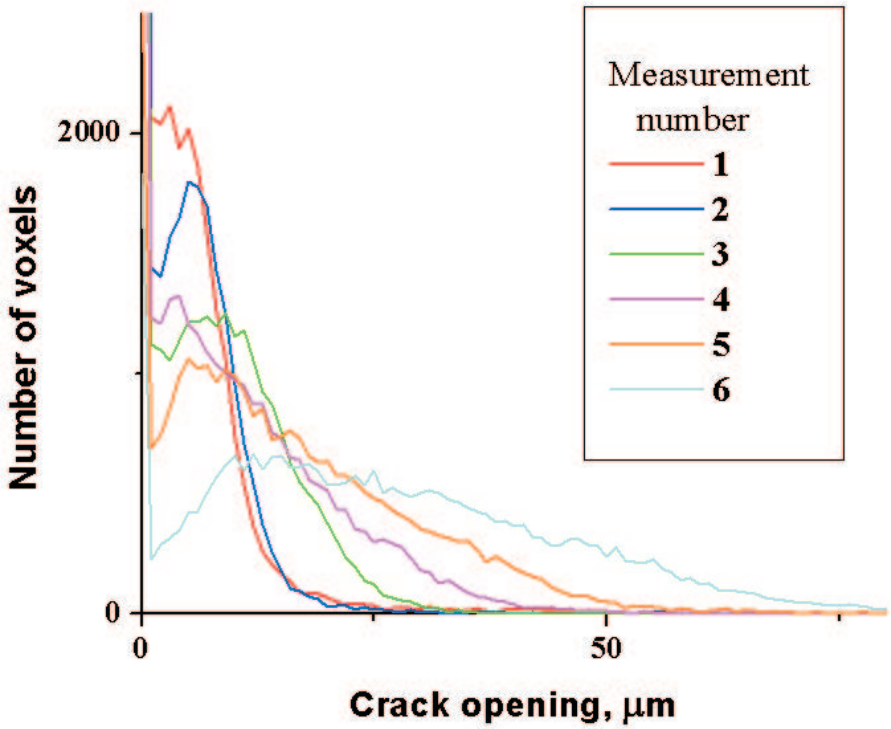

Figure 23: Histogram plot of the crack opening for different loads for the sample with extended crack.

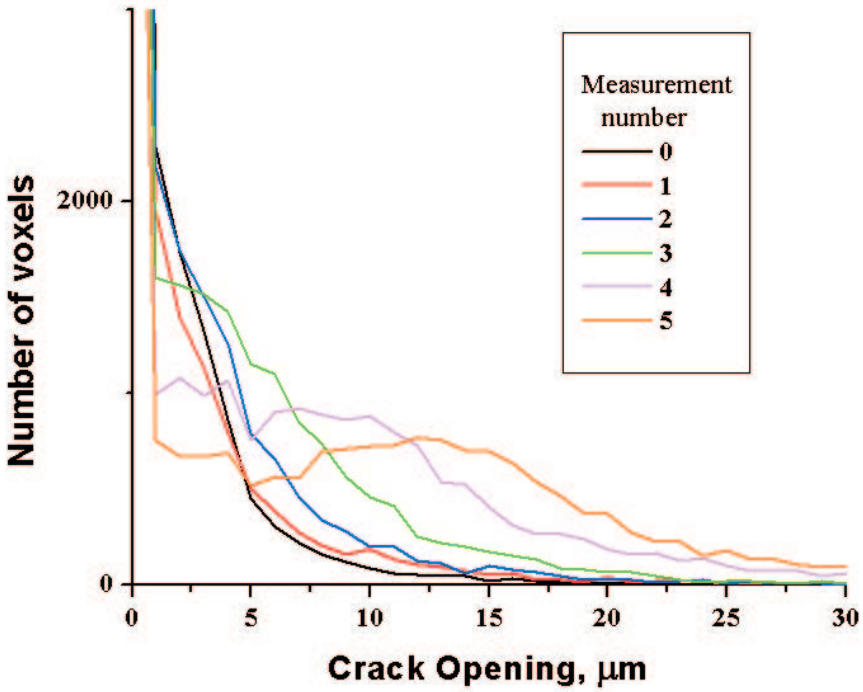

Figure 24: Histogram plot of the crack opening for different loads for the sample with initial crack.

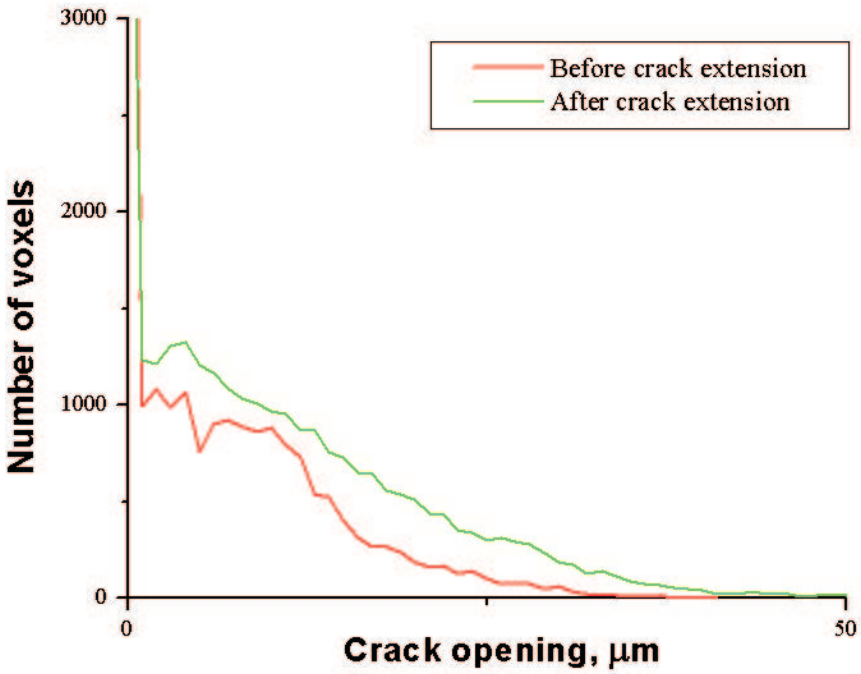

Figure 25: Histogram plot of the crack opening for sample before and after crack extension at 52 kgf load.

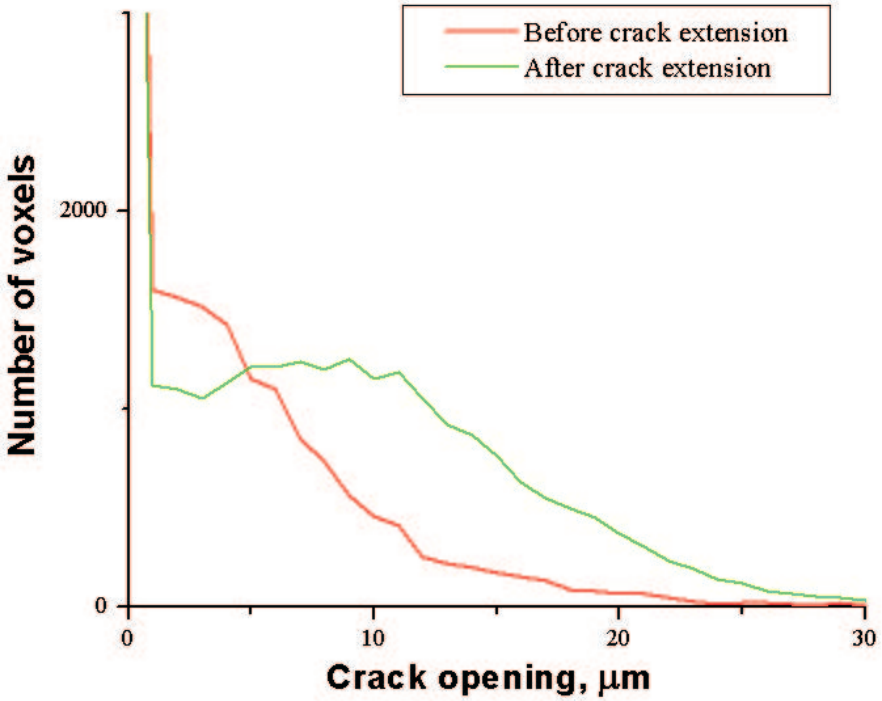

Figure 26: Histogram plot of the crack opening for sample before and after crack extension at 37 kgf load.

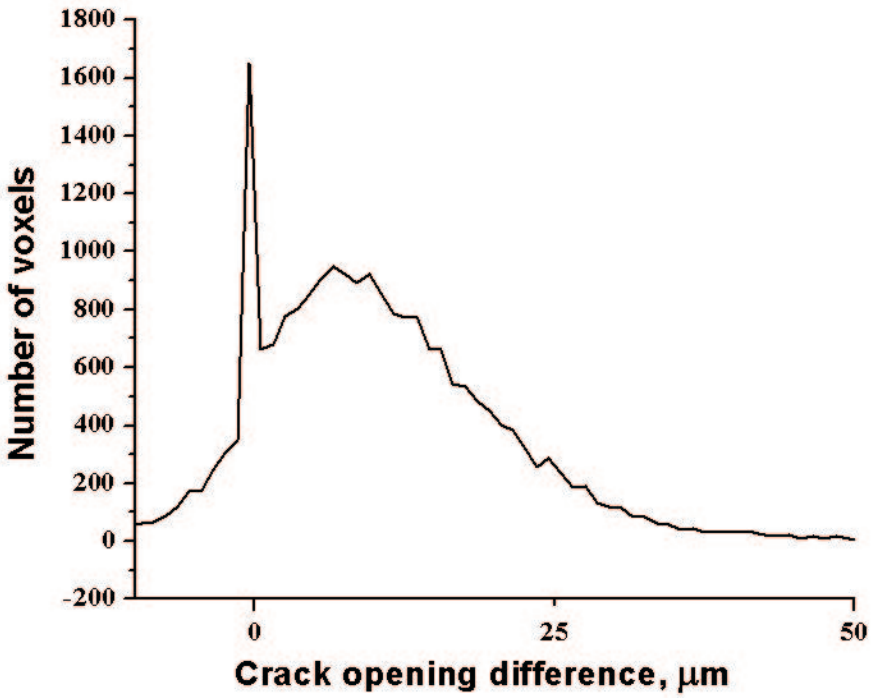

Figure 27: Histogram plot of the difference in crack opening for sample before and after crack extension at 52 kgf load.

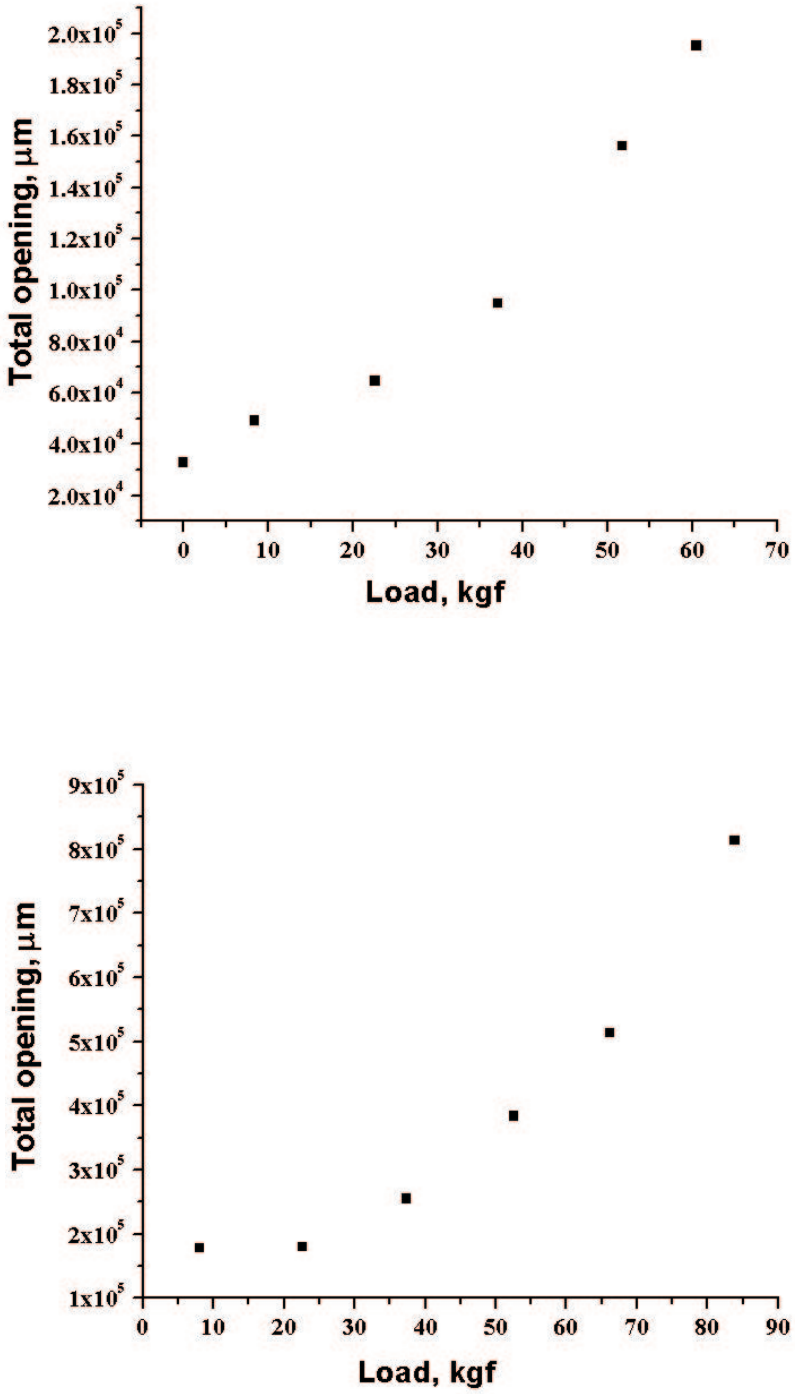

Figure 28: Plot of the amount of crack opening vs. the applied load for sample before(top) and after (bottom) crack extension.

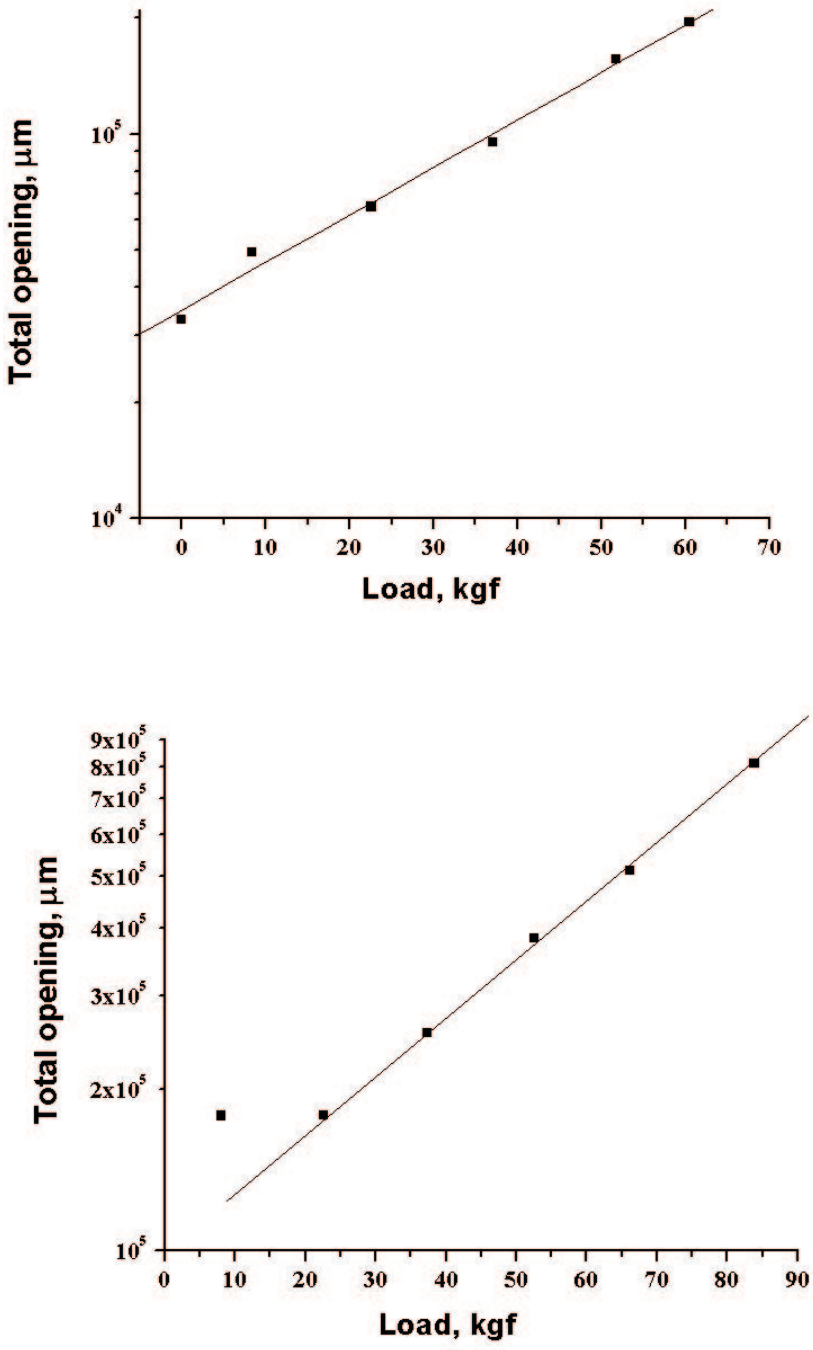

Figure 29: Semi-log plot of the amount of crack opening vs. the applied load for sample before(top) and after (bottom) crack extension.

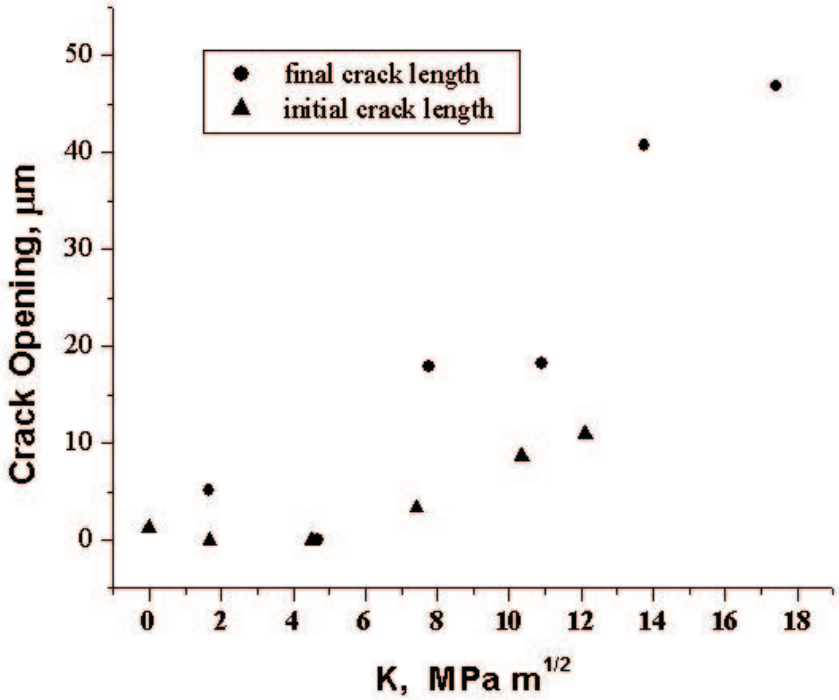

Figure 30: Crack opening at position A (marked on figure 13) before and after crack extension. Triangles mark opening for the initial crack length and circles mark opening for the extended crack.

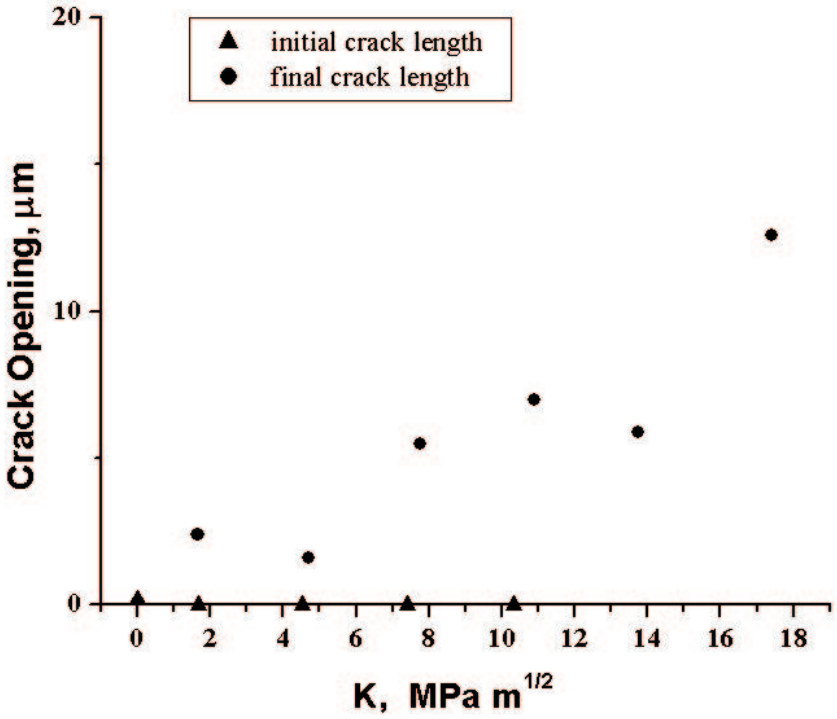

Figure 31: Crack opening at position B (marked on figure 13) before and after crack extension. Triangles mark opening for the initial crack length and circles mark opening for the extended crack.

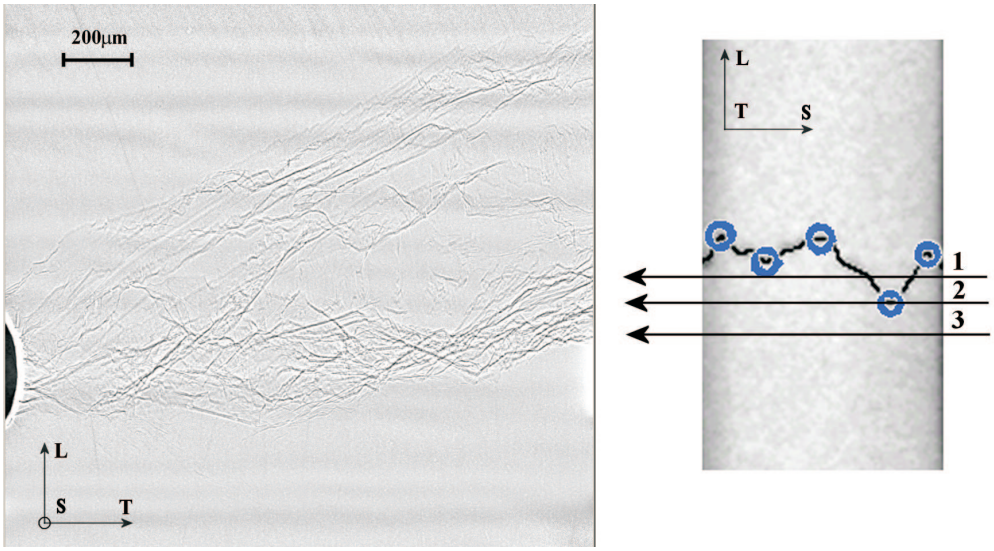

Figure 32: On the left is the X-ray radiograph of the area of the compact tension sample containing crack. The notch can be seen as a dark circular shape on the left, and the crack growth direction is to the right of the image. The image was corrected for beam and detector non-uniformities. Coordinate axis refer to the sample directions. On the right is a schematic showing the X-ray beam passing through the thickness of the sample. The dark line represents the crack and circles represent sharp changes in crack geometry.

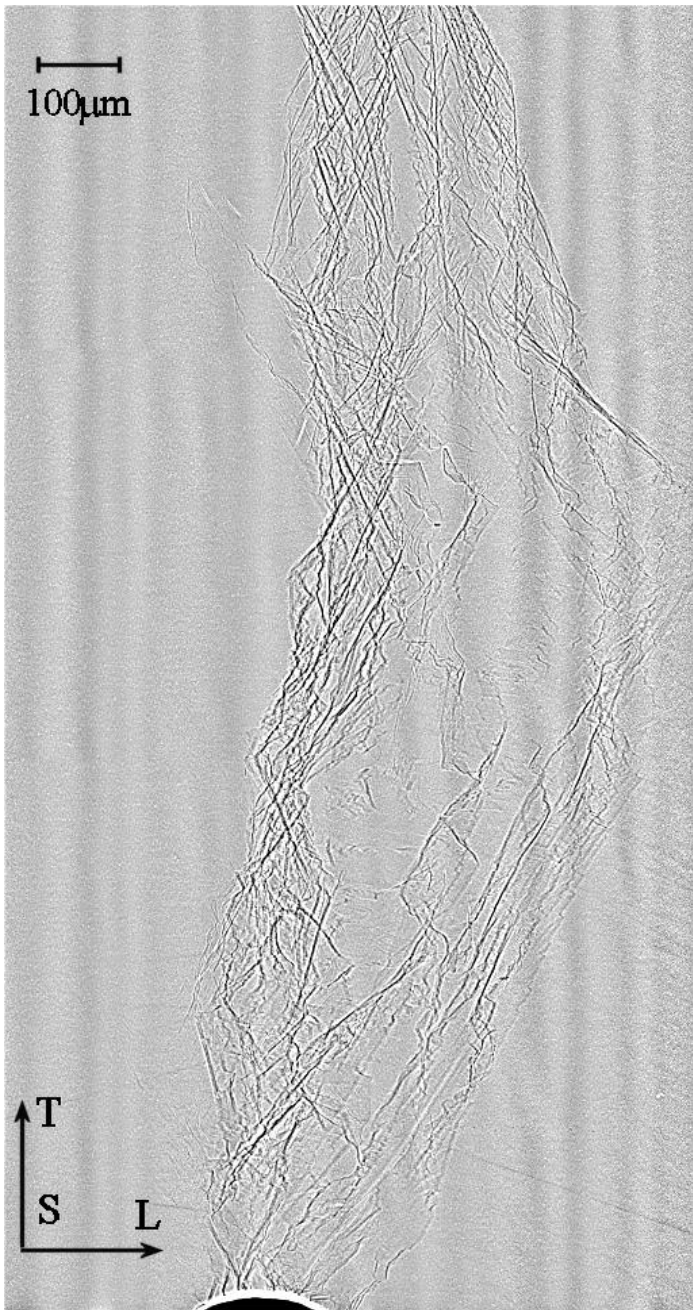

Figure 33: Phase contrast microradiograph of the first half of the crack in sample CT-41M. The X-ray beam is perpendicular to the plane of the sample.

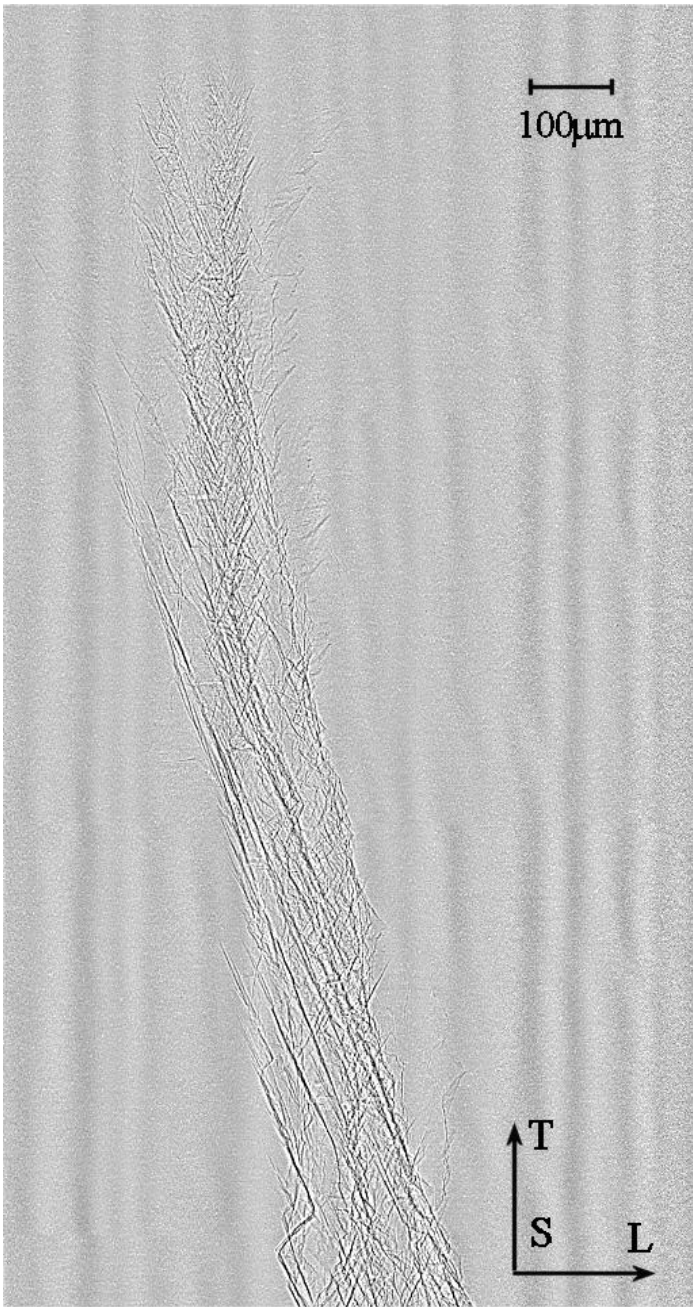

Figure 34: Phase contrast microradiograph of the second half of the crack in sample CT-41M in the same orientation as Figure 33

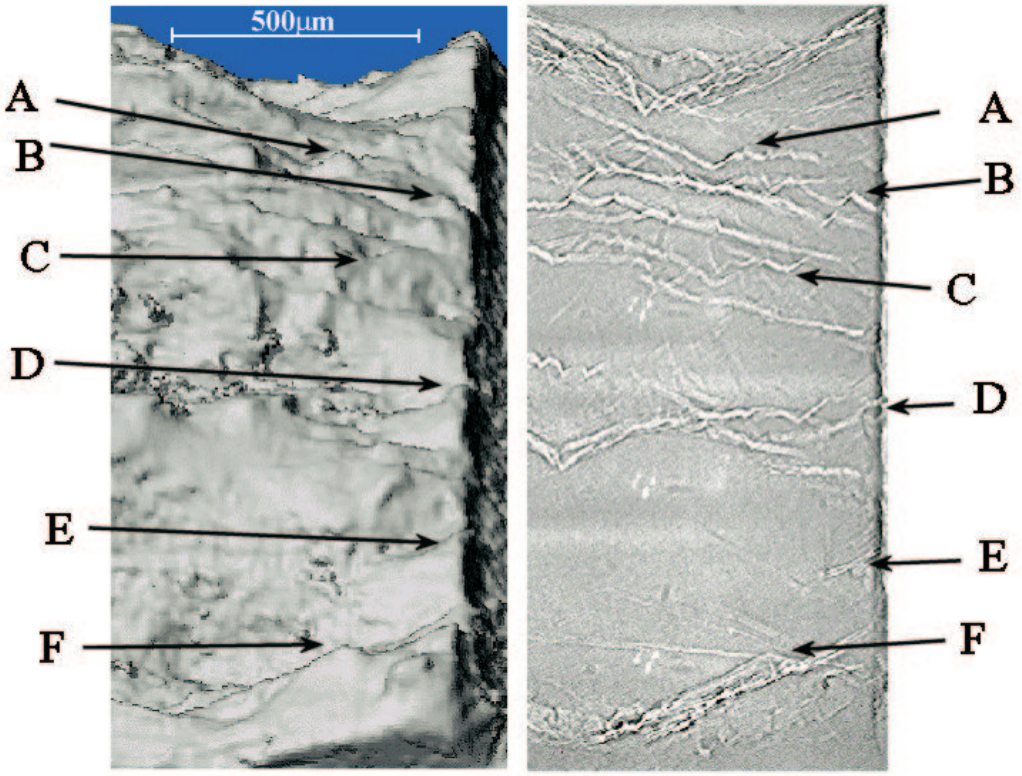

Figure 35: 3D rendering of the crack surface of sample CT-33M obtained with absorption microtomography is on the left and the phase contrast microradiograph of the same position and orientation of the sample is on the right. Letters mark identical features on the crack surface

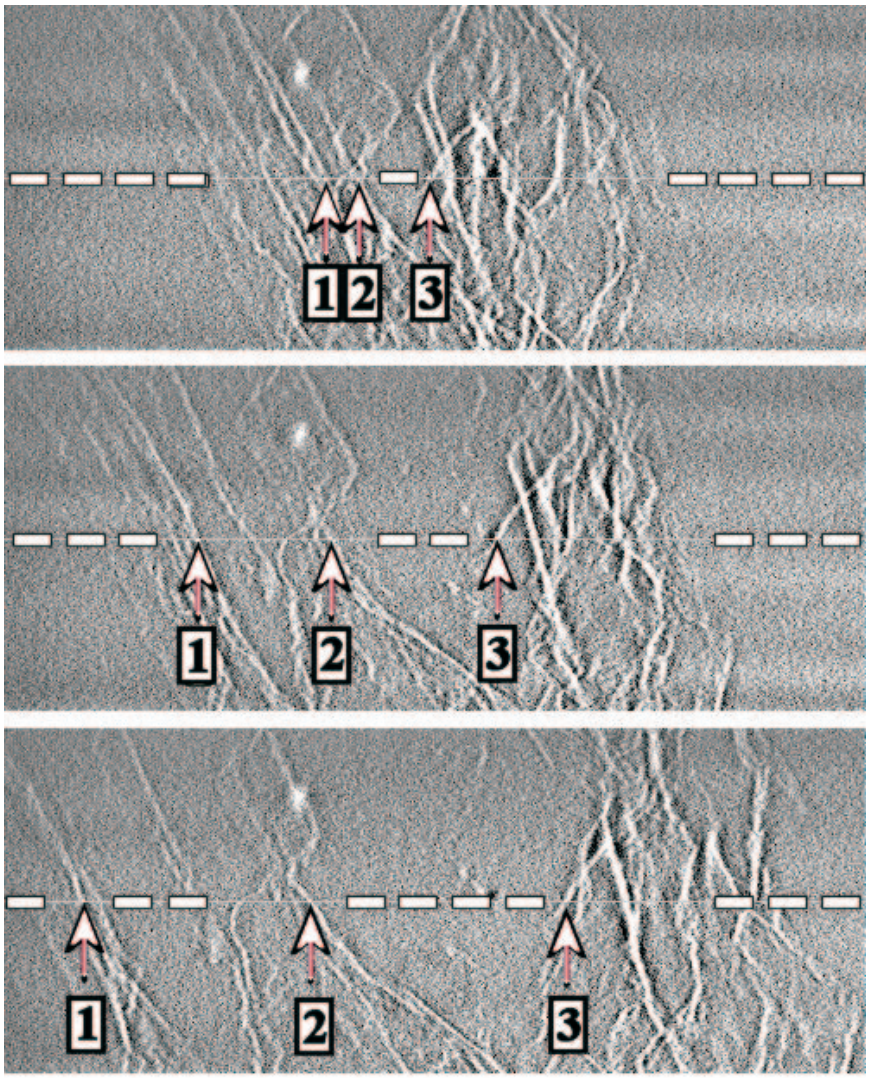

Figure 36: Three radiographs of the same area but at different sample rotations. Angular distance between adjacent radiographs is ten degrees and the crack growth direction is to the top. White horizontal straight line represents constant T position on all radiographs and positions of three features of interest that change with sample rotation are numbered.

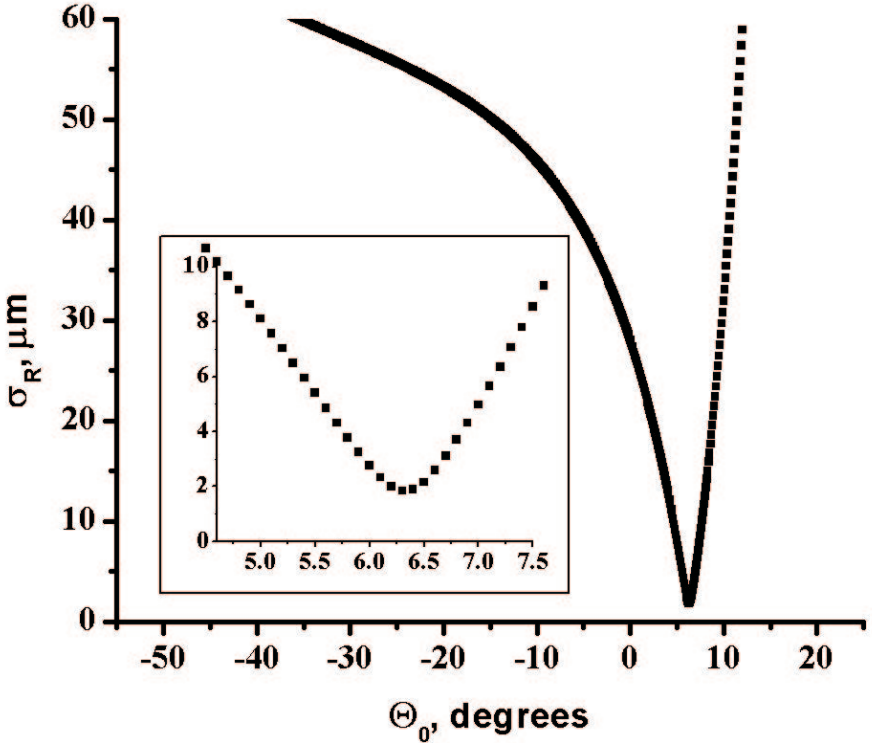

Figure 37: Typical change of standard deviation of set of R's with θ_0 (initial angle). Inset shows magnified area near the curve minimum.

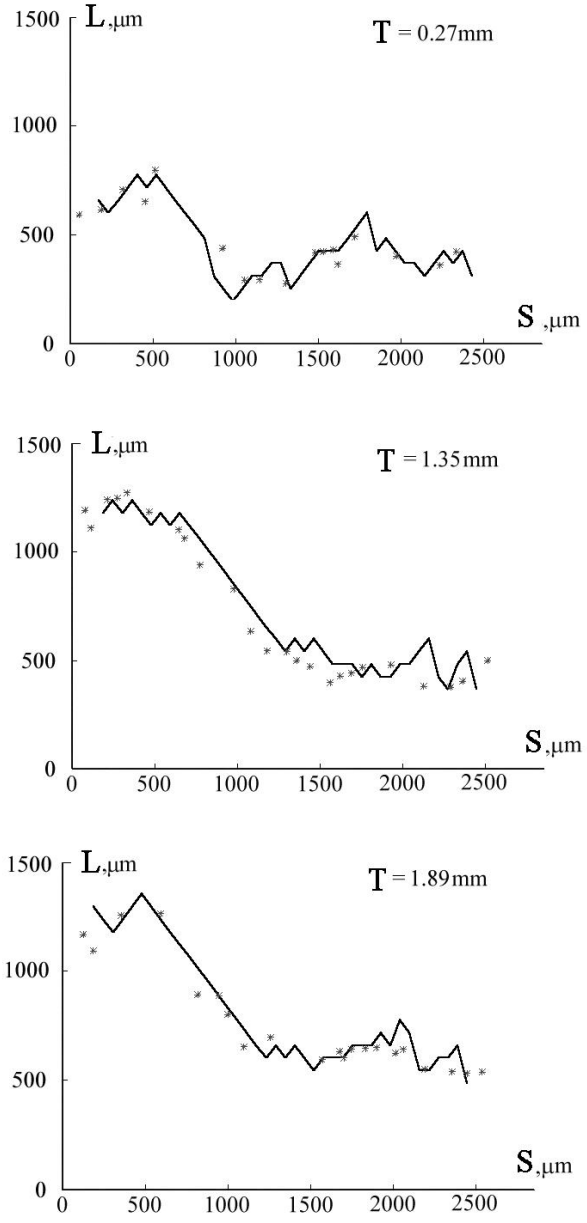

Figure 38: Profiles of crack height at different distances from the notch. Solid black line shows profiles obtained with absorption microtomography and markers show crack positions obtained with phase radiographs and stereo reconstruction.

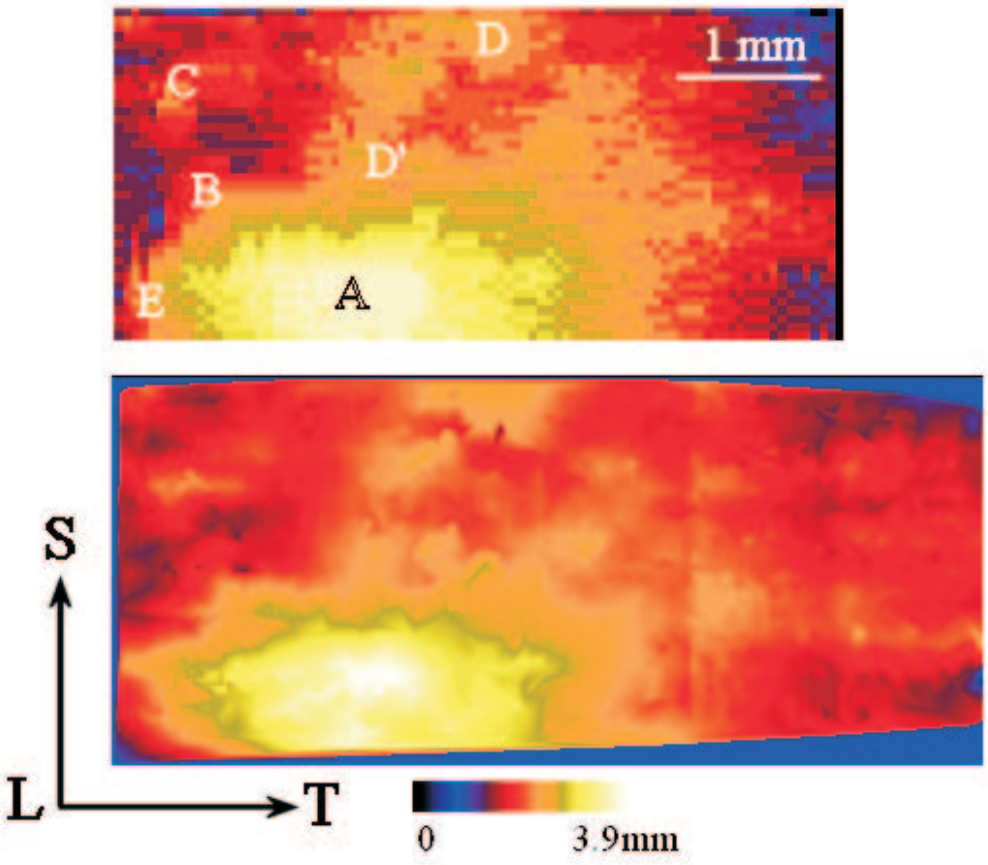

Figure 39: Color coded map of the crack surface obtained with absorption micro-tomography (top) and phase contrast stereometry (bottom)

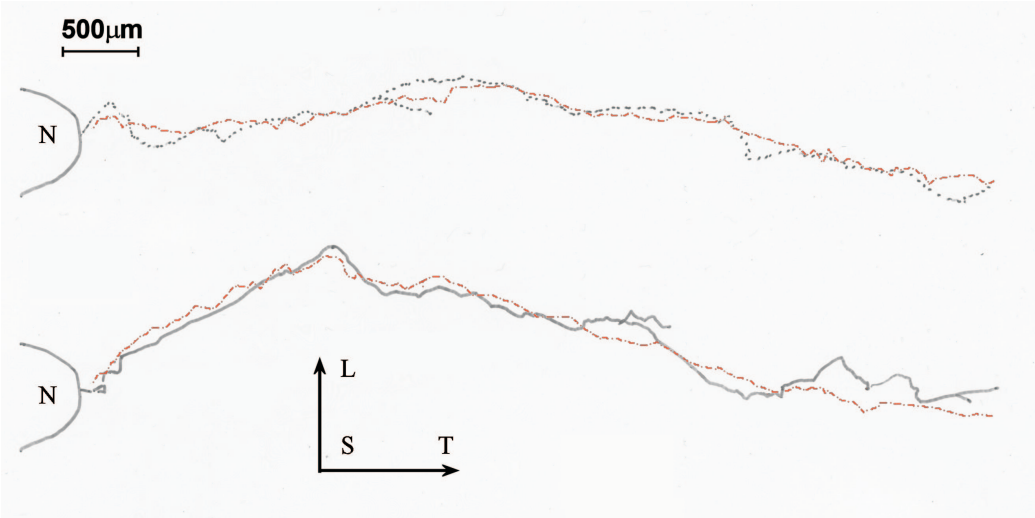

Figure 40: Comparison of crack path from the exterior of the same sample obtained with optical microscopy (black line) and phase contrast stereometry (red line) for two sample faces (front and back). "N" marks the crack notch.

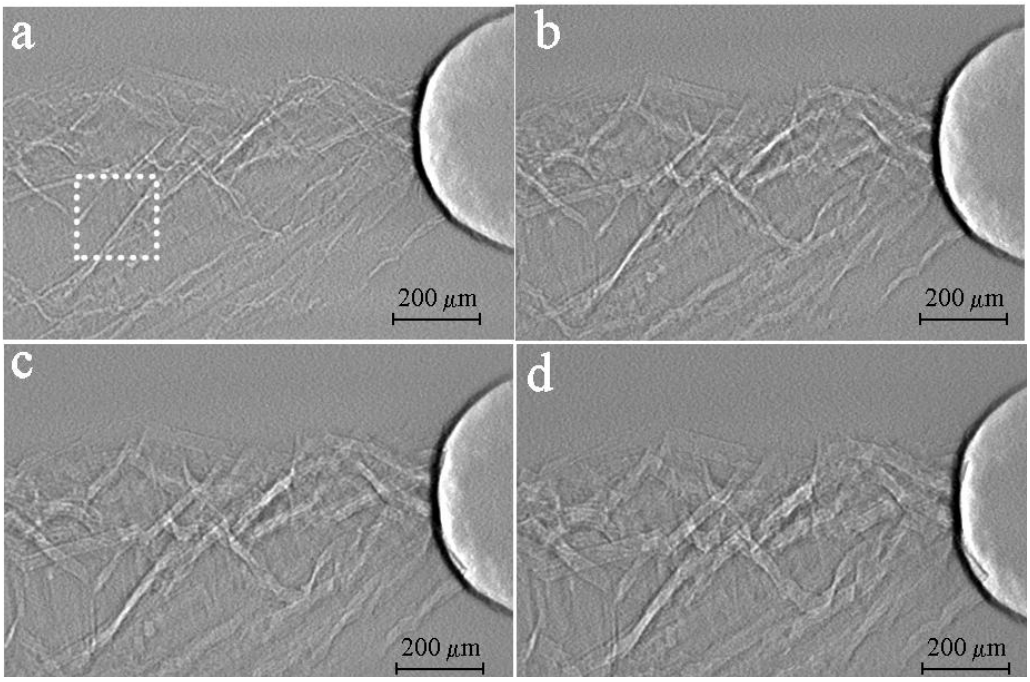

Figure 41: Phase contrast images of the sample CT-41M taken at different loads: a) 10 kgf b) 20 kgf c) 30 kgf d) 40 kgf. Notch is on the right side of the images. Crack growth direction is to the left. The direction of the applied load is vertical in the plane of the page. White rectangle marks the area shown in Figure 43

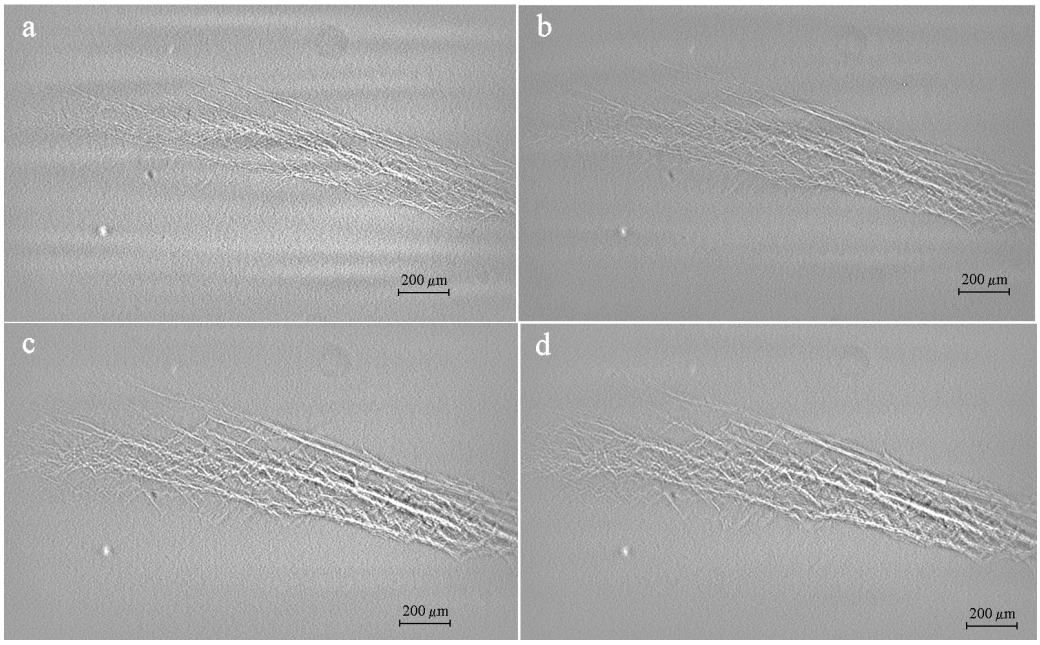

Figure 42: Phase contrast images of the sample CT-41M taken at different loads: a) 10 kgf b) 20 kgf c) 30 kgf d) 40 kgf in the area near the crack tip. Crack growth direction is to the left. The direction of the applied load is vertical in the plane of the page

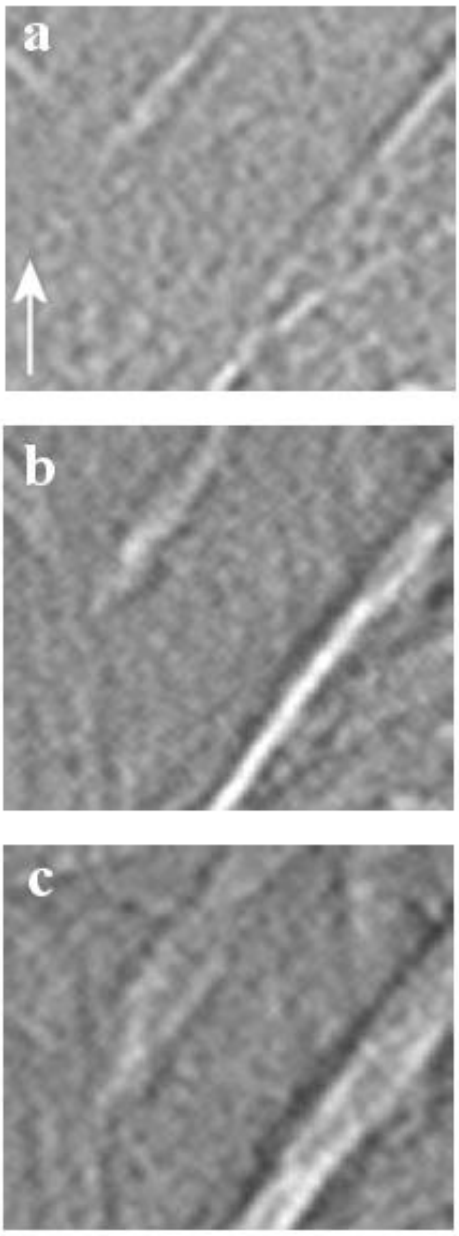

Figure 43: Magnified views of the phase contrast radiographs (from the area marked by white rectangle in Figure 41a) recorded at three loads ((a) 2 kgf , (b) 20 kgf and (c) 40 kgf) applied to sample CT-41M (direction of the applied load is shown by the arrow). Horizontal field of view is 170 μm

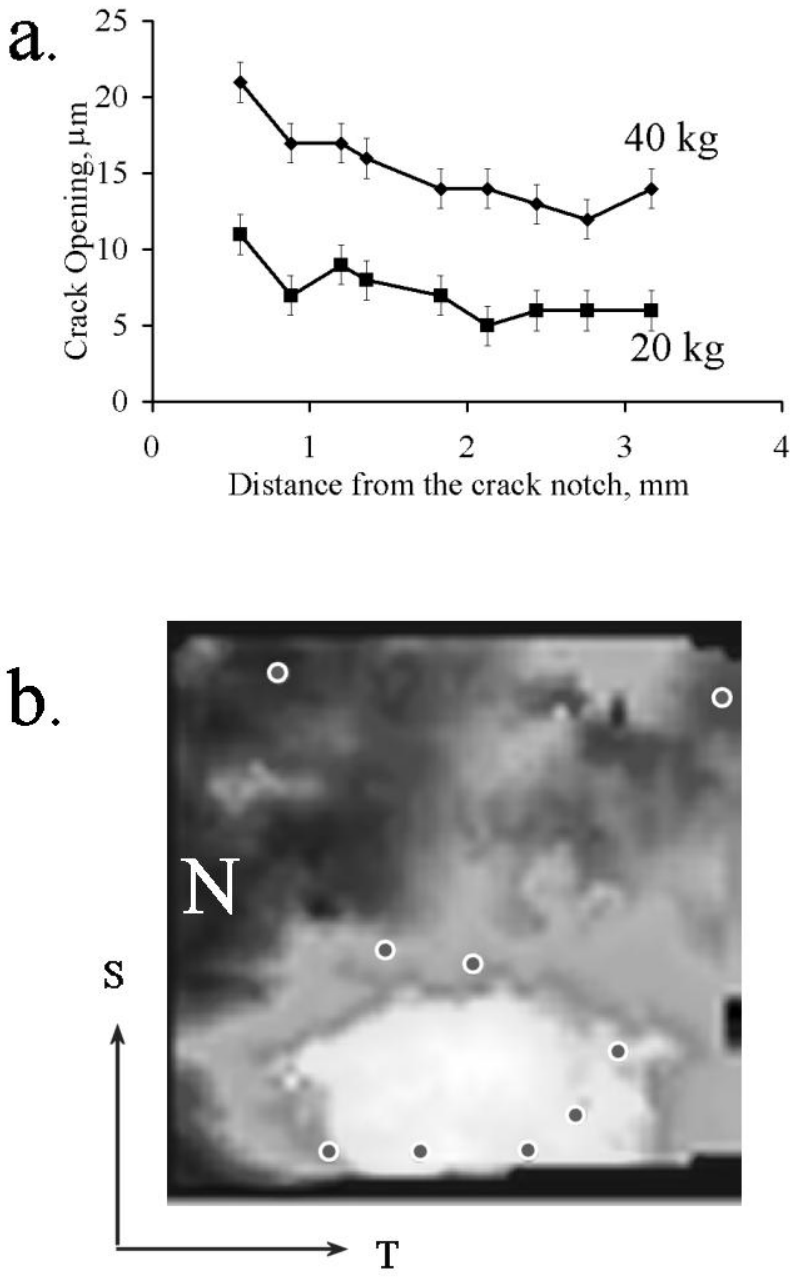

Figure 44: On the top — plot of crack opening for two loads at different positions (which are shown by circles on the crack surface grayscale map on the bottom) determined from phase microradiography.

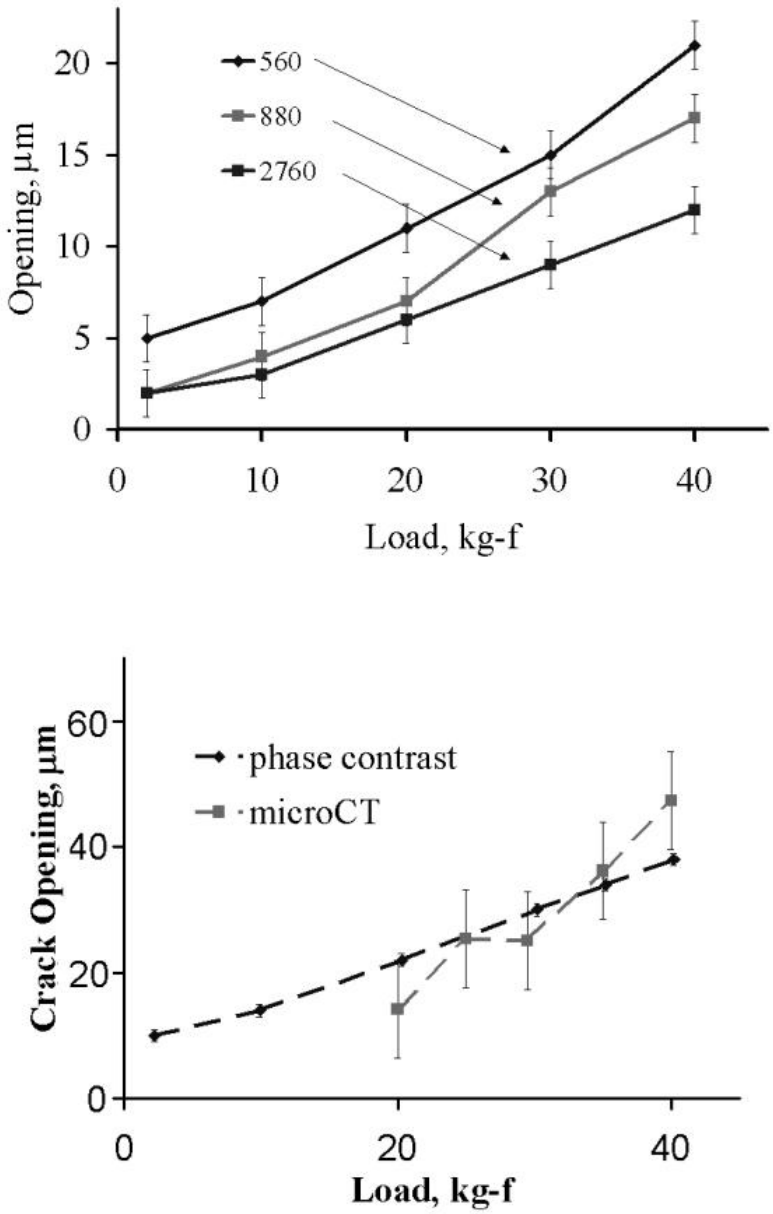

Figure 45: (a) Dependence of crack opening for three points on the crack surface (located at .56 mm, .88 mm and 2.76 mm from the notch tip) on load. b) Comparison of crack opening determined from phase contrast microradiograph and absorption microtomography for different loads

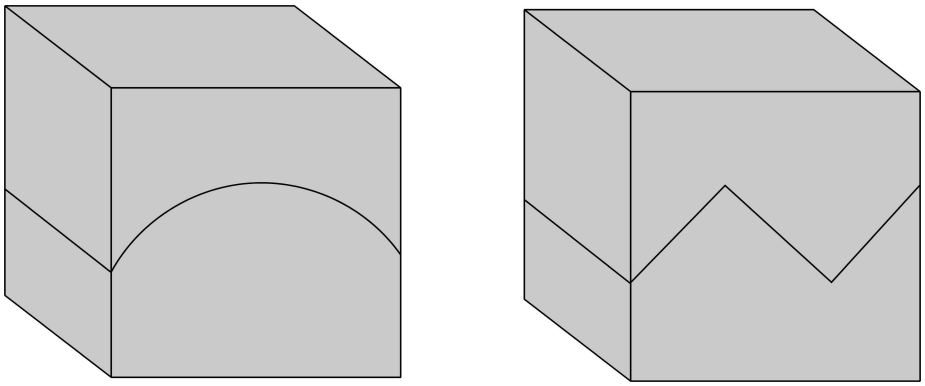

Figure 46: The geometry of two prototype aluminum specimens

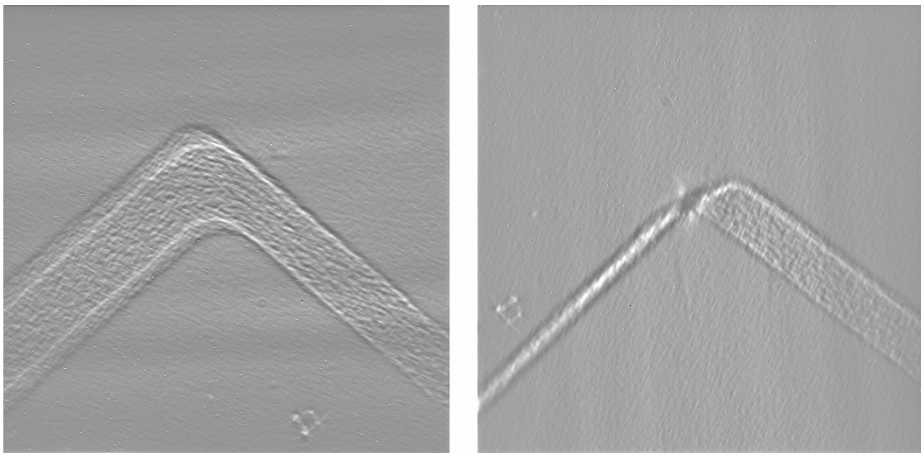

Figure 47: Phase contrast images of the cut in the phantom sample (right one on Figure 46) with the beam direction slightly off the sample face normal.

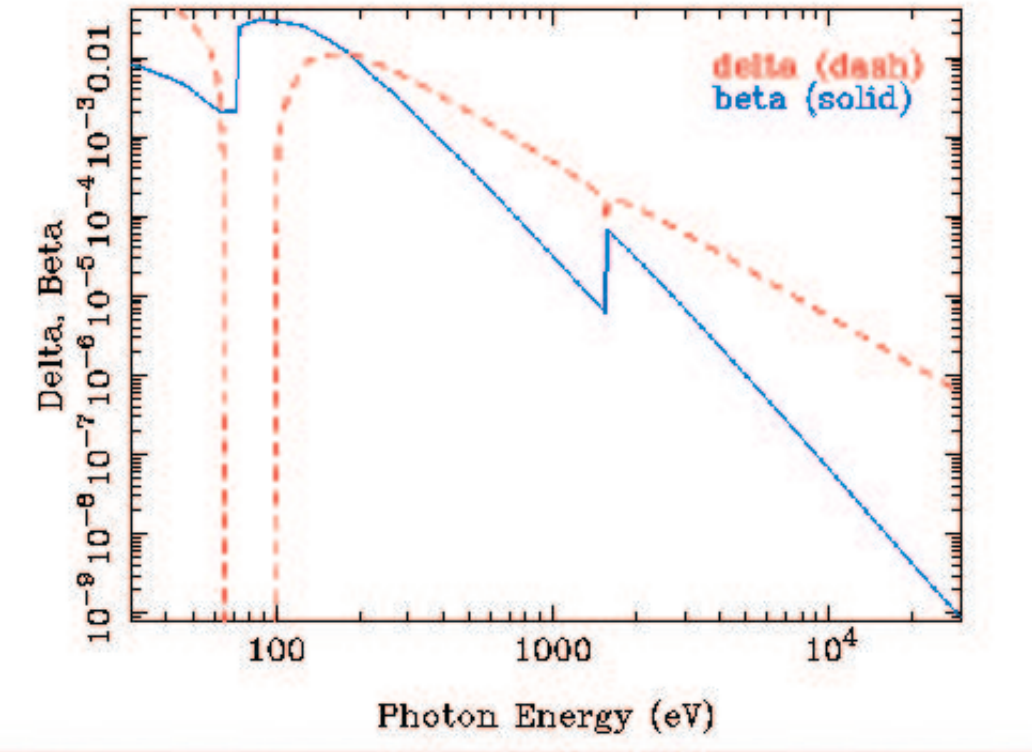

Figure 48: Plot of the deviation of the real part of the index of refraction from unity (δ, dash line) and imaginary part of the index of refraction (β, solid line) for aluminum as a function of photon energy [1].

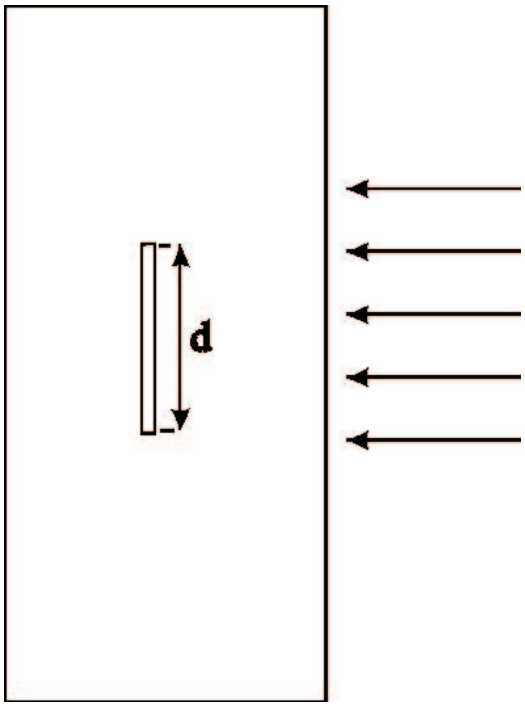

Figure 49: Schematic of a cross-section of a model sample containing a crack inside an aluminum that was used for simulation.

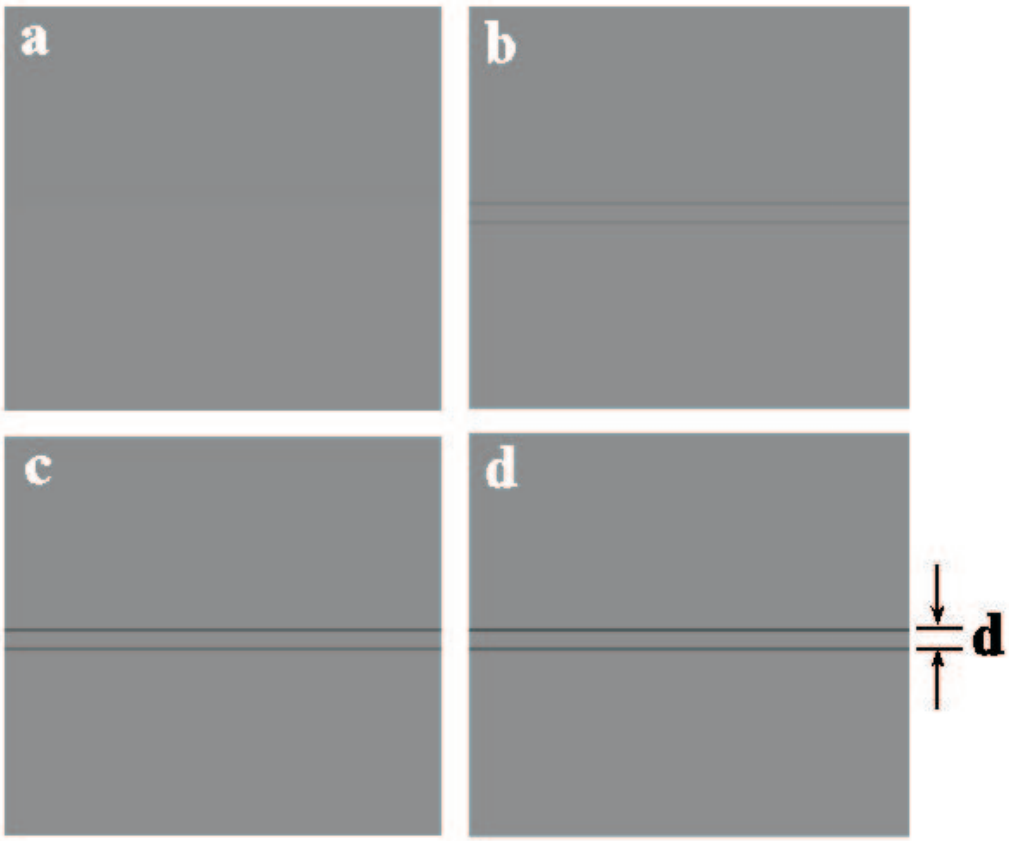

Figure 50: Results of a computer simulation in which 30 kEv X-ray beam passed through a model sample containing a crack (shown on Fig. 49) calculated for different sample - detector distances: a) 1 cm, b) 10 cm, c) 20 cm, and d) 30 cm. Results are shown in 2D in grayscale, where white corresponds to zero beam attenuation.

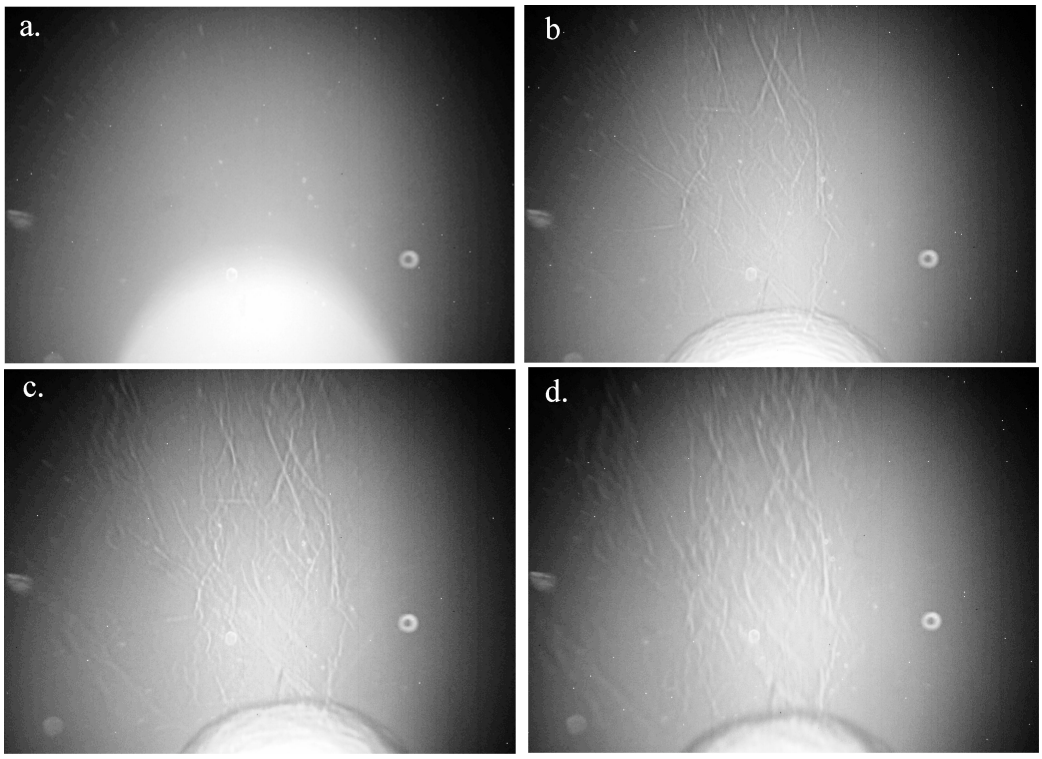

Figure 51: Phase contrast microradiographs of sample CT-43 recorded at different sample–detector distances. a) 10 mm, b) 250 mm, c) 500 mm, and d) 1000 mm. The notch from which the crack grew is at the bottom of the radiographs.

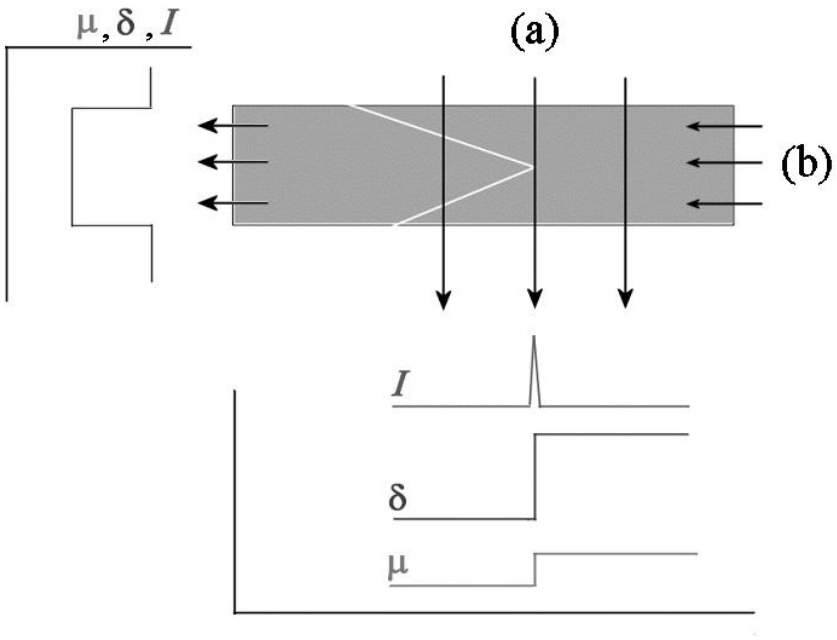

Figure 52: Schematic showing the phase contrast forming for two perpendicular orientations of a cracked sample. Arrows show direction of the X-ray beam. Plots schematically show line integrals of the sample linear attenuation coefficient (μ), deviation of the index of refraction from unity (δ) and X-ray intensity on the detector.

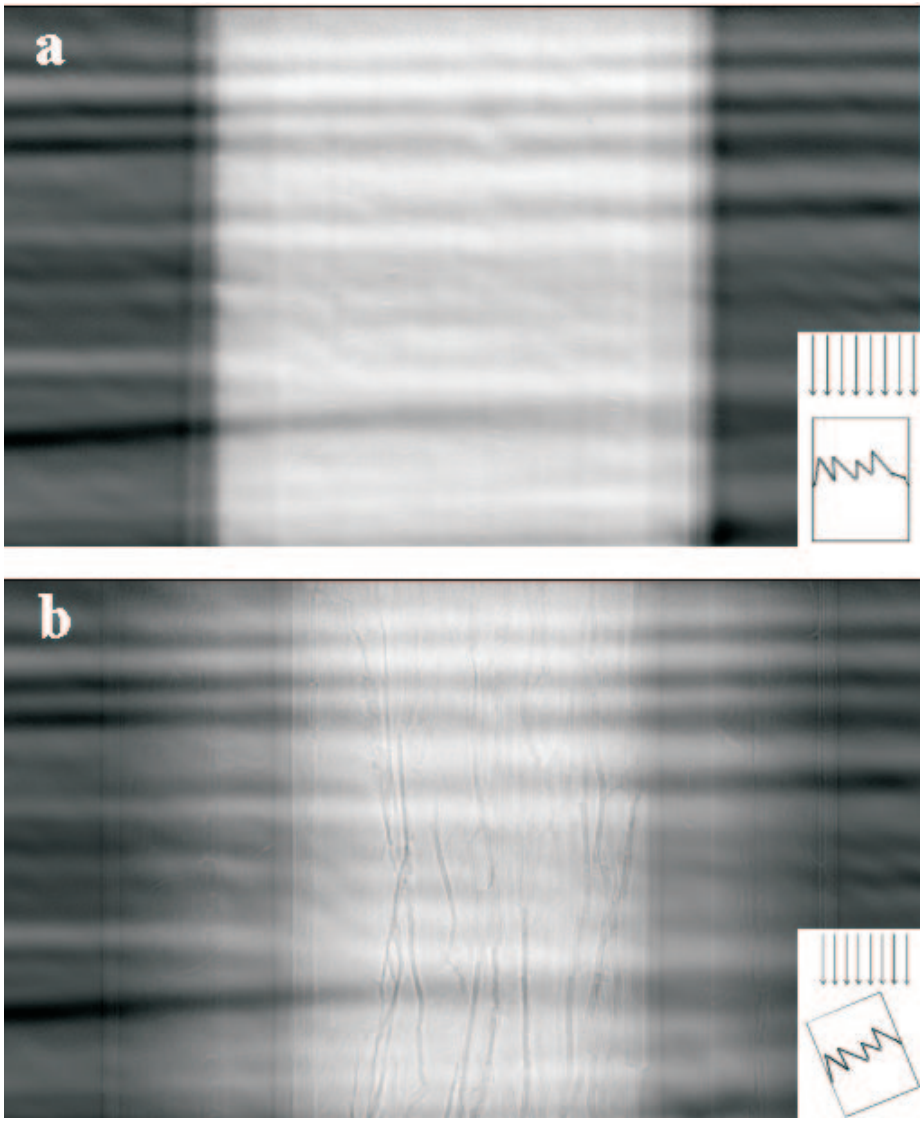

Figure 53: X-ray phase radiographs of sample CT-11 recorded at two different sample orientations (sample was rotated about the vertical axis, perpendicular to the X-ray beam). Insets in the lower right of the radiographs show horizontal cross-sections of the sample and arrows show X-ray direction. a) nominal crack plane is parallel to the detector; b) sample is rotated 22.5° about the vertical axis

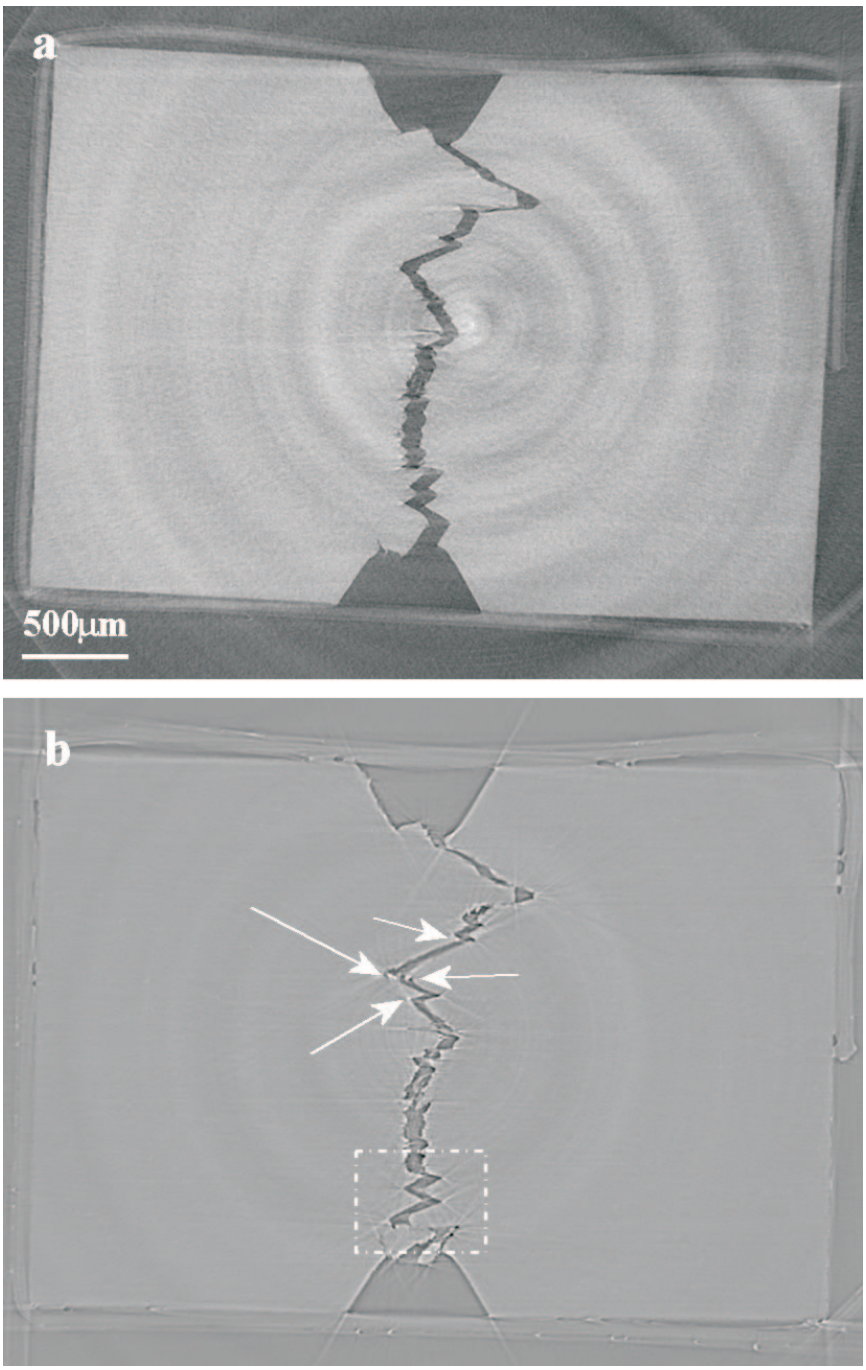

Figure 54: Reconstructed microCT slices of sample CT-11: a) at sample - detector distance of 50 mm; b) at sample - detector distance of 915 mm. Arrows in b) show areas with high contrast from phase shift. Selected area in b) is shown magnified in Fig. 55

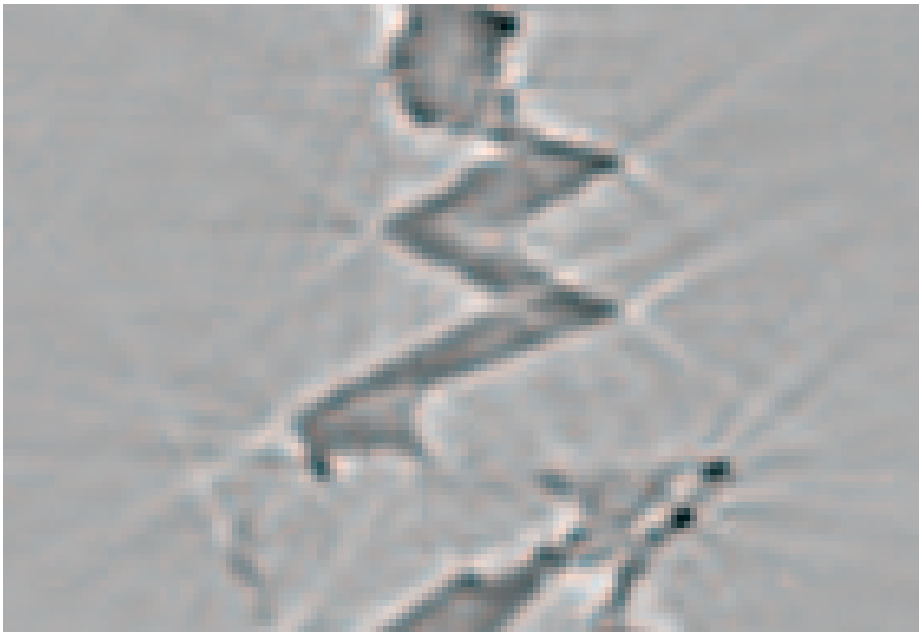

Figure 55: Magnified area of Fig. 54b showing areas of high contrast on the edges of the crack and reconstruction artifacts.

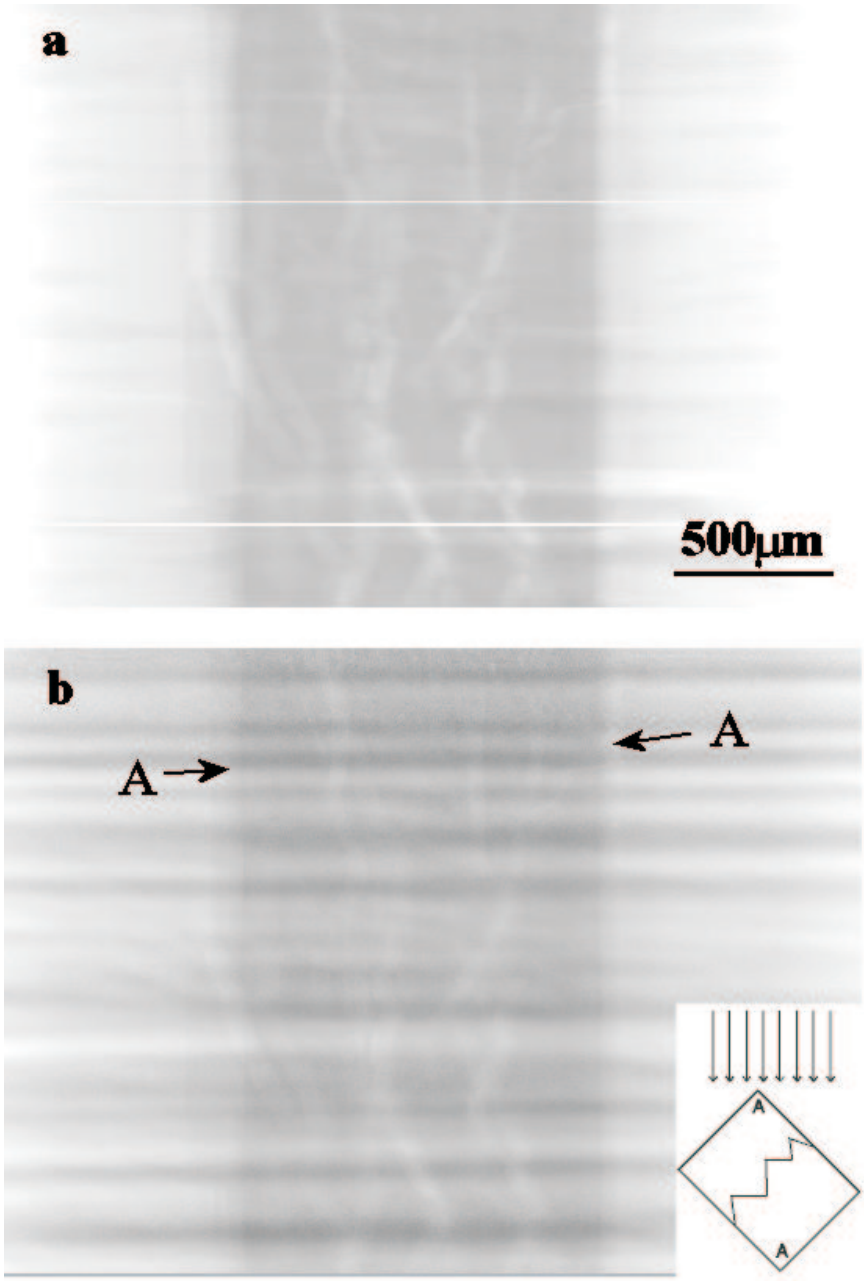

Figure 56: Comparison of the simulation results (a) with experimental radiograph (b). Inset shows schematic of the sample cross-section orientation, with nominal crack plane at 45° angle to the beam. "A" mark corners of the sample which correspond to vertical contrast lines in a) and b)

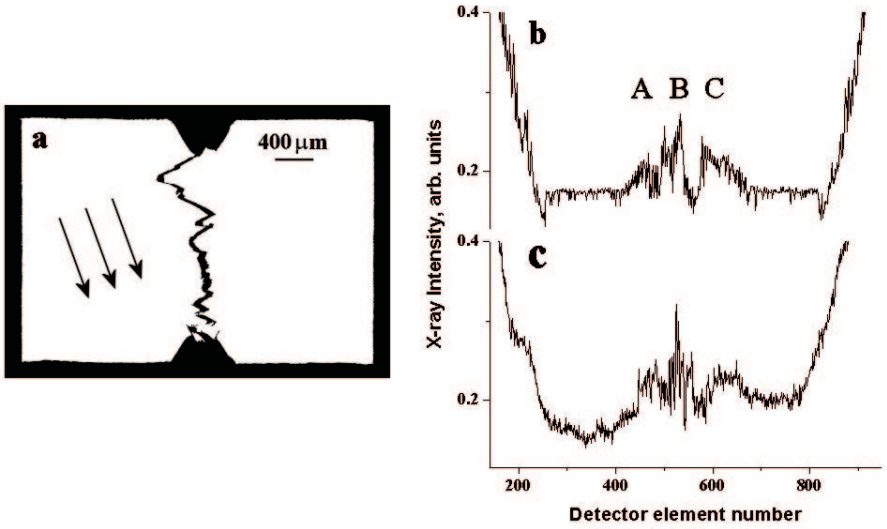

Figure 57: a) Segmented reconstructed microCT slice of sample CT-11. White represents aluminum and black represents empty space. Arrows show direction of the X-ray beam that was used in b) and c); b) calculated X-ray intensity profile at a sample - detector distance of 405 mm; c) experimental X-ray profile measured at the same distance.

REFERENCES

[1] *Center for X-ray Optics. Lawrence Berkeley National Lab. http://cindy.lbl.gov.*

[2] Rao, K. T. V. and Ritchie, R. O., "Fatigue of aluminum lithium alloys," *International Materials Reviews*, vol. 37, no. 4, pp. 153–185, 1992.

[3] Elber, W., "Fatigue crack closure under cyclic tension," *Engineering Fracture Mechanics*, vol. 2, pp. 37–45, 1970.

[4] Yoder, G. R., Pao, P. S., Imam, M. A., and Cooley, L. A., "Micromechanisms of fatigue fracture in Al-Li alloy 2090," Aluminum–Lithium Alloys. Vol. II, (Birmingham, UK), pp. 1033–1041, Mat. and Comp. Eng. Publ. Ltd., 1989.

[5] Starke, E. A. and Williams, J. C., "Microstructure and the fracture mechanics of fatigue crack propagation," Fracture Mechanics: Perspectives and Directions (Twentieth Symposium), (Philadelphia), pp. 184–205, ASTM, 1989.

[6] Haase, J. D., Guvenilir, A., Witt, J. R., and Stock, S. R., "X-ray microbeam mapping of microtexture related to fatigue crack asperities in Al-Li 2090," *Acta Materialia*, vol. 46, no. 13, pp. 4791–4799, 1998.

[7] Ignatiev, K., Rek, Z., and Stock, S. R., "X-ray microbeam diffraction comparison of mesotextures in plates of three aluminum alloys," vol. 44 of *Advances in X-ray analysis*, (Newtown Square, PA), pp. 56–61, International Centre for Diffraction Data (ICDD), 2001.

[8] Stock, S. R., Guvenilir, A., Breunig, T. M., Kinney, J. H., and Nichols, M. C., "Computed-tomography. part 3: Volumetric, high-resolution X-ray analysis of fatigue-crack closure," *Journal of the Minerals Metals and Materials Society*, vol. 47, no. 1, pp. 19–23, 1995.

[9] Guvenilir, A., Breunig, T. M., Kinney, J. H., and Stock, S. R., "Direct observation of crack opening as a function of applied load in the interior of a notched tensile sample of Al-Li 2090," *Acta Materialia*, vol. 45, no. 5, pp. 1977–1987, 1997.

[10] Guvenilir, A. and Stock, S. R., "High resolution computed tomography and implications for fatigue crack closure modelling," *Fatigue Fracture of Engineering Materials Structures*, vol. 21, no. 4, pp. 439–450, 1998.

[11] Stock, S. R., "X-ray microtomography of materials," *International Materials Reviews*, vol. 44, no. 4, pp. 141–164, 1999.

[12] Guvenilir, A., Breunig, T. M., Kinney, J. H., and Stock, S. R., "New direct observations of crack closure processes in Al-Li 2090 t8e41," *Philosophical Transactions of the Royal Society of London Series A — Mathematical Physical and Engineering Sciences*, vol. 357, no. 1761, pp. 2755–2775, 1999.

[13] Breunig, T. M., Stock, S. R., Antolovich, S. D., Kinney, J. H., Massey, W. N., and Nichols, M. C., "A framework for relating macroscopic measures and physical processes of crack closure illustrated by a study of aluminum-lithium alloy 2090," Fracture Mechanics: Twenty-Second Symposium (Vol.1), ASTM STP 1131, (Philadelphia), pp. 749–761, ASTM, 1992.

[14] Guvenilir, A., Stock, S. R., Barker, M. D., and Betz, R. A., "Physical processes of crack closure observed in the interior of an Al-Li 2090 compact tension sample," The 4th International Conference on Aluminum Alloys: Their Physical and Mechanical Properties. Vol. II, Georgia Institute of Technology, School of Materials Science and Engineering, pp. 413–419, 1994.

[15] Morano, R., Stock, S. R., Davis, G. R., and Elliott, J. C., "X-ray microtomography of fatigue crack closure as a function of applied load in Al-Li 2090 t8e41 samples," vol. 591 of *MRS Proceedings*, pp. 31–35, 2000.

[16] Morano, R. N., "Effect of r-ratio on crack closure in Al-Li 2090 t8e41, investigated non-destructively with X-ray microtomography," M.S. Thesis, Georgia Institute of Technology, Atlanta, Georgia, 1998.

[17] Momose, A., Takeda, T., Itai, Y., Yoneyama, A., and Hirano, K., "Perspective for medical applications of phase-contrast X-ray imaging," Medical Applications of Synchrotron Radiation: Proceedings of the International Workshop on Medical Applications of Synchrotron Radiation, (Tokyo), pp. 55–61, Springer-Verlag, 1998.

[18] Momose, A., Takeda, T., Itai, Y., and Hirano, K., "Phase-contrast X-ray computed tomography for observing biological soft tissues," *Nature Medicine*, vol. 2, no. 5, pp. 596–596, 1996.

[19] Arfelli, F., Assante, M., Bonvicini, V., Bravin, A., Cantatore, G., Castelli, E., Palma, L. D., Michiel, M. D., Longo, R., Olivo, A., Pani, S., Pontoni, D., Poropat, P., Prest, M., Rashevsky, A., Tromba, G., Vacchi, A., Vallazza, E., and Zanconati, F., "Low-dose phase contrast X-ray medical imaging," *Physics in Medicine and Biology*, vol. 43, no. 10, pp. 2845–2852, 1998.

[20] Takeda, T., Momose, A., Ueno, E., and Itai, Y., "Phase-contrast X-ray CT image of breast tumor," *Journal of Synchrotron Radiation*, vol. 5, pp. 1133–1135, 1998.

[21] Buffiere, J. Y., Maire, E., Cloetens, P., Lormand, G., and Fougeres, R., "Characterization of internal damage in a MMCP using X-ray synchrotron

phase contrast microtomography," *Acta Materialia*, vol. 47, no. 5, pp. 1613–1625, 1999.

[22] Rao, K. T. V., Yu, W., and Ritchie, R. O., "Fatigue crack-propagation in aluminum-lithium alloy 2090 .1. long crack behavior," *Metallurgical Transactions A — Physical Metallurgy and Materials Science*, vol. 19, no. 3, pp. 549–561, 1988.

[23] Rao, K. T. V., Yu, W., and Ritchie, R. O., "Fatigue crack-propagation in aluminum-lithium alloy 2090 .2. small crack behavior," *Metallurgical Transactions A — Physical Metallurgy and Materials Science*, vol. 19, no. 3, pp. 563–569, 1988.

[24] Pao, P. S., Cooley, L. A., Imam, M. A., and Yoder, G. R., "Fatigue-crack growth in 2090 Al-Li alloy," *Scripta Metallurgica*, vol. 23, no. 8, pp. 1455–1460, 1989.

[25] Rao, K. T. V., Yu, W., and Ritchie, R. O., "Cryogenic toughness of commercial aluminum-lithium alloys — role of delamination toughening," *Metallurgical Transactions A-Physical Metallurgy and Materials Science*, vol. 20, no. 3, pp. 485–497, 1989.

[26] Rao, K. T. V., Yu, W., and Ritchie, R. O., "On the behavior of small fatigue cracks in commercial aluminum-lithium alloys," *Engineering Fracture Mechanics*, vol. 31, no. 4, p. 623, 1988.

[27] Yoder, G. R., Pao, P. S., Imam, M. A., and Cooley, L. A., "Prediction of slip-band facet angle in the fatigue crack-growth of an Al-Li alloy," *Scripta Metallurgica*, vol. 22, no. 8, pp. 1241–1244, 1988.

[28] Sanders, T. H. and Starke, E. A., "The effect of slip distribution on the monotonic and cyclic ductility of Al-Li binary alloys," *Acta Metallurgica*, vol. 30, no. 5, pp. 927–939, 1982.

[29] Noble, B., Harris, S. J., and Dinsdale, K., "Yield characteristics of aluminium-lithium alloys," *Metal Science*, vol. 16, no. 9, pp. 425–430, 1982.

[30] Christensen, R. H., "Fatigue crack growth affected by metal fragments wedged between opening-closing crack surfaces.," *Applied Materials Research*, pp. 207–210, 1963.

[31] Budiansky, B. and Hutchinson, J. W., "Analysis of closure in fatigue crack growth," *Journal of Applied Mechanics — Transactions of the ASME*, vol. 45, no. 2, pp. 267–276, 1978.

[32] Suresh, S. and Ritchie, R. O., "A geometric model for fatigue crack closure induced by fracture surface-roughness," *Metallurgical Transactions A — Physical Metallurgy and Materials Science*, vol. 13, no. 9, pp. 1627–1631, 1982.

[33] Ritchie, R. O., "Fatigue — introduction," *Materials Science and Engineering A — Structural Materials Properties Microstructure and Processing*, vol. 103, no. 1, pp. 1–2, 1988.

[34] Herman, G. T., *Image reconstruction from projections. The fundamentals of computerized tomography.* Orlando: Academic Press, 1980.

[35] Kak, A. C. and Slaney, M., *Principles of computerized tomographic imaging.* New York: IEEE Press, 1988.

[36] Copley, D. C., Eberhard, J. W., and Mohr, G. A., "Computed-tomography .1. introduction and industrial applications," *Journal of the Minerals Metals and Materials Society*, vol. 46, no. 1, pp. 14–26, 1994.

[37] Radon, J. *Ber.Schsischen Akad.Wiss.*, vol. 69, pp. 262–277, 1917.

[38] Davis, G. R., Dowker, S. E. P., Elliott, J. C., Anderson, P., Wassif, H. S., Boyde, A., Goodship, A. E., Stock, S. R., and Ignatiev, K., "Non-destructive 3d structural studies by X-ray microtomography," vol. 45 of *Advances in X-ray analysis*, (Newtown Square, PA), pp. 485–490, International Centre for Diffraction Data (ICDD), 2002.

[39] *Scanco medical. http://www.scanco.ch.*

[40] *Skyscan. http://www.skyscan.be.*

[41] Davis, G. R. and Elliott, J. C., "X-ray microtomography scanner using time-delay integration for elimination of ring artefacts in the reconstructed image," *Nuclear Instruments Methods in Physics Research Section A — Accelerators Spectrometers Detectors and Associated Equipment*, vol. 394, no. 1-2, pp. 157–162, 1997.

[42] Breunig, T. M., Stock, S. R., and Brown, R. C., "Simple load frame for in-situ computed-tomography and X-ray tomographic microscopy," *Materials Evaluation*, vol. 51, no. 5, pp. 596–600, 1993.

[43] Haase, J. D., Guvenilir, A., Witt, J. R., Langoy, M. A., and Stock, S. R., "Microtexture, asperities, and crack deflection in Al-Li 2090 t8e41," Mixed-Mode Crack Behavior, ASTM STP 1359, pp. 160–173, 1999.

[44] Srivatsan, T. S., Anand, S., Sriram, S., and Vasudevan, V. K., "The high-cycle fatigue and fracture behavior of aluminum alloy 7055," *Materials Science and Engineering A — Structural Materials Properties Microstructure and Processing*, vol. 281, no. 1-2, pp. 292–304, 2000.

[45] Ignatiev, K., Lee, W. K., Fezzaa, K., Davis, G. R., Elliott, J. C., and Stock, S. R., "Three-dimensional mapping of fatigue crack position via a novel X-ray phase contrast approach," vol. 46 of *Advances in X-ray analysis*, (Newtown Square, PA), pp. 314–319, International Centre for Diffraction Data (ICDD), 2003.

[46] Toda, H., Sinclair, I., Buffiere, J. Y., Maire, E., Connolley, T., Joyce, M., Khor, K. H., and Gregson, P., "Assessment of the fatigue crack closure phenomenon in damage-tolerant aluminium alloy by in-situ high-resolution synchrotron X-ray microtomography," *Philosophical Magazine*, vol. 83, no. 21, pp. 2429–2448, 2003.

[47] Ludwig, W., Buffiere, J. Y., Savelli, S., and Cloetens, P., "Study of the interaction of a short fatigue crack with grain boundaries in a cast al alloy using X-ray microtomography," *Acta Materialia*, vol. 51, no. 3, pp. 585–598, 2003.

[48] Fitzgerald, R., "Phase-sensitive X-ray imaging," *Physics Today*, vol. 53, no. 11, pp. 82–82, 2000.

[49] Cowley, J. M., *Diffraction Physics*. Elsevier Science, 1995.

[50] Cloetens, P., Guigay, J. P., Demartino, C., Baruchel, J., and Schlenker, M., "Fractional talbot imaging of phase gratings with hard x rays," *Optics Letters*, vol. 22, no. 14, pp. 1059–1061, 1997.

[51] Hirano, K. and Momose, A., "Investigation of the phase shift in X-ray forward diffraction using an X-ray interferometer," *Physical Review Letters*, vol. 76, no. 20, pp. 3735–3737, 1996.

[52] Momose, A., Takeda, T., Itai, Y., Yoneyama, A., and Hirano, K., "Phase-contrast tomographic imaging using an X-ray interferometer," *Journal of Synchrotron Radiation*, vol. 5, pp. 309–314, 1998.

[53] Hirano, K. and Momose, A., "Investigation of the phase shift in X-ray forward diffraction using an X-ray interferometer," *Journal of Synchrotron Radiation*, vol. 5, pp. 967–968, 1998.

[54] Momose, A. and Hirano, K., "The possibility of phase-contrast X-ray microtomography," *Japanese Journal of Applied Physics Part 1*, vol. 38, pp. 625–629, 1999.

[55] Takeda, T., Momose, A., Yu, Q. W., Wu, J., Hirano, K., and Itai, Y., "Phase-contrast X-ray imaging with a large monolithic X-ray interferometer," *Journal of Synchrotron Radiation*, vol. 7, pp. 280–282, 2000.

[56] Ingal, V. N. and Beliaevskaya, E. A., "X-ray plane-wave topography observation of the phase-contrast from a noncrystalline object," *Journal of Physics D — Applied Physics*, vol. 28, no. 11, pp. 2314–2317, 1995.

[57] Chapman, D., Thomlinson, W., Zhong, Z., Johnston, R., and Pisano, E., "Diffraction enhanced imaging applied to materials science and medicine," *Synchrotron Radiation News*, vol. 11, no. 2, pp. 4–11, 1998.

[58] Spal, R. D., "Submicrometer resolution hard X-ray holography with the asymmetric bragg diffraction microscope," *Physical Review Letters*, vol. 86, no. 14, pp. 3044–3047, 2001.

[59] Snigirev, A., Snigireva, I., Kohn, V., Kuznetsov, S., and Schelokov, I., "On the possibilities of X-ray phase contrast microimaging by coherent high-energy synchrotron radiation," *Review of Scientific Instruments*, vol. 66, no. 12, pp. 5486–5492, 1995.

[60] Raven, C., Snigirev, A., Snigireva, I., Spanne, P., Souvorov, A., and Kohn, V., "Phase-contrast microtomography with coherent high-energy synchrotron X-rays," *Applied Physics Letters*, vol. 69, no. 13, pp. 1826–1828, 1996.

[61] Cloetens, P., Barrett, R., Baruchel, J., Guigay, J. P., and Schlenker, M., "Phase objects in synchrotron radiation hard X-ray imaging," *Journal of Physics D-Applied Physics*, vol. 29, no. 1, pp. 133–146, 1996.

[62] Spanne, P., Raven, C., Snigireva, I., and Snigirev, A., "In-line holography and phase-contrast microtomography with high energy X-rays," *Physics in Medicine and Biology*, vol. 44, no. 3, pp. 741–749, 1999.

[63] Gureyev, T. E., Raven, C., Snigirev, A., Snigireva, I., and Wilkins, S. W., "Hard X-ray quantitative non-interferometric phase-contrast microscopy," *Journal of Physics D — Applied Physics*, vol. 32, no. 5, pp. 563–567, 1999.

[64] Cloetens, P., Ludwig, W., Baruchel, J., Guigay, J. P., Pernot-Rejmankova, P., Salome-Pateyron, M., Schlenker, M., Buffiere, J. Y., Maire, E., and Peix, G., "Hard X-ray phase imaging using simple propagation of a coherent synchrotron radiation beam," *Journal of Physics D — Applied Physics*, vol. 32, no. 10A, pp. A145–A151, 1999.

[65] Cloetens, P., Ludwig, W., Baruchel, J., Dyck, D. V., Landuyt, J. V., Guigay, J. P., and Schlenker, M., "Holotomography: Quantitative phase tomography with micrometer resolution using hard synchrotron radiation X-rays," *Applied Physics Letters*, vol. 75, no. 19, pp. 2912–2914, 1999.

[66] Baruchel, J., Cloetens, P., Hartwig, J., Ludwig, W., Mancini, L., Pernot, P., and Schlenker, M., "Phase imaging using highly coherent X-rays: Radiography, tomography, diffraction topography," *Journal of Synchrotron Radiation*, vol. 7, pp. 196–201, 2000.

[67] Pogany, A., Gao, D., and Wilkins, S. W., "Contrast and resolution in imaging with a microfocus X-ray source," *Review of Scientific Instruments*, vol. 68, no. 7, pp. 2774–2782, 1997.

[68] Mayo, S. C., Davis, T. J., Gureyev, T. E., Miller, P. R., Paganin, D., Pogany, A., Stevenson, A. W., and Wilkins, S. W., "X-ray phase-contrast

microscopy and microtomography," *Optics Express*, vol. 11, no. 19, pp. 2289–2302, 2003.

[69] Kotre, C. J. and Birch, I. P., "Phase contrast enhancement of X-ray mammography: A design study," *Physics in Medicine and Biology*, vol. 44, no. 11, pp. 2853–2866, 1999.

[70] Westneat, M. W., Betz, O., Blob, R. W., Fezzaa, K., Cooper, W. J., and Lee, W. K., "Tracheal respiration in insects visualized with synchrotron X-ray imaging," *Science*, vol. 299, no. 5606, pp. 558–560, 2003.

[71] Cloetens, P., Pateyronsalome, M., Buffiere, J. Y., Peix, G., Baruchel, J., Peyrin, F., and Schlenker, M., "Observation of microstructure and damage in materials by phase sensitive radiography and tomography," *Journal of Applied Physics*, vol. 81, no. 9, pp. 5878–5886, 1997.

[72] Kowalski, G., Moore, M., and Nailer, S., "Application of X-ray phase-contrast imaging to polycrystalline cvd diamond," *Journal of Physics D — Applied Physics*, vol. 32, no. 10A, pp. A166–A171, 1999.

[73] Simov, S., Simova, E., and Davidkov, B., "Electron-microscope study of surface-topography by geometrical determination of metric characteristics of surface elements," *Journal of Microscopy*, vol. 137, no. 1, pp. 47–55, 1985.

[74] Kinney, J. H. and Nichols, M. C., "X-ray tomographic microscopy (xtm) using synchrotron radiation," *Annual Review of Materials Science*, vol. 22, pp. 121–152, 1992.

[75] Guvenilir, A., "Investigation into asperity induced closure in an Al-Li alloy using X-ray tomography," Ph.D. Thesis, Georgia Institute of Technology, Atlanta, Georgia, 1995.

[76] Laird, C., "The influence of metallurgical structure on the mechanisms of fatigue crack propagation," Fatigue Crack Propagation, STP 415, (Philadelphia), pp. 131–168, ASTM, 1967.

[77] Suresh, S., *Fatigue of materials*. Cambridge, UK: Cambridge University Press, 2nd ed., 1998.

[78] Haase, J. D., "Microbeam diffraction mapping of microtexture in Al-Li 2090 t8e41," M.S. Thesis, Georgia Institute of Technology, Atlanta, Georgia, 1998.

[79] Bronnikov, A. V., "Reconstruction formulas in phase-contrast tomography," *Optics Communications*, vol. 171, no. 4-6, pp. 239–244, 1999.

[80] Dowd, B. A., Campbell, B. H., Marr, R. B., Nagarkar, V., Tipnis, S., Axe, L., and Siddons, D. P., "Developments in synchrotron X-ray computed microtomography at the national synchrotron light source," SPIE Proc. 3772, pp. 224–236, 1999.

VITA

Dr. Konstantin Igorevich Ignatiev was born in St.Petersburg, Russia on January 8, 1973 to Dr. Igor Sergeevich Ignatiev and Dr. Irina Konstantinovna Butikova. He graduated from St.Petersburg high school number 239 with a coursework emphasis on math and physics in 1990. The same year he entered the optoelectronics program headed by Nobel Prize laureate Dr. Zhores Alferov at St.Petersburg Electrical Engineering University. During the last three years of study there, he also took additional classes in physics and electronics at the Ioffe Physico-Technical Institute. Dr. Ignatiev graduated with Diploma in 1996 and his thesis work, dedicated to the study of silicon carbide metal-oxide-semiconductor structures, was carried out under the guidance of Dr. Pavel A. Ivanov.

Dr. Ignatiev graduated with M.S. in Mechanical Engineering from Wichita State University in 1999 and his thesis, carried out under the guidance of Dr. Jharna Chaudhuri, was dedicated to X-ray studies of silicon carbide films. He attended the School of Materials Science and Engineering at Georgia Institute of Technology with Dr. Stuart R. Stock as his advisor, and graduated with Ph.D. in July 2004. During the last three years leading to graduation, Dr. Ignatiev had an appointment as a pre-doctoral research fellow at the Institute for Bioengineering and Nanoscience in Advanced Medicine at Northwestern University where he worked on his thesis and also took part in several research projects utilizing X-ray methods for research in biological and medical areas.

Dr. Ignatiev was married to Ms. Olga Tsareva on June, 5, 1998 in St.Petersburg, where she was studying for M.A. in fine arts, and they are currently expecting their first child.